Multi-antenna methods for scalable beyond-5G access networks

Placido Mursia

Multi-Antenna Methods for Scalable Beyond-5G Access Networks

Dissertation

submitted to

Sorbonne Université

in partial fulfillment of the requirements for the degree of
Doctor of Philosophy

Author:

Placido MURSIA

Scheduled for defense on the 28th of May, 2021, before a committee composed of:

Prof. Dr.	**Ana Isabel PEREZ NEIRA**	CTTC, Spain
Prof. Dr.	**Antti TÖLLI**	University of Oulu, Finland
Prof. Dr.	**Bruno CLERCKX**	Imperial College London, United Kingdom
Prof. Dr.	**Florian KALTENBERGER**	EURECOM, France
Prof. Dr.	**Marco DI RENZO**	CentraleSupélec, France
Prof. Dr.	**Mari KOBAYASHI**	Technical University of Munich, Germany

Thesis Director

Prof. Dr.	**David GESBERT**	EURECOM, France

Thesis Co-Directors

Prof. Dr.	**Italo ATZENI**	University of Oulu, Finland
Prof. Dr.	**Laura COTTATELLUCCI**	Friedrich-Alexander University, Germany

Techniques d'Antennes Multiples pour les Réseaux d'Accès Radio à Haute Densité en Aprés-5G

Thèse

soumise à

Sorbonne Université

pour l'obtention du Grade de Docteur

présentée par:

Placido MURSIA

Soutenance de thèse prévue le 28 Mai 2021 devant le jury composé de:

Prof. Dr.	**Ana Isabel PEREZ NEIRA**	CTTC, Espagne
Prof. Dr.	**Antti TÖLLI**	University of Oulu, Finlande
Prof. Dr.	**Bruno CLERCKX**	Imperial College London, Royaume-Uni
Prof. Dr.	**Florian KALTENBERGER**	EURECOM, France
Prof. Dr.	**Marco DI RENZO**	CentraleSupélec, France
Prof. Dr.	**Mari KOBAYASHI**	Technical University of Munich, Allemagne

Encadrant

Prof. Dr.	**David GESBERT**	EURECOM, France

Co-Encadrants

Prof. Dr.	**Italo ATZENI**	University of Oulu, Finlande
Prof. Dr.	**Laura COTTATELLUCCI**	Friedrich-Alexander University, Allemagne

Abstract

The exponential increase of wireless user equipments (UEs) and network services associated with current fifth-generation (5G) deployments poses several unprecedented design challenges that need to be addressed with the advent of future beyond-5G networks. Specifically, the growing demand for high data rates along with the need to serve a large number of heterogeneous devices, ranging from classical mobile phones, to connected objects forming the Internet-of-Things (IoT), motivates the study of novel signal processing and transmission schemes. In this regard, massive multiple-input multiple-output (MIMO) is a well-established access technology, which allows to serve many tens of UEs using the same time-frequency resources by means of highly directional beamforming techniques. However, massive MIMO exhibits scalability issues in *massive access* scenarios where the UE population is composed of a large number of heterogeneous devices.

Indeed, while the availability of a large number of antennas in massive MIMO transceivers brings substantial performance gains, it also greatly increases the system overhead and complexity. Specifically, the high dimensionality of the channels requires the allocation of considerable time-frequency resources to acquire the channel state information (CSI) and results in large matrix operations to construct precoders/decoders. Moreover, in the context of multicast communications as, e.g., wireless edge caching or broadcasting of mission-critical messages, conventional multi-antenna techniques exhibit vanishing rates as the number of UEs increases even in the massive antenna regime. Lastly, the large number of radio frequency (RF) chains associated with massive MIMO transceivers, which are used to counteract propagation losses in harsh environments such as, e.g., at millimiter-wave (mmWave) frequencies, clashes with the limited power budget of IoT devices.

In this thesis, we propose novel scalable multi-antenna methods for performance enhancement in the aforementioned scenarios of interest. Specifically, we describe the fundamental role played by statistical CSI that can be leveraged for reduction of both complexity and overhead for CSI acquisition, and for multi-UE interference suppression. Indeed, when the UEs are equipped with at least two antennas, their spatial selectivity properties can be leveraged to enforce statistical orthogonality among interfering transmissions. Moreover, we exploit device-to-device (D2D) communications to overcome the fundamental bottleneck of conventional multicasting. In particular, we exploit the precoding capabilities of a multi-antenna transmitter to carefully select UEs in favorable channel conditions, which in turn act as oppor-

tunistic relays and retransmit the message via the D2D links. Lastly, in the context of mmWave communications, we explore the benefits of the recently proposed reconfigurable intelligent surfaces (RISs), which are a key innovation enabler thanks to their inherently passive structure that allows to control the propagation environment and effectively counteract propagation losses. In particular, we employ passive beamforming at the RIS, i.e., without any significant power expenditure, together with conventional active beamforming at the transmitter to substantially increase the network throughput performance.

Abrégé

L'augmentation exponentielle des équipements d'utilisateurs sans fil (UEs) et des services des réseaux associés aux déploiements actuels de cinquième génération (5G) pose plusieurs défis de conception sans précédent qui doivent être résolus avec l'avènement des futurs réseaux au-delà de la 5G. Plus précisément, la demande croissante de débits de données élevés ainsi que la nécessité de desservir un grand nombre d'appareils hétérogènes, allant des téléphones mobiles classiques aux objets connectés formant l'internet des objets (IoT), motivent l'étude de nouveaux schémas de traitement et de transmission du signal. À cet égard, les sorties multiples massives à entrées multiples (massive MIMO) sont une technologie d'accès bien établie, qui permet de desservir plusieurs dizaines d'UEs en utilisant les mêmes ressources temps-fréquence au moyen de techniques de formation de faisceau hautement directionnelles. Cependant, le massive MIMO présente des problèmes d'évolutivité dans les scénarios accès massif où la population UE est composée d'un grand nombre de périphériques hétérogènes. En effet, si la disponibilité d'un grand nombre d'antennes dans les émetteurs-récepteurs massive MIMO apporte des gains de performances substantiels, elle augmente également considérablement la surcharge et la complexité du système. Plus précisément, la dimensionnalité élevée des canaux nécessite l'allocation de ressources temps-fréquence considérables pour acquérir les informations d'état de canal (CSI) et se traduit par de grandes opérations matricielles pour construire des précodeurs/décodeurs. De plus, dans le contexte de communications de multidiffusion comme, par exemple, la mise en cache périphérique sans fil ou la diffusion de messages critiques pour la mission, les techniques d'antennes multiples conventionnelles présentent des taux de disparition lorsque le nombre d'UEs augmente même dans le régime d'antenne massif. Enfin, le grand nombre de chaînes de radiofréquences (RF) associées aux émetteurs-récepteurs massive MIMO, qui sont utilisés pour contrer les pertes de propagation dans des environnements difficiles tels que, par exemple, à des fréquences d'ondes millimétriques (mmWave), se heurte au budget de puissance limité des appareils IoT. Dans cette thèse, nous proposons de nouvelles méthodes à antennes multiples évolutives pour l'amélioration des performances dans les scénarios d'intérêt susmentionnés. Plus précisément, nous décrivons le rôle fondamental joué par le CSI statistique qui peut être mis à profit pour réduire à la fois la complexité et la surcharge pour l'acquisition de CSI et pour la suppression des interférences multi-utilisateurs. En effet, lorsque les UEs sont équipés au moins de duex antennes, leurs propriétés de sélectivité spatiale peuvent être exploitées pour

imposer une orthogonalité statistique parmi les transmissions interférentes. De plus, nous exploitons les communications de périphérique à périphérique (D2D) pour surmonter le goulot d'étranglement fondamental de la multidiffusion conventionnelle. En particulier, nous exploitons les capacités de précodage d'un émetteur multi-antennes pour sélectionner soigneusement les UEs dans des conditions de canal favorables, qui à leur tour agissent comme des relais opportunistes et retransmettent le message via les liaisons D2D. Enfin, dans le cadre des communications mmWave, nous explorons les avantages des surfaces intelligentes reconfigurables (RISs) récemment proposées, qui sont un catalyseur clé de l'innovation grâce à leur structure intrinsèquement passive qui permet de contrôler l'environnement de propagation et de contrer efficacement les pertes de propagation. En particulier, nous utilisons la formation de faisceaux passive au niveau du RIS, c'est-à-dire sans aucune dépense d'énergie significative, ainsi que la formation de faisceaux active conventionnelle au niveau de l'émetteur pour augmenter considérablement les performances du réseau.

Acknowledgements

I would like to sincerely thank my thesis advisor David Gesbert and co-advisor Laura Cottatellucci for their invaluable leadership and constructive criticism throughout the duration of my Ph.D. degree. A special thank you goes to my second co-advisor Italo Atzeni, and to Mari Kobayashi, for the countless and always very useful technical discussions and advice. I am truly grateful for having had the possibility to work closely with all four of them.

I would like to thank my colleagues for their technical feedback and cooperation, notably the *M3* group, the Communication Systems department of EURECOM overall, and the members of the Marie-Curie ITN project SPOTLIGHT. Moreover, I would like to thank Dr. Vincenzo Sciancalepore, Dr. Xavier Costa-Pérez, and all the members of the 5GN group for hosting me at NEC Laboratories Europe GmbH. In this regard, I would like to mention my friends Antonio and Federico for having had a major role in making my experience in Heidelberg so fruitful both personally, and work-wise.

A big thank you goes to all other colleagues and friends at EURECOM who have contributed in creating such a friendly and relaxed work environment, which is key to overcoming all the bad moments but also to fully enjoy the good ones. In particular, I would like to mention my friends from the *FROST* team for all the great time we spent together and the indelible memories that I will always cherish.

I am particularly grateful to my long time friends from my home town, notably the *A.TO.MI.CA* group, for always being there for me, through good and bad times.

Last but not least, I would like to express my deep gratitude to my family for their unconditional love and for having been constant source of inspiration, and to Martina for her love and support, which were key to overcome the most important and difficult part of this journey: I would not be here without you. I dedicate this thesis to them.

Heidelberg, 17 May 2021 ***Placido Mursia***

Contents

List of Figures

List of Tables

List of Abbreviations

4G fourth-generation.

5G fifth-generation.

ADC analog-to-digital.

AF Amplify-and-Forward.

AoA angle of arrival.

AoD angle of departure.

AR Augmented Reality.

AWGN additive white Gaussian noise.

BD block diagonalization.

BS base station.

CSI channel state information.

CSIT channel state information at the transmitter.

CVX Disciplined Convex Programming.

D2D device-to-device.

DAC digital-to-analog.

DFT discrete Fourier transform.

FDD frequency-division duplex.

IoT Internet-of-Things.

ITN intelligent transport networks.

KKT Karush-Kuhn-Tucker.

LoS line-of-sight.

MIMO multiple-input multiple-output.

MISO multiple-input single-output.

MMSE minimum mean squared error.

mmWave millimiter-wave.

MRT maximum-ratio transmission.

MSE mean squared error.

NLoS non-line-of-sight.

NMSE normalized mean squared error.

pdf probability distribution function.

PLA planar linear array.

RF radio frequency.

RIS reconfigurable intelligent surface.

RZF regularized zero-forcing.

SDP semidefinite programming.

SDR semidefinite relaxation.

SE spectral efficiency.

SINR signal-to-interference-plus-noise-ratio.

SMSE sum mean squared error.

SNR signal-to-noise-ratio.

TDD time-division duplex.

UE user equipment.

ULA uniform linear array.

WF water-filling.

ZF zero-forcing.

Notations

The following list describes an overview of the notation used throughout this thesis. We use lowercase and uppercase boldface letters to denote vectors and matrices, respectively, whereas calligraphic uppercase letters denote sets. Vectors are denoted as column vectors by default.

$\mathbb{R}^{M\times N}$	Set of $M \times N$ real matrices
$\mathbb{C}^{M\times N}$	Set of $M \times N$ complex matrices
$\mathbb{Z}$	Set of integer numbers
$\mathbf{A}^{\mathrm{T}}$	Transpose of matrix $\mathbf{A}$
$\mathbf{A}^{\mathrm{H}}$	Hermitian transpose of matrix $\mathbf{A}$
$\mathbf{A}^{*}$	Conjugate of matrix $\mathbf{A}$
$[\mathbf{A}]_{ij}$	Element in position (i, j) of matrix $\mathbf{A}$
$\|\mathbf{x}\|$	Euclidean norm of vector $\mathbf{x}$
$\|\mathbf{A}\|_{\mathrm{F}}$	Frobenius norm of matrix $\mathbf{A}$
$\mathbb{E}[\mathbf{A}]$	Expectation of matrix $\mathbf{A}$
$\mathrm{Var}[\mathbf{x}]$	Variance of vector $\mathbf{x}$
$\mathrm{tr}(\mathbf{A})$	Trace of matrix $\mathbf{A}$
$\mathrm{rank}(\mathbf{A})$	Rank of matrix $\mathbf{A}$
$\mathrm{diag}(\mathbf{A})$	Vector containing the diagonal of matrix $\mathbf{A}$
$\mathrm{diag}(\mathbf{x})$	Diagonal matrix with diagonal elements equal to the entries of vector $\mathbf{x}$
$\mathbf{I}_N$	N-dimensional identity matrix
$\mathbf{e}_n$	n-th column of the identity matrix of size N
$\mathbf{0}$	Zero vector or zero matrix with proper dimension
$\mathrm{vec}(\mathbf{A})$	Vectorization of the matrix $\mathbf{A}$
$[\mathbf{x}_1, \ldots, \mathbf{x}_L]$	Horizontal concatenation of vectors $\mathbf{x}_1, \ldots, \mathbf{x}_L$
$\mathbf{A} \otimes \mathbf{B}$	Kronecker product of matrices $\mathbf{A}$ and $\mathbf{B}$
$\mathbf{A} \circ \mathbf{B}$	Element-wise product of matrices $\mathbf{A}$ and $\mathbf{B}$
$\mathbf{u}_{\min}(\mathbf{A})$	Eigenvector corresponding to the minimum eigenvalue of matrix $\mathbf{A}$
$\mathbf{u}_{\max}(\mathbf{A})$	Eigenvector corresponding to the maximum eigenvalue of matrix $\mathbf{A}$
$\mathbb{1}_{\mathscr{S}}(k, j)$	Indicator function equal to 1 if $(k, j) \in \mathscr{S}$ and to 0 otherwise
$\mathscr{CN}(\mathbf{0}, \mathbf{\Sigma})$	Zero-mean circularly symmetric complex Gaussian distribution with covariance matrix $\mathbf{\Sigma}$

Part I

Motivation and System Model

Chapter 1

Introduction

Fifth-generation (5G) and beyond networks will stand out from earlier fourth-generation (4G) deployments in several important ways [1]: (i) the need for very high throughput traffic delivery to a dense population of highly demanding internet users; (ii) the heterogeneity of devices that will download/upload data from/to the network, from classical human-controlled tablets and phones, to connected objects in use for smart cities and smart factories, and connected vehicles of the upcoming intelligent transport networks (ITN); (iii) the heterogeneity of performance metrics by which satisfaction will be measured by network operators and across these diverse devices, i.e., from peak data rate, to latency, reliability, and energy consumption. These combined departures from 4G networks motivate a re-design of signal processing and information coding mechanisms in order to offer the required performance and adaptability.

In this thesis, we consider a beyond-5G scenario in which a large number of heterogeneous user equipments (UEs) concurrently access the network, denoted as *massive access*, and we take on the challenge of designing novel multi-antenna methods to cope with the resulting technical challenges and to attain the associated unprecedented demands in terms of network performance [2, 3].

1.1 Massive MIMO

Among candidate technologies, massive multiple-input multiple-output (MIMO) plays a pivotal role in current 5G deployments [1, 4, 5] and is expected to maintain this role also in future beyond-5G wireless networks [6–9]. Indeed, thanks to its large number of antennas, massive MIMO is able to serve several UEs in the same time-frequency resources and can increase their received useful power by a factor that scales linearly with the number of available antennas. This is achieved thanks to highly directional beamforming, which results from the coherent combination of the transmit signals at the massive array. However, while the promises of massive MIMO are numerous and well investigated, some challenges remain yet

to be solved [5]. In particular, massive MIMO exhibits scalability issues in massive access scenarios due to the large number of UEs to be served. Indeed, the coherent transmission of signals requires the availability of the channel state information at the transmitter (CSIT), which poses several challenges in terms of system design in massive access scenarios. The channel state information (CSI) is necessary to attain the aforementioned benefits of massive MIMO but also implies increased complexity of implementing precoders/decoders and greater overhead linked with the pilot-aided training and CSI feedback as the number of antennas and UEs grows large.

Specifically, the high dimensionality of the channel requires the allocation of considerable communication resources for pilot-aided CSI acquisition and large matrix operations. In frequency-division duplex (FDD) systems, the CSI is obtained by means of downlink pilot transmission from the base station (BS) to the UEs. In this case, the amount of communication resources required for channel estimation in the downlink scales with the number of antennas M resulting in an excess overhead as M increases [10]. In contrast, in time-division duplex (TDD) systems, the CSI is acquired by means of uplink pilot transmission from the UEs to the BS, and the uplink channel estimates are then used also in the downlink thanks to channel reciprocity. Thus, the amount of required communication resources scales with the number of UEs K. However, since the channel coherence time is limited, the same pilot sequences must be reused across different UEs, thus generating pilot contamination that greatly reduces the quality of the CSI [11, 12]. As a result, the channel of interfering UEs who share the same pilot sequence becomes correlated, which poses a fundamental limitation on the achievable spectral efficiency (SE). Nevertheless, it is shown in [13] that, when using multi-cell minimum mean squared error (MMSE) precoding, the achievable SE of massive MIMO is not limited by pilot contamination as M grows large. However, such kind of precoding requires full CSI sharing across all cells, which significantly increases the overall signaling overhead.

1.1.1 The role of statistical channel information

To counteract such issues, several important works have proposed to use statistical CSI in the massive MIMO regime [14–26]. In particular, this information is represented by the channel covariance matrix, which characterizes the set of statistical channel directions and associated average channel power gains. Such statistical properties of the massive MIMO channel are essentially dictated by the angle spread spanned by the angle of arrival (AoA) of the multipath propagation of signals that impinge on the massive array. The angle spread of the AoAs is often bounded because of the high spatial resolution of the massive array compared to the limited scattering environment. As a result, the channel covariance matrices in massive MIMO tend to be low-rank and dominated by few major channel directions [13, 15, 18, 19]. This particular property can be exploited for several applications such as reducing feedback overhead in the channel estimation phase and mitigating interference in the downlink data transmission

phase. As shown in [19], this is possible if interfering UEs who are sufficiently far apart exhibit non-overlapping or orthogonal signal subspaces. Moreover, in [15], the authors show the dependence of the subspace richness of the signal associated with each UE on the scattering radius around the UE.

In this regard, several works have investigated the hybrid precoding problem where the beamforming applied at the BS is divided into an inner and outer precoder [16–18, 23]. The inner precoder is based on local instantaneous CSI while the outer precoder depends only on the second order channel statistics. Such approach results in a reduction of the number of pilot symbols required for CSI acquisition, as shown in [23]. Moreover, in the context of FDD systems where the CSI acquisition overhead problem is even more pronounced, the authors in [16] have proposed to utilize such hybrid precoding scheme in order to reduce the size of the resulting effective CSI vectors by exploiting the near-orthogonality of the angle spreads of the channels for different UE groups. The inner beamforming matrix is then calculated based on the reduced effective instantaneous channels of the UEs. In [18], this approach is shown to incur no loss compared to the full CSIT case when the number of antennas at the BS grows large. Furthermore, in [17] the authors show that such a scaling is obtained also in the case of finite number of antennas at the BS when employing suitable UE scheduling.

In TDD systems, existing works have pointed out how the BS can discriminate interfering UEs based solely on statistical channel information even in the presence of pilot contamination, thus providing the possibility to reuse pilots across multiple UEs [14, 19, 22, 26]. In [14], pilot reuse for massive MIMO transmission over spatially correlated Rayleigh fading channels is proposed as a means to reduce the overhead for channel estimation. Indeed, the sum mean squared error (MSE) of the channel estimates can be minimized provided that the intervals of the AoAs of the UEs reusing the pilots are non-overlapping, thus resulting in pilot decontamination. In [22], the channel second-order statistics is used to precode the pilot signals. This method reduces the variance of the channel estimation error by a factor that is proportional to the number of antennas at the UEs and hence provides the possibility to reuse pilots. A robust channel estimation method is investigated in [26] by exploiting path diversity in the angle domain, thus coping with scenarios in which the interfering channels may overlap with the desired channels in terms of AoAs of the channel multipath.

Statistical CSI can also be used in the design of precoders to mitigate interference in the downlink data transmission phase [24, 25]. Thanks to the availability of the channel covariance matrices, the BS can precode the signal such that the chosen propagation paths do not interfere on average. The authors in [24] propose to maximize a lower bound on the ergodic sum rate of a two-UE setting where the UEs are equipped with a single antenna. A robust transceiver based on a lower bound of the average MSE matrix under different CSI conditions is designed in [25].

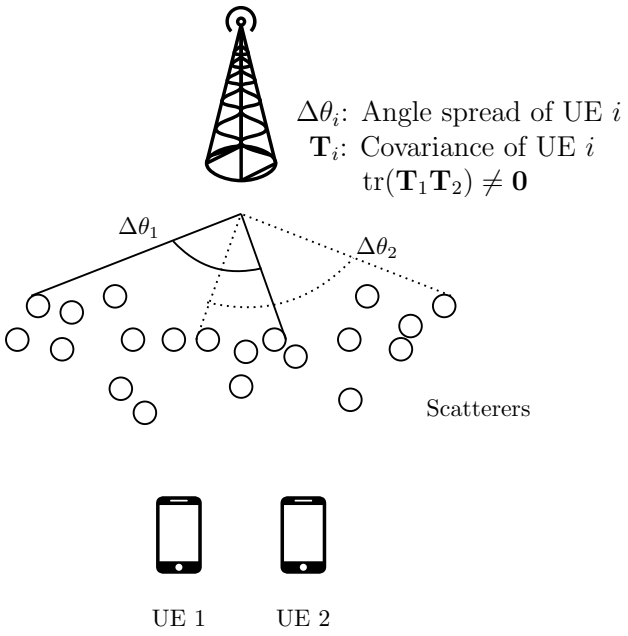

Figure 1.1 – The channel covariance matrix is essentially dictated by the angle spread spanned by the AoAs of the multipath propagation of signals. In many realistic scenarios, the angle spreads of interfering UEs are overlapping.

However, the performance of the above schemes relies on the structure of the channel covariance matrix of the UEs in terms of rank and degree of separation from the signal subspaces of the other UEs. Such properties are dictated by the physical scattering environment and *are generally beyond the control of the designer*. Hence, the condition of non-overlapping or orthogonal signal subspaces is rarely satisfied in practice, whereas in many practical scenarios, such as the one depicted in Fig. 1.1, the UEs exhibit high statistical correlation [13]. Moreover, existing works often assume the so-called Kronecker channel model due to its simple analytical structure. However, such a model has been shown to be an over-simplification of the true nature of the wireless channel [27]. How to use statistical channel information for CSI acquisition overhead reduction and interference mitigation under the assumption of more realistic channel models is the main topic of discussion in Part II of this thesis.

1.2 D2D Communications

In parallel, device-to-device (D2D) communications have recently gained momentum on account of emerging applications in 5G wireless systems such as multicasting, machine-to-machine communication, and cellular-offloading [28, 29], and are expected to be included in upcoming 5G deployments as a new paradigm for enhancing the performance of the network [1, 2, 30]. Indeed, D2D communications can be used as an alternative approach to cope with massive access scenarios by allowing UEs in close proximity to establish direct communication.

Hence, by replacing a relatively long radio link via the BS, which is severely limited by pathloss, with two shorter direct hops, D2D communications allow to reduce the power consumption and latency, and obtain higher data rates.

1.2.1 Multicast communications: when service reliability becomes a limiting factor

In this thesis, we consider the application of D2D communications in the context of multicast communications in which a transmitter wishes to convey a common message to multiple receivers. Such a scenario arises naturally in many wireless networks [31–36]. Specifically, multicast services are relevant for many challenging applications ranging from wireless edge caching, where popular contents are cached during off-peak hours and subsequently distributed via multicasting [37, 38], to the broadcasting of mission-critical messages in vehicular networks [39]. However, it is well known that multicasting over wireless channels is hindered by the *worst-user-kills-all* effect, whereby the multicast capacity vanishes as the number of UEs K increases for a fixed number of BS antennas [31, 32]. In fact, since the message transmitted by the BS must be decoded by all the UEs, the multicast capacity is limited by the UEs with the smallest fading gain and the latter tends to decrease with the system dimension. In particular, for the case of i.i.d. Rayleigh fading channels, the multicast capacity vanishes quickly as it scales inversely proportional to K [31]. Note that this behavior cannot be fundamentally solved by simply adding more antennas at the transceivers.

To overcome this issue, different approaches have been considered in the literature (e.g., [31, 33–36, 40–46]), which can be roughly classified into three groups. In the first group, a subset of UEs in good channel conditions is selected to be served, whereas the UEs in poor channel conditions are neglected [40, 41]. However, not only does such an approach result in limited network coverage, but it also implies solving a combinatorial problem to find the optimal subset of UEs. The second group exploits multiple antennas at the transmitter and the resulting channel hardening to mitigate the variance of the individual received signal power as the number of UEs increases [31, 42]. However, such an approach is based on the assumption of i.i.d. Rayleigh fading channels and requires that the number of BS antennas grows at least as $\log(K)$. Lastly, the third group builds on UE cooperation enabled by D2D links.

1.2.2 D2D-aided multicasting

In the aforementioned multicasting scenario, D2D communications between the UEs can be leveraged to overcome the vanishing behavior of the multicast capacity by dividing the total transmission time in two phases. Here, conventional multicasting occurs only in the first phase, where the BS transmits at such a rate that the common message is received by a

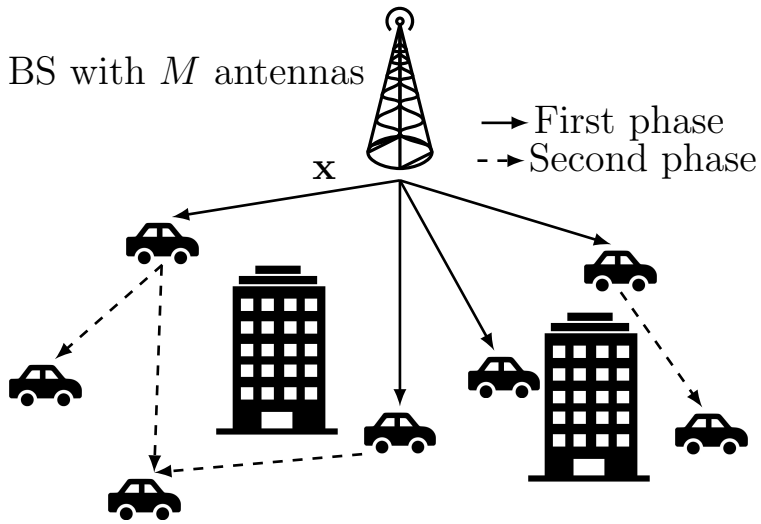

Figure 1.2 – D2D-aided two-phase cooperative multicasting. During the first phase, the BS sends the common message x via conventional multicasting to a set of relays, which in turn retransmit the message in the second phase via the D2D links to the rest of the network.

subset of UEs in favorable channel conditions. Then, these UEs act as opportunistic relays and cooperatively retransmit the message in the second phase. This approach, which is depicted in Fig. 1.2, has been extensively studied in the literature under specific CSIT assumptions and by focusing on the simple case of single-antenna transmitter [33–36, 43–46], as detailed next.

Theoretical analysis of two-phase cooperative multicasting can be found in [33–35, 43, 46]. More specifically, [33] established the multicast capacity by using a two-phase cooperative scheme for a simple network with i.i.d. Rayleigh fading channels. The multicast scaling was analyzed in [34] for two different network models, where the multicast capacity was shown to grow as $\log(\log(K))$ in the case of dense network (i.e., a scenario in which the number of receivers increases over a fixed network area) with spatially i.i.d. channels. Recently, [46] characterized the multicast scaling for a more general network topology (capturing the pathloss) and showed that, with statistical CSIT, the average multicast rate increases as $\log(\log(K))$. A similar analysis can be found in [35] for IEEE 802.16-based wireless metropolitan area networks. Furthermore, [43] characterized the achievable multicast rate of an interactive scheme based on full-duplex and non-orthogonal cooperation links. Another two-phase scheme was presented in [36], which focused on minimizing the total power consumption while guaranteeing a certain coverage under perfect CSIT. On the other hand, [44] considered a two-layer multicast message structure with a high-priority, low-rate part and a low-priority, high-rate part, such that the UEs who are able to decode the entire message assist the others by acting as opportunistic relays. The time allocation between the two phases was investigated in [45], which showed that more time should be dedicated to the second phase as the UEs move away

from the BS. Finally, a similar two-phase cooperative scheme with multiple antennas at the BS was proposed in [47] in the context of broadcasting under perfect CSIT. By exploiting rate splitting, this scheme forms a virtual common message to be multicast in the first phase and retransmitted via opportunistic relaying in the second phase.

In summary, existing works have demonstrated the benefits of two-phase cooperative schemes either for specific CSIT configurations or for the simple case of single-antenna BS. This motivates us to study the two-phase cooperative multicasting by exploiting multiple antennas at the BS, *which radically changes the nature of problem*, and to consider various CSIT configurations ranging from perfect CSIT, to topological CSIT (where only the map of the network area and the UE distribution are available at the BS). Such discussion is detailed in Part III of this thesis.

1.3 MmWave Communications

In the past few years, the need to cope with massive access scenarios has also led to the study of higher frequency bands as a means to guarantee connectivity to a large number of Internet-of-Things (IoT) devices. In this regard, millimiter-wave (mmWave) plays a key role in realizing the promises of 5G and will continue to do so in beyond-5G networks [9, 48]. Indeed, the advent of massive IoT applications spawning a huge volume of devices poses mmWave as a candidate solution for many applications such as smart grids, smart cities and smart industries [49]. However, mmWave contrasts with the low-power nature of IoT devices that are not able by themselves to counteract the harsh propagation environments in such high frequency bands. The main challenge in this case is that mmWave transceivers usually employ multiple radio frequency (RF) chains and a large number of antennas to combat the aforementioned high pathloss attenuation. This strategy contrasts with energy-constrained IoT devices, as integrating multiple active components draining energy becomes infeasible [50].

1.3.1 RIS-aided networks

In the context of mmWave communications, reconfigurable intelligent surfaces (RISs) are gaining much attention on account of recent advances in metamaterials, making them feasible to be constructed and installed in urban environments [51].[1] A RIS is a reflecting surface that can be conveniently modeled as a discrete array of passive antennas, each of which can introduce a phase shift plus an amplitude attenuation in the signal. A suitable optimization of all such equivalent antenna elements results in a coherent combination of all the phase-shifted and attenuated paths of the incoming signal. This results in a very narrow and directive beam,

[1] Note that the term *intelligent reflecting surface* (IRS) is alternatively used in other related works. The acronyms IRS and RIS can be used interchangeably as they refer to the same physical device, i.e., a reflecting surface that can be controlled by some network entity. To avoid ambiguity, we have chosen to use in this dissertation the term RIS.

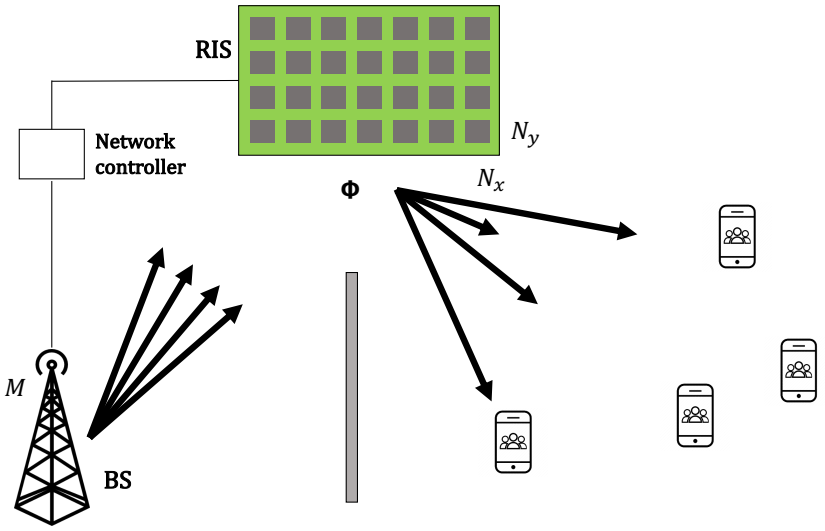

Figure 1.3 – Example of RIS-aided network with the line-of-sight (LoS) path obstructed, where $\mathbf{\Phi}$, N_X, and N_y are the matrix containing the induced phase shifts, and the number of RIS elements along the x and y axis, respectively.

which can improve the received signal quality at the receiving UE [52]. Such optimization is usually carried out by some central entity in the network who then informs the RIS of the resulting optimized parameters [53]. The latter is thus a fully passive structure whose sole active component is the RIS controller, which produces small variations in the input voltage on each RIS element that results in a phase shift added to the incoming signal. Hence, RISs can ultimately transform the uncontrollable nature of the propagation environment into a programmable medium by effectively counteracting pathloss attenuation and fading effects.

Thanks to the use of RISs, it is then possible to exploit the large amount of spectrum available at mmWave frequencies and dramatically increase peak data rates. Conceptually, a RIS may remind some of the challenges behind conventional *Amplify-and-Forward (AF)* relaying methods [54] and the beamforming methods used in (massive) MIMO [55]. However, there exists a marked difference between conventional AF relays and RISs [56,57]. Indeed, the former rely on active (energy-consuming) low-noise power amplifiers and other active electronic components, such as digital-to-analog (DAC) or analog-to-digital (ADC) converters, mixers, and filters. In contrast, RISs have very low hardware footprint, consisting of a single or just a few layers of planar structures that can be built using lithography or nano-printing methods. Consequently, RISs are particularly attractive for seamless integration into walls, ceilings, object cases, building glasses, or even clothing [58]. On the other hand, both massive MIMO and RIS technology can produce similar signal-to-noise-ratio (SNR) gains.[2] However, a RIS

[2]Although it has been shown that the SNR scales linearly with the number of antennas when using massive MIMO and proportional to the square of the number of equivalent antenna elements with RIS technology, the lack

achieves such beamforming gains in a near-passive way since only a (negligible) power input is required for the RIS controller, thus exhibiting high energy efficiency.

On account of the previously described advantages, RISs are in fact gaining a lot of momentum in massive access scenarios [52, 59–73] because of their aforementioned ability to turn the stochastic nature of the wireless environment into a programmable channel. RISs have been recently proposed for a variety of applications including secure communications [67, 68], non-orthogonal multiple access [69], over-the-air-computation [70], or energy-efficient cellular networks [71, 72].

While the theoretical modelling of RIS-aided wireless networks is well studied, many challenges are still open such as building testbeds for experimental validation [74–77], the task of estimating the combined channel from the BS to the RIS and on to the UE [78, 79], and the joint optimization of the multi-antenna BS and the RIS parameters [79–85]. Particularly relevant for this thesis is the latter category, concerning the joint optimization of active beamforming at the BS and passive beamforming at the RIS. In [80] the authors analyzed a single-UE case and propose to maximize the rate. The resulting non-convex optimization problem is solved via both fixed-point iteration and manifold optimization. A similar setting is analyzed in [79], where the authors propose a heuristic solution to the non-convex maximization of the received signal power with similar performance to conventional semidefinite relaxation (SDR). The single-UE setting is also studied in [84], where the authors propose to encode information both in the transmitted signal and in the RIS configuration. A multi-user setting is analyzed in [81] where the authors propose to maximize the minimum receive SNR among all UEs in the large system regime. While this approach guarantees fairness among UEs, it might not maximize the system sum rate. In [82], the authors design jointly the beamforming at the BS side and the RIS parameters by minimizing the total transmit power at the BS, given a minimum receive signal-to-interference-plus-noise-ratio (SINR) requirement. This framework was later extended to consider low-resolution RISs in a single-UE setting [83].

In this thesis, we consider an RIS-aided network as the one depicted in Fig. 1.3 and claim that active beamforming via an antenna array at the transmitter side and passive beamforming in the channel via a RIS *can complement each other* and provide even larger gains when they are jointly optimized. In particular, we introduce a novel mathematical framework to minimize the sum mean squared error (SMSE) of RIS-aided beamforming communication systems, which is suitable for massive IoT wireless access. This approach, which to the best of our knowledge has not been explored before, allows us to build efficient algorithms that maximize the sum rate performance while guaranteeing efficiency and scalability. This concept is further detailed in Part IV of this thesis.

of power amplification in the latter determines a performance loss such that, overall, both technologies produce very similar SNR gains given the same conditions [55].

1.4 Thesis Outline and Main Contributions

In this section, we give a brief outline of this dissertation by highlighting the key concepts and contributions detailed in each of its sections. Specifically, this thesis is divided into five parts, which are briefly described as follows.

Part I: Motivation and System Model. This part is divided in two chapters. Chapter 1 describes the motivation behind our work by shedding some light on the open challenges and limitations of state-of-the-art on multiple-antenna technologies in beyond-5G wireless networks. Chapter 2 describes the system model of the considered massive access scenario. In particular, we describe such a scenario in its most general case providing key definitions, assumptions and performance metrics that will be utilized throughout this dissertation. In the subsequent parts, we will particularize the aforementioned setting in order to better focus on different specific design aspects.

Part II: Covariance Shaping. In Chapter 3, we introduce the concept of *covariance shaping*, which consists in suitably altering the channel statistics perceived by the BS by means of statistical beamforming at the UE-side as to enforce partial or full orthogonality among interfering transmissions in space. This method is based solely on statistical channel properties and can be used both for overhead and complexity reduction in the acquisition of CSI and matrix operations, respectively, and for interference mitigation. Compared to existing works that unrealistically assumes statistical orthogonality as a property given by the physical scattering environment, covariance shaping exploits the spatial selectivity properties of the UEs when the latter are equipped with at least two antennas to enforce such a property in any given physical scenario. Moreover, covariance shaping assumes a general channel model that goes beyond the commonly-assumed Kronecker structure. Indeed, while the Kronecker channel model is widely spread due to its simple analytical formulation and tractability, it does not allow the UEs to alter the channel statics perceived by the BS. In this regard, we turn a generally inconvenient but more realistic channel model into a benefit. In Chapter 4, this method is firstly investigated in the simple case of two UEs in order to highlight its key characteristics and it is then extended to a general number of UEs. Furthermore, we derive the achievable sum rate under covariance shaping, which further exposes the effects of the proposed method on the performance of the network. These results were published in the following papers.

[21] P. Mursia, I. Atzeni, D. Gesbert, and L. Cottatellucci, "On the Performance of Covariance Shaping in Massive MIMO Systems," in *Proc. IEEE Int. Workshop Computer-Aided Modeling and Design of Commun. Links and Netw. (CAMAD)*, Barcelona, Spain, 2018

[20] P. Mursia, I. Atzeni, D. Gesbert, and L. Cottatellucci, "Covariance Shaping for Massive MIMO Systems," in *Proc. IEEE Global Commun. Conf. (GLOBECOM)*, Abu Dhabi, UAE, 2018

[86] P. Mursia, I. Atzeni, D. Gesbert, and L. Cottatellucci, "Enforcing Statistical Orthogonality in Massive MIMO Systems via Covariance Shaping," 2021, submitted to *IEEE Trans. Wireless Commun. (TWC)* [Online]. Available: https://arxiv.org/abs/2106.07952

Part III: D2D-Aided Multi-Antenna Multicasting. In this part we consider a cooperative two-phase multicasting scheme in the presence of multiple antennas at the BS. By endowing the BS with precoding capabilities, the problem of designing a cooperative multicasting scheme capitalizing on D2D communications changes radically in nature. Indeed, it requires to jointly optimize the precoding strategy and the multicast rate in order to maximize the system performance. To the best of our knowledge, this scenario has not been considered so far in existing works. In Chapter 5, we described the considered system model and optimization metrics. Specifically, we use the notion of *average multicast rate* and *outage multicast rate* as performance metrics, which correspond to the maximum multicast rate under average and joint outage constraints on the achievable rates of the UEs, respectively. Such constraints are specified by a *target outage*, which allows to avoid wasting useful communication resources to serve a small percentage of UEs that might be in particularly unfavorable channel conditions. Moreover, differently from previous works we consider various CSIT configurations and propose three algorithms denoted as: (i) D2D-MAM, which is applicable in the case of perfect CSIT; (ii) D2D-SMAM, which is designed to account for the availability of statistical long-term CSIT, and (iii) D2D-TMAM, which assumes only coarse CSIT such as the map of the network and the probability distribution function (pdf) of the UEs in space. The proposed methods, which are detailed in Chapter 6, exploit the precoding capabilities at the BS to target specific UEs that can effectively serve as D2D relays towards the remaining UEs, and maximize the multicast rate under the specified outage constraint and CSIT configuration. In all the considered cases, the proposed algorithms overcome the worst-UE bottleneck behavior of conventional single-phase multi-antenna multicasting and turn a large UE-population into a benefit for the achievable multicast rate. These results have led to the following publications.

[87] P. Mursia, I. Atzeni, D. Gesbert, and M. Kobayashi, "D2D-Aided Multi-Antenna Multicasting," in *Proc. IEEE Int. Conf. Commun. (ICC)*, Shanghai, China, 2019, **best paper award.**

[88] P. Mursia, I. Atzeni, M. Kobayashi, and D. Gesbert, "D2D-Aided Multi-Antenna Multicasting in a Dense Network," in *Proc. Asilomar Conf. Signals, Syst., and Comput. (ASILOMAR)*, Pacific Grove, USA, 2019

[89] P. Mursia, I. Atzeni, M. Kobayashi, and D. Gesbert, "D2D-Aided Multi-Antenna Multicasting under Generalized CSIT," 2021, submitted to *IEEE Trans. Wireless Commun. (TWC)* [Online]. Available: https://arxiv.org/abs/2102.01624

Part IV: Reconfigurable Intelligent Surfaces. In Chapter 7, we discuss the integration of the recently introduced RIS technology into existing MIMO systems as a means to enhance the

performance of the network in massive access scenarios. Specifically, we propose a RIS-aided multi-UE alternating optimization algorithm, denoted as RISMA, that jointly optimizes the (active) beamforming strategy at the BS and the (passive) phase shifts at the RIS. Compared to existing works, RISMA has the unique advantage of a simple and efficient optimization framework, which results from the choice of the SMSE as optimization metric. This choice plays a key role in determining the associated complexity of the optimization procedure and resulting network performance. Indeed as described in Chapter 8, the SMSE allows us to obtain a convex problem in the two optimization variables separately. Specifically, when employing alternating optimization between the beamforming vector at the BS and the phase shifts at the RIS, the resulting sub-problems are solved in closed-form thus resulting in scalability and efficiency of the design without the need of setting any system parameter. In addition, we adapt RISMA, which provides a solution from a theoretical perspective, to accommodate practical constraints when using low-resolution RISs comprising antenna elements that can be activated in a binary fashion. In particular, such RISs only support phase shift values from a discrete set, rather than any real value from a range, and further compound our problem. To address this scenario, we propose Lo-RISMA, which decouples the optimization of the binary activation coefficients and the quantized phase shits. The former are optimized via SDR while the latter are projected onto the quantized space. Differently from other prior work considering low-resolution RISs, Lo-RISMA benefits from the key properties of the chosen SMSE metric. Specifically, for each iteration of the proposed algorithm for a fixed RIS configuration the precoding strategy is found via a simple closed-form solution, and once the precoding strategy is fixed the problem of finding the RIS parameters is efficiently solved via SDR. The aforementioned work has resulted in the following publication.

[90] P. Mursia, V. Sciancalepore, A. Garcia-Saavedra, L. Cottatellucci, X. Costa-Perez, and D. Gesbert, "RISMA: Reconfigurable Intelligent Surfaces Enabling Beamforming for IoT Massive Access," *IEEE J. Sel. Areas Commun. (JSAC)*, vol. 8716, no. c, pp. 1–1, 2020

Part V: Concluding Remarks. This last part concludes this dissertation by summarizing the main contributions and drawing final remarks on the previously described parts. Lastly, we give some insights on possible future works and research directions. The manuscript ends with the appendices, the list of publications, the résumé of the thesis in French, and the list of references.

Chapter 2

System Model

In this chapter, we describe the considered scenario in its most general setting by defining the key parameters, physical quantities, and performance metrics of interest. Such a scenario serves as a common basis throughout the rest of the thesis and is studied under different assumptions and simplifications in the subsequent parts. We consider a single-cell multi-UE MIMO wireless network consisting of a multi-antenna BS, a RIS mounted on the facade of a building, and several heterogeneous UEs ranging from classical mobile phones, to smart-watches and cars. Such a setting is referred to as massive access scenario and is depicted in Fig. 2.1. Note that we study both the downlink, by focusing on the data transmission phase from the BS to the UEs, and the uplink, by considering the channel estimation phase in which the UEs transmit pilot sequences to the BS. The main system parameters and performance metrics are described in the following and summarized in Table 2.1 and Table 2.2, respectively.

We assume that the BS is equipped with M antennas, while the RIS is modeled as an equivalent L-antenna array. Moreover, there are a total of K UEs, which are equipped with N antennas each. We let $\mathbf{\Phi} \triangleq \text{diag}(\alpha_1 e^{j\phi_1}, \ldots, \alpha_\ell e^{j\phi_L}) \in \mathbb{C}^{L\times L}$ with $\phi_\ell \in [0, 2\pi)$, and $|\alpha_\ell|^2 \leq 1$, $\forall \ell$ represent the phase shifts and amplitude attenuation introduced by the RIS, respectively (see, e.g., [52, 63, 83, 90, 91]).

We model the BS as a uniform linear array (ULA) with array response vector for a given steering angle θ defined as

$$\mathbf{a}(\theta) \triangleq [1, e^{j2\pi\delta\cos(\theta)}, \ldots, e^{j2\pi\delta(M-1)\cos(\theta)}]^{\mathrm{T}} \in \mathbb{C}^{M\times 1} \tag{2.1}$$

where $j^2 = -1$ is the imaginary unit and δ is the ratio between the antenna spacing and the signal wavelength. Note that we assume $\delta = 0.5$ unless otherwise stated. In a similar way, we assume that the array at each UE k is a ULA with array response vector given by

$$\mathbf{b}(\theta) \triangleq [1, e^{j2\pi\delta\cos(\theta)}, \ldots, e^{j2\pi\delta(N-1)\cos(\theta)}]^{\mathrm{T}} \in \mathbb{C}^{N\times 1}. \tag{2.2}$$

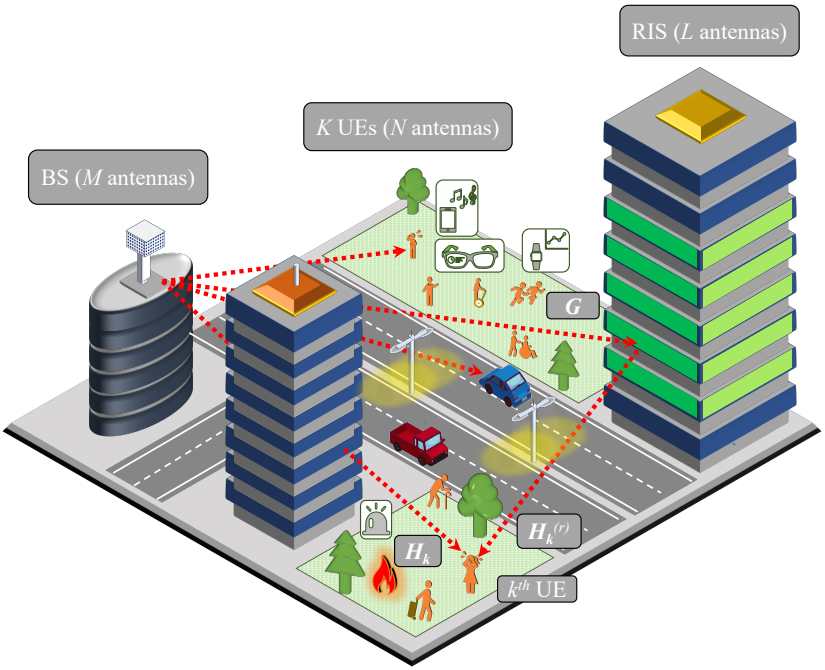

Figure 2.1 – Downlink of the considered beyond-5G massive access scenario.

Finally, the RIS is modelled as a planar linear array (PLA) with L_x and L_y antennas along the x and y axis, respectively, and with $L \triangleq L_x L_y$ whose array response vector for the steering angles ψ_x and ψ_z (i.e., the azimuth and elevation angles, respectively) is given by

$$\begin{aligned}\mathbf{c}(\psi_x,\psi_z) \triangleq &[1, e^{-j2\pi\delta\sin(\psi_z)\cos(\psi_x)},\ldots,e^{-j2\pi\delta(L_y-1)\sin(\psi_z)\cos(\psi_x)}]^{\mathrm{T}} \\ &\otimes [1, e^{-j2\pi\delta\cos(\psi_x)\cos(\psi_z)},\ldots,e^{-j2\pi\delta(L_x-1)\cos(\psi_x)\cos(\psi_z)}]^{\mathrm{T}} \in \mathbb{C}^{L\times 1}. \end{aligned} \tag{2.3}$$

2.1 Channel Model

In this thesis, we do not make any restrictive assumption on the chosen carrier frequency for transmission of data. Indeed, the models presented in this part are applicable to a wide range of frequencies spanning from sub-6GHz, to mmWave. We model the considered channel according to the discrete physical channel model (see, e.g., [92]), whereby the channel matrix between the BS and UE k is defined as

$$\mathbf{H}_k \triangleq \sqrt{\frac{K^r_{H_k}}{1+K^r_{H_k}}}\mathbf{H}_{k,\mathrm{LoS}} + \sqrt{\frac{1}{1+K^r_{H_k}}}\mathbf{H}_{k,\mathrm{NLoS}} \in \mathbb{C}^{N\times M} \tag{2.4}$$

where $K^r_{H_k}$ stands for the Rician factor, while $\mathbf{H}_{k,\mathrm{LoS}}$ is the deterministic LoS path between the BS and UE k, and $\mathbf{H}_{k,\mathrm{NLoS}}$ represents the random non-line-of-sight (NLoS) multipath Rayleigh fading component. In a similar way, we define the channel matrix between the BS and the RIS

Table 2.1 – System parameters.

Parameter	Symbol	Parameter	Symbol	Parameter	Symbol
Number of BS antennas	M	Channel between the BS and UE k	$\mathbf{H}_k$	Noise power	σ_n^2
Number of RIS elements	L	Channel between the BS and the RIS	$\mathbf{G}$	Rician factor	$K_A^r,\ A \in \{H_k, G, H_k^r\}$
Number of UEs	K	Channel between the RIS and UE k	$\mathbf{H}_k^r$	Transmit covariance matrix	$\mathbf{\Gamma}$
Number of UE antennas	N	Channel between the BS and UE k	$\mathbf{H}_k$	Channel covariance matrix of UE k	$\mathbf{\Sigma}_k$
Covariance matrix seen at UE k	$\mathbf{R}_k$	Covariance matrix of UE k seen at the BS	$\mathbf{T}_k$	Pilot sequence p	$\mathbf{P}_p$
Equivalent channel of UE k	$\mathbf{Q}_k$	MMSE estimated of the equivalent channel of UE k	$\hat{\mathbf{Q}}_k$	Data symbol vector of UE k	$\mathbf{s}_k$
Estimated data symbol vector of UE k	$\hat{\mathbf{s}}_k$	Precoding matrix at the BS	$\mathbf{W}$	Receive combining matrix at UE k	$\mathbf{V}_k$
Transmit signal at the BS	$\mathbf{x}$	Number of pilot sequences	P	Transmit power at the BS	$\bar{P}$
LoS pathloss exponent	α	NLoS pathloss exponent	β	Transmit power at UE k	ρ_k

as follows

$$\mathbf{G} \triangleq \sqrt{\frac{K_G^r}{1+K_G^r}}\mathbf{G}_{\text{LoS}} + \sqrt{\frac{1}{1+K_G^r}}\mathbf{G}_{\text{NLoS}} \in \mathbb{C}^{L\times M}. \tag{2.5}$$

The channel matrix between the RIS and UE k is given by

$$\mathbf{H}_k^r \triangleq \sqrt{\frac{K_{H_k^r}^r}{1+K_{H_k^r}^r}}\mathbf{H}_{k,\text{LoS}}^r + \sqrt{\frac{1}{1+K_{H_k^r}^r}}\mathbf{H}_{k,\text{NLoS}}^r \in \mathbb{C}^{L\times N}, \tag{2.6}$$

while we let α and β denote the LoS and NLoS pathloss exponent, respectively.

Let $\mathbf{Q}_k = \left(\mathbf{H}_k^r\right)^{\text{H}}\mathbf{\Phi}\mathbf{G} + \mathbf{H}_k = [\mathbf{q}_{k,1}^{\text{T}}, \ldots, \mathbf{q}_{k,N}^{\text{T}}]^{\text{T}} \in \mathbb{C}^{N\times M}$ denote the equivalent channel between UE k and the BS (which includes the path reflected upon the RIS). We assume a general model whereby the entries of $\mathbf{Q}_k$ satisfy $\text{vec}(\mathbf{Q}_k) \sim \mathscr{CN}(\mathbf{0}, \mathbf{\Sigma}_k)$ [93, Ch.3]: here, the channel covariance matrix $\mathbf{\Sigma}_k \in \mathbb{C}^{NM\times NM}$ may be written as

$$\mathbf{\Sigma}_k \triangleq \begin{bmatrix} \mathbf{\Sigma}_{k,11} & \mathbf{\Sigma}_{k,12} & \cdots & \mathbf{\Sigma}_{k,1M} \\ \mathbf{\Sigma}_{k,12}^{\text{H}} & \mathbf{\Sigma}_{k,22} & & \vdots \\ \vdots & & \ddots & \\ \mathbf{\Sigma}_{k,1M}^{\text{H}} & \cdots & & \mathbf{\Sigma}_{k,MM} \end{bmatrix} \tag{2.7}$$

where $\mathbf{\Sigma}_{k,mn} \triangleq \mathbb{E}[\mathbf{q}_{k,m}\mathbf{q}_{k,n}^{\text{H}}] \in \mathbb{C}^{N\times N}$ represents the cross-covariance matrix between the mth and nth columns of $\mathbf{H}_k$. Lastly, we define the covariance matrix seen by UE k as $\mathbf{R}_k \triangleq \mathbb{E}[\mathbf{Q}_k\mathbf{Q}_k^{\text{H}}] \in \mathbb{C}^{N\times N}$ and the covariance matrix relative to UE k seen at the BS as $\mathbf{T}_k \triangleq \mathbb{E}[\mathbf{Q}_k^{\text{H}}\mathbf{Q}_k] \in \mathbb{C}^{M\times M}$, respectively: observe that, in case of downlink transmission, $\mathbf{R}_k$ and $\mathbf{T}_k$ represent the receive and transmit covariance matrices, respectively. Lastly, we assume that all channels follow a quasi-static flat-fading model and thus remain constant over the transmission time of a codeword. Note that throughout the rest of this thesis we make different assumptions on the availability or not of the CSI at the transmitter/receiver.

2.2 Uplink Pilot-Aided Channel Estimation

Assuming a TDD setting, the channel matrices $\mathbf{G}$, $\mathbf{H}_k^r$, and $\mathbf{H}_k$ are estimated at the BS via antenna-specific uplink pilots, such that N pilot vectors of length τ per UE are required. Let $\bar{P} \leq K$ denote the number of orthogonal pilots and let $\mathscr{S}_p \triangleq \{k : \text{UE } k \text{ has pilot } \mathbf{P}_p\}$ be the set of UEs that share the same pilot matrix $\mathbf{P}_p \in \mathbb{C}^{N\times\tau}$, with $p = 1,\ldots,\bar{P}$, where $\{\mathbf{P}_p\mathbf{P}_p^{\mathrm{H}} = \frac{\tau}{N}\mathbf{I}_N\}_{p=1}^{\bar{P}}$ and $\{\mathbf{P}_p\mathbf{P}_q^{\mathrm{H}} = \mathbf{0}\}_{q\neq p}$: note that N orthogonal pilot vectors are assigned to each UE and these conditions imply $\tau \geq PN$. We use $\mathbf{Y} \in \mathbb{C}^{M\times\tau}$ to denote the receive signal at the BS during the uplink pilot-aided channel estimation phase, which is given by

$$\mathbf{Y} \triangleq \sum_{p=1}^{\bar{P}} \sum_{k\in\mathscr{S}_p} \sqrt{\rho_k}\left(\mathbf{G}^{\mathrm{H}}\boldsymbol{\Phi}^{\mathrm{H}}\mathbf{H}_k^r + \mathbf{H}_k^{\mathrm{H}}\right)\mathbf{P}_p + \mathbf{N} \tag{2.8}$$

where ρ_k is the transmit power of UE k, $\mathbf{N} \in \mathbb{C}^{M\times\tau}$ is the additive white Gaussian noise (AWGN) term with elements distributed as $\mathscr{CN}(0,\sigma_n^2)$. The MMSE estimate of the equivalent channel from the n-th antenna of UE k to the BS (including the path reflected upon the RIS) $\mathbf{q}_{k,n} \in \mathbb{C}^{1\times M}$, with $k \in \mathscr{S}_p$, reads as (see, e.g., [13])

$$\hat{\mathbf{q}}_{k,n}^{\mathrm{H}} \triangleq \frac{N}{\tau\sqrt{\rho_k}}\mathbf{Z}_{k,nn}\mathbf{U}_{k,nn}^{-1}\mathbf{Y}\mathbf{P}_p^{\mathrm{H}}\mathbf{e}_n \in \mathbb{C}^{M\times 1} \tag{2.9}$$

where $\mathbf{Z}_{k,nn} \triangleq \mathbb{E}[\mathbf{q}_{k,n}^{\mathrm{T}}\mathbf{q}_{k,n}^*] \in \mathbb{C}^{M\times M}$ represents the covariance matrix of $\mathbf{q}_{k,n}$, and we have defined the matrix $\mathbf{U}_{k,nn} \triangleq \left(\mathbf{Z}_{k,nn} + \sum_{j\in\mathscr{S}_p\setminus\{k\}}\frac{\rho_j}{\rho_k}\mathbf{Z}_{j,nn} + \frac{N}{\tau\varrho_k}\mathbf{I}_M\right) \in \mathbb{C}^{M\times M}$ and the transmit SNR $\varrho_k \triangleq \rho_k/\sigma_n^2$. Finally, the estimate of the channel matrix $\mathbf{Q}_k$ is given by $\hat{\mathbf{Q}}_k \triangleq [\hat{\mathbf{q}}_{k,1}^{\mathrm{T}},\ldots,\hat{\mathbf{q}}_{k,N}^{\mathrm{T}}]^{\mathrm{T}}$.

The MSE of the channel estimate $\hat{\mathbf{Q}}_k$ of UE k is given by

$$\overline{\mathrm{MSE}}_k \triangleq \frac{1}{N}\sum_{n=1}^{N}\mathbb{E}[\|\hat{\mathbf{q}}_{k,n} - \mathbf{q}_{k,n}\|^2], \tag{2.10}$$

while the normalized mean squared error (NMSE) of $\hat{\mathbf{Q}}_k$ reads as

$$\overline{\mathrm{NMSE}}_k \triangleq \frac{1}{N}\sum_{n=1}^{N}\mathbb{E}\left[\frac{\|\hat{\mathbf{q}}_{k,n} - \mathbf{q}_{k,n}\|^2}{\|\mathbf{q}_{k,n}\|^2}\right]. \tag{2.11}$$

2.3 Downlink Data Transmission

In the downlink, the BS precodes the data symbol vector $\mathbf{s} \triangleq [\mathbf{s}_1^{\mathrm{T}},\ldots,\mathbf{s}_K^{\mathrm{T}}]^{\mathrm{T}} \in \mathbb{C}^{Q\times 1}$, where each $\mathbf{s}_k \in \mathbb{C}^{Q_k\times 1}$ with $\mathbb{E}[\mathbf{s}_k\mathbf{s}_k^{\mathrm{H}}] = \mathbf{I}_{Q_k}$ is intended for UE k and with $Q = \sum_{k=1}^{K} Q_k$, via the multi-UE precoding matrix $\mathbf{W} \triangleq [\mathbf{W}_1,\ldots,\mathbf{W}_K] \in \mathbb{C}^{M\times Q}$ with $\|\mathbf{W}\|_{\mathrm{F}}^2 = P$, where P is the total available transmit power budget at the BS and where each $\mathbf{W}_k \in \mathbb{C}^{M\times Q_k}$ is the precoding matrix associated to

$\mathbf{s}_k$. Let $\mathbf{x} \triangleq \mathbf{W}\mathbf{s} \in \mathbb{C}^{M\times 1}$ denote the transmitted signal at the BS and let us define the transmit covariance matrix as

$$\Gamma \triangleq \mathbb{E}[\mathbf{x}\mathbf{x}^{\mathrm{H}}] \in \mathbb{C}^{M\times M}. \tag{2.12}$$

The receive signal at UE k is defined as

$$\mathbf{y}_k \triangleq \left(\left(\mathbf{H}_k^r\right)^{\mathrm{H}}\mathbf{\Phi}\mathbf{G} + \mathbf{H}_k\right)\mathbf{W}\mathbf{s} + \mathbf{n}_k \tag{2.13}$$

$$= \left(\left(\mathbf{H}_k^r\right)^{\mathrm{H}}\mathbf{\Phi}\mathbf{G} + \mathbf{H}_k\right)\mathbf{W}_k\mathbf{s}_k + \sum_{j\neq k}\left(\left(\mathbf{H}_k^r\right)^{\mathrm{H}}\mathbf{\Phi}\mathbf{G} + \mathbf{H}_k\right)\mathbf{W}_j\mathbf{s}_j + \mathbf{n}_k \in \mathbb{C}^{N\times 1} \tag{2.14}$$

where $\mathbf{n}_k \in \mathbb{C}^{N\times 1}$ is the AWGN term at UE k, which is assumed to be independent from all the channel matrices and distributed as $\mathscr{CN}(\mathbf{0}, \sigma_n^2\mathbf{I}_N)$. Moreover, note that in Eq. (2.14) we have explicited the useful signal part plus inter-UE interference and noise. Each UE k estimates its data symbol vector as $\hat{\mathbf{s}}_k \triangleq \mathbf{V}_k^{\mathrm{H}}\mathbf{y}_k$, where $\mathbf{V}_k \triangleq [\mathbf{v}_{k,1}, \ldots, \mathbf{v}_{k,Q_k}] \in \mathbb{C}^{N\times Q_k}$ with $\|\mathbf{V}_k\|_{\mathrm{F}}^2 = 1$ is the corresponding combining matrix.

Hence, the receive SINR at UE k relative to symbol $s_{k,q}$ is expressed as

$$\mathrm{SINR}_{k,q} \triangleq \frac{\left|\mathbf{v}_{k,q}^{\mathrm{H}}\left(\left(\mathbf{H}_k^r\right)^{\mathrm{H}}\mathbf{\Phi}\mathbf{G} + \mathbf{H}_k\right)\mathbf{w}_{k,q}\right|^2}{\sum_{(j,r)\neq(k,q)}\left|\mathbf{v}_{k,q}^{\mathrm{H}}\left(\left(\mathbf{H}_k^r\right)^{\mathrm{H}}\mathbf{\Phi}\mathbf{G} + \mathbf{H}_k\right)\mathbf{w}_{j,r}\right|^2 + \|\mathbf{v}_{k,q}\|^2\sigma_n^2}. \tag{2.15}$$

The system sum rate is thus defined as

$$R = \sum_{k=1}^{K}\sum_{q=1}^{Q_k}\log_2\left(1 + \frac{\left|\mathbf{v}_{k,q}^{\mathrm{H}}\left(\left(\mathbf{H}_k^r\right)^{\mathrm{H}}\mathbf{\Phi}\mathbf{G} + \mathbf{H}_k\right)\mathbf{w}_{k,q}\right|^2}{\sum_{(j,r)\neq(k,q)}\left|\mathbf{v}_{k,q}^{\mathrm{H}}\left(\left(\mathbf{H}_k^r\right)^{\mathrm{H}}\mathbf{\Phi}\mathbf{G} + \mathbf{H}_k\right)\mathbf{w}_{j,r}\right|^2 + \|\mathbf{v}_{k,q}\|^2\sigma_n^2}\right). \tag{2.16}$$

We define the receive MSE of UE k as

$$\mathrm{MSE}_k = \mathbb{E}[\|\hat{\mathbf{s}}_k - \mathbf{s}_k\|^2] \tag{2.17}$$

$$= \mathbb{E}[\|\mathbf{V}_k^{\mathrm{H}}\mathbf{y}_k - \mathbf{s}_k\|^2]. \tag{2.18}$$

The receive SMSE over all UEs is thus expressed as

$$\mathrm{SMSE} = \sum_k \mathrm{MSE}_k. \tag{2.19}$$

Table 2.2 – Performance metrics.

Parameter	**Symbol**	**Parameter**	**Symbol**
Sum rate	R	Receive SINR at UE k for symbol q	$\text{SINR}_{k,q}$
Received MSE at UE k	MSE_k	Receive SMSE	$\overline{\text{SMSE}}$
MSE of the channel estimate of UE k	$\overline{\text{MSE}}_k$	NMSE of the channel estimate of UE k	$\overline{\text{NMSE}}_k$

Part II

Covariance Shaping

Chapter 3

Introduction

The exploitation of statistical CSI is of paramount importance in massive MIMO systems, where instantaneous channel estimation can give rise to a major signaling overhead limiting the network performance. In the existing literature, statistical CSI is used for tasks such as pilot decontamination and statistical beamforming by assuming: i) signal subspace separation among the UEs, which is rarely realized in practice and is generally beyond the control of the network designer (as it is dictated by the physical scattering environment); and ii) the so-called Kronecker channel structure, which has been shown to be an over-simplification in most cases.

Building on the fact that most current and future UEs are, and will be, equipped with a small-to-moderate number of antennas, we propose a novel statistical beamforming technique at the UEs-side, referred to as *covariance shaping*. While existing methods assume statistical orthogonality among the UEs as a property given by the physical scattering environment and the Kronecker channel model due to its analytical tractability, covariance shaping aims at modifying the channel statistics of the UEs in order to enforce signal subspace separation in any given network scenario. The proposed approach targets a suitable shaping of the covariance matrix performed at the UE-side and relies uniquely on statistical CSI. Specifically, it consists in preemptively applying a statistical beamforming at each UE during both the uplink pilot-aided channel estimation phase and the downlink data transmission phase, aiming at enforcing a separation of the signal subspaces of the UEs that would be otherwise highly overlapping. In this context, each UE exploits its antennas to excite only a subset of all the possible propagation directions towards the BS such that the spatial correlation with interfering UEs is minimized while preserving enough useful power for effective data transmission. Hence, covariance shaping is suitable for both pilot decontamination in TDD systems and statistical precoding. Remarkably, the proposed method exploits the realistic non-Kronecker channel structure that allows to suitably alter the channel statistics perceived at the BS by acting at the UE-side. Therefore, it has the unique advantage of turning the generally

inconvenient non-Kronecker nature of massive MIMO channels into a benefit. Numerical results show the sum-rate performance gains with respect to reference scenarios employing the multiple antennas at the UEs for spatial multiplexing.

The covariance shaping framework was initially proposed in our prior work [20, 21] and recently used in the context of minimization of the outage probability in [94]. In this work, the authors propose to design a statistical receive beamforming by extending the metric proposed in [20] to all pairs of interfering UEs, together with the design of a statistical precoding at the BS. Differently from [94], we argue that covariance shaping must be adopted for *both* pilot decontamination during the uplink pilot-aided channel estimation phase and receive combining during the downlink data transmission phase. By doing so, the BS is able to acquire accurate instantaneous effective channel estimates, which are then used for efficient downlink precoding and result in greatly enhanced network performance.

The contributions of this part are summarized as follows.

- We present the novel concept of covariance shaping, which aims at designing a suitable shaping of the covariance matrices of the UEs to enforce a full or partial separation of their signal subspaces, which would be otherwise highly overlapping.

- We point out how exploiting the non-Kronecker nature of massive MIMO channels is crucial to suitably alter the channel statistics perceived at the BS by acting at the UE-side.

- We derive a tractable expression of the ergodic achievable sum rate under covariance shaping with the objective of characterizing the impact of the proposed framework on the system performance.

- We optimize the covariance shaping strategies by minimizing the variance of the inter-UE interference (as a metric to measure the spatial correlation) among all the interfering UEs. To this end, we propose a low-complexity iterative best-response algorithm that is proved to converge to a to a stationary point of the original problem in the case of two UEs and to a limit point in the case of more than two UEs.

- We provide numerical results highlighting the superior sum-rate performance of covariance shaping with respect to reference scenarios where the multiple antennas at the UE are employed for spatial multiplexing.

3.1 System Model

3.1.1 Channel model

As a special case of the system model described in Chapter 2, we consider only the direct channel between the BS and each UE k, which is given by $\mathbf{H}_k \triangleq [\mathbf{h}_{k,1},\ldots,\mathbf{h}_{k,M}] = [\mathbf{g}_{k,1}^{\mathrm{T}},\ldots,\mathbf{g}_{k,N}^{\mathrm{T}}]^{\mathrm{T}} \in \mathbb{C}^{N\times M}$, where $\mathbf{h}_{k,m} \in \mathbb{C}^{N\times 1}$ and $\mathbf{g}_{k,n} \in \mathbb{C}^{1\times M}$ are the channel vectors between the mth BS antenna and UE k and between the BS and the nth antenna of UE k, respectively. As mentioned above, we assume a general channel model where the entries of $\mathbf{H}_k$ satisfy $\mathrm{vec}(\mathbf{H}_k) \sim \mathscr{CN}(\mathbf{0},\mathbf{\Sigma}_k)$, with the channel covariance matrix $\mathbf{\Sigma}_k \in \mathbb{C}^{NM\times NM}$ defined in Eq. (2.7).

3.1.2 Uplink pilot-aided channel estimation

As described in Chapter 2, the channel matrices $\{\mathbf{H}_k\}_{k=1}^K$ are estimated at the BS via $\bar{P}$ orthogonal uplink pilots, with $\bar{P} < K$. The receive signal at the BS during the uplink pilot-aided channel estimation phase is defined as (cf. Eq. (2.8))

$$\mathbf{Y} \triangleq \sum_{p=1}^{\bar{P}} \sum_{k\in\mathscr{S}_p} \sqrt{\rho_k}\mathbf{H}_k\mathbf{P}_p + \mathbf{N}, \tag{3.1}$$

while MMSE estimate of $\mathbf{g}_{k,n}$, with $k \in \mathscr{S}_p$ is given by Eq. (2.9).[1]. Finally, the estimate of $\mathbf{H}_k$ is obtained as $\hat{\mathbf{H}}_k \triangleq [\hat{\mathbf{g}}_{k,1}^{\mathrm{T}},\ldots,\hat{\mathbf{g}}_{k,N}^{\mathrm{T}}]^{\mathrm{T}}$.

3.1.3 Downlink data transmission

Focusing on the downlink data transmission, the receive signal at UE k $\mathbf{y}_k$ is expressed as in Eq. (2.14) while the resulting sum rate is given by (cf. Eq. (2.16))

$$R \triangleq \sum_{k=1}^{K}\sum_{q=1}^{Q_k} \log_2\left(1 + \frac{|\mathbf{v}_{k,q}^{\mathrm{H}}\mathbf{H}_k\mathbf{w}_{k,q}|^2}{\sum_{(j,r)\neq(k,q)}|\mathbf{v}_{k,q}^{\mathrm{H}}\mathbf{H}_k\mathbf{w}_{j,r}|^2 + \|\mathbf{v}_{k,q}\|^2\sigma_n^2}\right). \tag{3.2}$$

[1] Note that since in this part we consider only the direct link between the BS and the UEs we have that $\mathbf{q}_{k,n} \equiv \mathbf{g}_{k,n}$.

Chapter 4

Covariance Shaping: Enforcing Favorable Propagation in Massive MIMO Systems

4.1 Covariance Shaping at The UE-Side

In a massive MIMO setting, the BS can spatially separate the signals corresponding to different UEs if their covariance matrices lie on orthogonal supports, i.e., if $\mathbf{\Sigma}_k \mathbf{\Sigma}_j = \mathbf{0}$ for a given pair of UEs k and j. However, the degree of spatial orthogonality between UEs is determined by the positions of the latter combined with the physical scattering environment, where both these factors are generally beyond the control of the network designer. Hence, signal subspace separation among the UEs is rarely realized in practice [13]. In this context, we propose a novel method relying uniquely on statistical CSI, referred to as *covariance shaping*, which is applied at the UE-side to enforce the aforementioned signal subspace separation in any given network scenario. According to covariance shaping, the UEs preemptively apply a statistical transmit/receive beamforming vector (different for each UE) that aims at spatially separating their transmissions, thus drastically reducing both the pilot contamination and the interference. Here, the original MIMO channel of each UE is transformed into an effective multiple-input single-output (MISO) channel by combining the transmit/receive signal with the corresponding covariance shaping vector. Remarkably, the proposed method exploits the realistic non-Kronecker channel structure and allows to suitably alter the channel statistics perceived at the BS by acting at the UE-side, thus turning a generally inconvenient model into a benefit.

Let $\mathbf{v}_k \in \mathbb{C}^{N\times 1}$ denote the statistical beamforming vector preemptively applied by UE k: in the rest of this part, we refer to $\mathbf{v}_k$ as *covariance shaping vector*. Hence, the MIMO channel $\mathbf{H}_k$ between the BS and each UE k is transformed into the effective MISO channel $\bar{\mathbf{g}}_k \triangleq \mathbf{v}_k^{\mathrm{H}} \mathbf{H}_k \in \mathbb{C}^{1\times M}$. In this setting, it follows that $\bar{\mathbf{g}}_k \sim \mathcal{CN}(\mathbf{0}, \bar{\mathbf{\Phi}}_k)$, where $\bar{\mathbf{\Phi}}_k \in \mathbb{C}^{M\times M}$ is the effective

covariance matrix defined as

$$\bar{\mathbf{\Phi}}_k \triangleq \mathbb{E}[\bar{\mathbf{g}}_k^{\mathrm{T}} \bar{\mathbf{g}}_k^*] \tag{4.1}$$

$$= \left((\mathbf{I}_M \otimes \mathbf{v}_k^{\mathrm{H}}) \mathbf{\Sigma}_k (\mathbf{I}_M \otimes \mathbf{v}_k)\right)^{\mathrm{T}} \tag{4.2}$$

with $\mathbf{\Sigma}_k$ introduced in Eq. (2.7) and where $\mathbb{E}[\|\bar{\mathbf{g}}_k\|^2] = \mathrm{tr}(\bar{\mathbf{\Phi}}_k)$. In the rest of this section, we describe how the two phases of uplink pilot-aided channel estimation and downlink data transmission are modified under covariance shaping and we provide a tractable expression of the resulting ergodic achievable sum rate. The optimization of the covariance shaping vectors is discussed in Section 4.2.

4.1.1 Uplink pilot-aided channel estimation

To estimate the effective channels resulting from covariance shaping, the BS assigns the same pilot vector $\mathbf{p}_p \in \mathbb{C}^{1\times\tau}$ to all UEs $k \in \mathscr{S}_p$, with $\{\|\mathbf{p}_p\|^2 = \tau\}_{p=1}^P$ and $\{\mathbf{p}_p \mathbf{p}_q^{\mathrm{H}} = 0\}_{p\neq q}$. We use $\bar{\mathbf{Y}} \in \mathbb{C}^{M\times\tau}$ to denote the receive signal at the BS during the uplink pilot-aided channel estimation phase, which is given by (cf. Eq. (2.8))

$$\bar{\mathbf{Y}} \triangleq \sum_{p=1}^{P} \sum_{k\in\mathscr{S}_p} \sqrt{\rho_k}\, \bar{\mathbf{g}}_k^{\mathrm{H}} \mathbf{p}_p + \mathbf{N}. \tag{4.3}$$

Then, the MMSE estimate of $\bar{\mathbf{g}}_k$, with $k \in \mathscr{S}_p$, reads as (cf. Eq. (2.9))

$$\hat{\bar{\mathbf{g}}}_k^{\mathrm{H}} \triangleq \frac{1}{\tau\sqrt{\rho_k}} \bar{\mathbf{\Phi}}_k \mathbf{U}_k^{-1} \bar{\mathbf{Y}} \mathbf{p}_p^{\mathrm{H}} \tag{4.4}$$

where we have defined $\mathbf{U}_k \triangleq \left(\bar{\mathbf{\Phi}}_k + \sum_{j\in\mathscr{S}_p\setminus\{k\}} \frac{\rho_j}{\rho_k} \bar{\mathbf{\Phi}}_j + (\tau\rho_k)^{-1}\mathbf{I}_M\right) \in \mathbb{C}^{M\times M}$.

4.1.2 Downlink data transmission

Focusing on the downlink data transmission, the BS now transmits only one symbol $s_k \in \mathbb{C}$ to each UE k, i.e., $\{Q_k = 1\}_{k=1}^K$: hence, we have $\mathbf{s} = [s_1, \ldots, s_K]^{\mathrm{T}} \in \mathbb{C}^{K\times 1}$ and the multi-UE precoding matrix becomes $\mathbf{W} = [\mathbf{w}_1, \ldots, \mathbf{w}_K] \in \mathbb{C}^{M\times K}$, where $\mathbf{w}_k \in \mathbb{C}^{M\times 1}$ is the precoding vector corresponding to s_k. The receive signal at UE k is thus given by (cf. Eq. (2.13)–(2.14))

$$\bar{y}_k \triangleq \bar{\mathbf{g}}_k \mathbf{W}\mathbf{s} + \mathbf{v}_k^{\mathrm{H}} \mathbf{n}_k \tag{4.5}$$

$$= \bar{\mathbf{g}}_k \mathbf{w}_k s_k + \sqrt{\rho_{\mathrm{BS}}} \sum_{j\neq k} \bar{\mathbf{g}}_k \mathbf{w}_j s_j + \mathbf{v}_k^{\mathrm{H}} \mathbf{n}_k \tag{4.6}$$

and the resulting sum rate is given by (cf. Eq. (2.16))

$$\bar{R} \triangleq \sum_{k=1}^{K} \log_2 \left(1 + \frac{|\bar{\mathbf{g}}_k \mathbf{w}_k|^2}{\sum_{j \neq k} |\bar{\mathbf{g}}_k \mathbf{w}_j|^2 + \sigma_n^2 \|\mathbf{v}_k\|^2}\right). \tag{4.7}$$

4.1.3 Ergodic achievable sum rate

We now analyze the sum rate as a function of the covariance shaping vectors with the objective of characterizing the impact of the proposed framework on the system performance. In particular, we derive a tractable expression of the ergodic achievable sum rate by assuming that each UE k does not know the effective scalar channel $\bar{\mathbf{g}}_k \mathbf{w}_k = \mathbf{v}_k^{\mathrm{H}} \mathbf{H}_k \mathbf{w}_k$ instantaneously but only its expected value. Building on the results in [11–13, 95], we can express the receive signal in Eq. (4.6) as

$$\bar{y}_k = \mathbb{E}[\bar{\mathbf{g}}_k \mathbf{w}_k] s_k + \left(\bar{\mathbf{g}}_k \mathbf{w}_k - \mathbb{E}[\bar{\mathbf{g}}_k \mathbf{w}_k]\right) s_k + \sum_{j \neq k} \bar{\mathbf{g}}_k \mathbf{w}_j s_j + \mathbf{v}_k^{\mathrm{H}} \mathbf{n}_k \tag{4.8}$$

$$= \mathbb{E}[\bar{\mathbf{g}}_k \mathbf{w}_k] s_k + n'_k \tag{4.9}$$

where the effective noise term $n'_k \triangleq \left(\bar{\mathbf{g}}_k \mathbf{w}_k - \mathbb{E}[\bar{\mathbf{g}}_k \mathbf{w}_k]\right) s_k + \sum_{j \neq k} \bar{\mathbf{g}}_k \mathbf{w}_j s_j + \mathbf{v}_k^{\mathrm{H}} \mathbf{n}_k$ accounts for the lack of instantaneous CSIT in addition to the interference and the noise at UE k. Hence, we define the effective SINR at UE k as

$$\overline{\mathrm{SINR}}_k \triangleq \frac{\left|\mathbb{E}[\bar{\mathbf{g}}_k \mathbf{w}_k]\right|^2}{\mathrm{Var}[\bar{\mathbf{g}}_k \mathbf{w}_k] + \sum_{j \neq k} \mathbb{E}\left[|\bar{\mathbf{g}}_k \mathbf{w}_j|^2\right] + \varrho_{\mathrm{BS}}^{-1} \|\mathbf{v}_k\|^2} \tag{4.10}$$

which is obtained by assuming the worst-case scenario of Gaussian-distributed effective noise z'_k.

The expression in Eq. (4.10) can be further simplified by considering the case where the BS adopts maximum-ratio transmission (MRT) precoding. In this setting, the multi-UE precoding matrix can be written as

$$\mathbf{W} = P \frac{\hat{\bar{\mathbf{G}}}^{\mathrm{H}}}{\sqrt{\mathbb{E}[\|\bar{\mathbf{G}}\|_{\mathrm{F}}^2]}} \tag{4.11}$$

where $\bar{\mathbf{G}} \triangleq [\bar{\mathbf{g}}_1^{\mathrm{T}}, \ldots, \bar{\mathbf{g}}_K^{\mathrm{T}}]^{\mathrm{T}} \in \mathbb{C}^{K \times M}$ and $\hat{\bar{\mathbf{G}}} \triangleq [\hat{\bar{\mathbf{g}}}_1^{\mathrm{T}}, \ldots, \hat{\bar{\mathbf{g}}}_K^{\mathrm{T}}]^{\mathrm{T}} \in \mathbb{C}^{K \times M}$ contain, respectively, the effective channels and their MMSE estimates defined in Eq. (4.4). Hence, the effective SINR in

Eq. (4.10) becomes

$$\overline{\mathrm{SINR}}_k = \frac{\left|\mathbb{E}[\bar{\mathbf{g}}_k \hat{\bar{\mathbf{g}}}_k^{\mathrm{H}}]\right|^2}{\mathrm{Var}[\bar{\mathbf{g}}_k \hat{\bar{\mathbf{g}}}_k^{\mathrm{H}}] + \sum_{j\neq k} \mathbb{E}\left[|\bar{\mathbf{g}}_k \hat{\bar{\mathbf{g}}}_j^{\mathrm{H}}|^2\right] + \varrho_{\mathrm{BS}}^{-1} \|\mathbf{v}_k\|^2 \mathbb{E}\left[\|\bar{\mathbf{G}}\|_{\mathrm{F}}^2\right]} \tag{4.12}$$

$$= \frac{\left(\mathrm{tr}(\bar{\mathbf{\Phi}}_k \mathbf{U}_k^{-1} \bar{\mathbf{\Phi}}_k)\right)^2}{\sum_{j=1}^K \mathrm{tr}(\bar{\mathbf{\Phi}}_k \bar{\mathbf{\Phi}}_j \mathbf{U}_j^{-1} \bar{\mathbf{\Phi}}_j) + \sum_{j\neq k} \mathbb{1}_{\mathscr{S}_p}(k,j) \mathrm{tr}(\bar{\mathbf{\Phi}}_k \mathbf{U}_j^{-1} \bar{\mathbf{\Phi}}_j)^2 + \varrho_{\mathrm{BS}}^{-1} \|\mathbf{v}_k\|^2 \sum_j \mathrm{tr}(\bar{\mathbf{\Phi}}_j)} \tag{4.13}$$

where we have defined the transmit SNR at the BS as $\varrho_{\mathrm{BS}}^{-1} \triangleq P/\sigma_n^2$ and Eq. (4.13) follows from plugging $\mathbb{E}[\bar{\mathbf{g}}_k \hat{\bar{\mathbf{g}}}_k^{\mathrm{H}}] = \mathrm{tr}(\bar{\mathbf{\Phi}}_k \mathbf{U}_k^{-1} \bar{\mathbf{\Phi}}_k)$, $\mathrm{Var}[\bar{\mathbf{g}}_k \hat{\bar{\mathbf{g}}}_k^{\mathrm{H}}] = \mathrm{tr}(\bar{\mathbf{\Phi}}_k \bar{\mathbf{\Phi}}_k \mathbf{U}_k^{-1} \bar{\mathbf{\Phi}}_k)$, $\mathbb{E}\left[|\bar{\mathbf{g}}_k \hat{\bar{\mathbf{g}}}_j^{\mathrm{H}}|^2\right] = \mathrm{tr}(\bar{\mathbf{\Phi}}_k \bar{\mathbf{\Phi}}_j \mathbf{U}_j^{-1} \bar{\mathbf{\Phi}}_j)$ $+\mathbb{1}_{\mathscr{S}_p}(k,j)\mathrm{tr}(\bar{\mathbf{\Phi}}_k \mathbf{U}_j^{-1} \bar{\mathbf{\Phi}}_j)^2$, and $\mathbb{E}[\|\bar{\mathbf{G}}\|_{\mathrm{F}}^2] = \sum_k \mathrm{tr}(\bar{\mathbf{\Phi}}_k)$ into Eq. (4.12); we refer to Appendix A for the full derivations. Note that, in the case of perfect channel estimation (i.e., when $\varrho_k \to \infty$ and all the UEs have orthogonal pilots), we have $\bar{\mathbf{\Phi}}_k \mathbf{U}_k^{-1} \bar{\mathbf{\Phi}}_k = \bar{\mathbf{\Phi}}_k$, $\bar{\mathbf{\Phi}}_j \mathbf{U}_j^{-1} \bar{\mathbf{\Phi}}_j = \bar{\mathbf{\Phi}}_j$, and $j \notin \mathscr{S}_p$ (which yields $\mathbb{1}_{\mathscr{S}_p}(k,j) = 0$). In this context, the effective SINR in Eq. (4.13) can be simplified as

$$\overline{\mathrm{SINR}}_k = \frac{\left(\mathrm{tr}(\bar{\mathbf{\Phi}}_k)\right)^2}{\sum_{j=1}^K \mathrm{tr}(\bar{\mathbf{\Phi}}_k \bar{\mathbf{\Phi}}_j) + \varrho_{\mathrm{BS}}^{-1} \|\mathbf{v}_k\|^2 \sum_j \mathrm{tr}(\bar{\mathbf{\Phi}}_j)}. \tag{4.14}$$

Finally, the ergodic achievable sum rate is obtained according to the following proposition (the proof follows from [12, Sec. C] and is thus omitted).

Proposition 1. *Assume that the BS adopts MRT precoding. Then, the following is an ergodic achievable sum rate:*

$$\bar{R}^{\mathrm{lb}} = \sum_{k=1}^K \log_2(1 + \overline{\mathrm{SINR}}_k) \tag{4.15}$$

with γ_k defined in Eq. (4.13) *for the case of imperfect channel estimation and in Eq.* (4.14) *for the case of perfect channel estimation. Furthermore, the expression in Eq.* (4.15) *satisfies*

$$\lim_{M\to\infty} \bar{R}^{\mathrm{lb}} = \mathbb{E}[\bar{R}] \tag{4.16}$$

with $\bar{R}$ defined in Eq. (4.7).

Considering the NLoS scenario with $K = 2$ and $N = 2$ depicted in Fig. 4.2(a) and the resulting covariance shaping vectors, Fig. 4.1 compares the sum rate in Eq. (4.7) (obtained via Monte Carlo simulations averaged over 10^3 independent channel realizations) and the ergodic achievable sum rate in Eq. (4.15) as functions of the number of BS antennas M. Here, we consider MRT precoding at the BS and different values of transmit SNR at the BS ϱ_{BS}. Indeed, as observed from Fig. 4.1(b), the normalized difference between the simulated average sum rate and the ergodic achievable sum rate decreases as M grows (i.e., Eq. (4.15) becomes increasingly more accurate), which demonstrates the validity of Proposition 1.

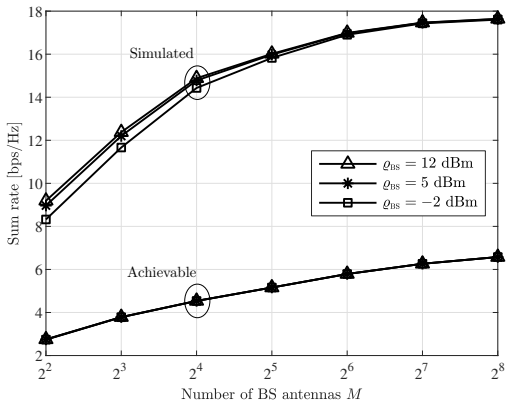

(a) Simulated average sum rate in Eq. (4.7) and ergodic achievable sum rate in Eq. (4.15).

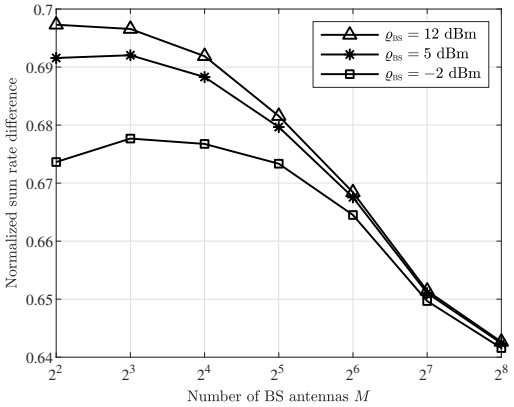

(b) Normalized difference between the simulated average sum rate in Eq. (4.7) and the ergodic achievable sum rate in Eq. (4.15).

Figure 4.1 – Simulated average sum rate and ergodic achievable sum rate (left) and their normalized difference (right) versus the number of BS antennas M for the NLoS scenario with $K = 2$ and $N = 2$ depicted in Fig. 4.2(a), MRT precoding at the BS, and different values of the transmit SNR at the BS ϱ_{BS}.

4.2 Covariance Shaping Optimization

In this section, we aim at maximizing the sum rate through a proper choice of the covariance shaping vectors at the UEs. To this end, we consider the variance of the inter-UE interference as a metric to measure the spatial correlation (or, in other words, the degree of statistical orthogonality) between two interfering UEs. In the following, we first consider the simple case of $K = 2$ and then extend the resulting analysis to the general case of $K \geq 2$.

Let us define the inter-UE interference between UEs k and j after applying covariance shaping as

$$\Omega(\mathbf{v}_k, \mathbf{v}_j) \triangleq \frac{\bar{\mathbf{g}}_k(\mathbf{v}_k)\bar{\mathbf{g}}_j^{\text{H}}(\mathbf{v}_j)}{\sqrt{\mathbb{E}\big[\|\bar{\mathbf{g}}_k(\mathbf{v}_k)\|^2\big]\mathbb{E}\big[\|\bar{\mathbf{g}}_j(\mathbf{v}_j)\|^2\big]}} \tag{4.17}$$

where we have made explicit the dependence of the effective channels on the corresponding covariance shaping vectors.

The effective channel vectors of UEs k and j yield asymptotic *favorable propagation* if they satisfy [96]

$$\lim_{M\to\infty} \Omega(\mathbf{v}_k, \mathbf{v}_j) = 0. \tag{4.18}$$

For a practical number of antennas M, a meaningful performance metric is the variance of

$\Omega(\mathbf{v}_k, \mathbf{v}_j)$, expressed as

$$\delta(\mathbf{v}_k, \mathbf{v}_j) \triangleq \mathrm{Var}\big[\Omega(\mathbf{v}_k, \mathbf{v}_j)\big] \tag{4.19}$$

$$= \frac{\mathrm{tr}\big(\bar{\mathbf{\Phi}}_k(\mathbf{v}_k)\bar{\mathbf{\Phi}}_j(\mathbf{v}_j)\big)}{\mathrm{tr}\big(\bar{\mathbf{\Phi}}_k(\mathbf{v}_k)\big)\mathrm{tr}\big(\bar{\mathbf{\Phi}}_j(\mathbf{v}_j)\big)} \tag{4.20}$$

where we have made explicit the dependence of the effective covariance matrices on the corresponding covariance shaping vectors. Note that the terms in Eq. (4.20) can be written as

$$\mathrm{tr}\big(\bar{\mathbf{\Phi}}_k(\mathbf{v}_k)\big) = \mathbf{v}_k^{\mathrm{H}}\Big(\sum_{m=1}^{M} \mathbf{\Sigma}_{k,mm}\Big)\mathbf{v}_k, \tag{4.21}$$

$$\mathrm{tr}\big(\bar{\mathbf{\Phi}}_k(\mathbf{v}_k)\bar{\mathbf{\Phi}}_j(\mathbf{v}_j)\big) = \sum_{m,n=1}^{M} \mathbf{v}_k^{\mathrm{H}}\mathbf{\Sigma}_{k,mn}\mathbf{v}_k\mathbf{v}_j^{\mathrm{H}}\mathbf{\Sigma}_{j,nm}\mathbf{v}_j \tag{4.22}$$

$$= \sum_{m,n=1}^{M} \mathbf{v}_k^{\mathrm{H}}\mathbf{\Sigma}_{k,mn}\mathbf{v}_k\mathbf{v}_j^{\mathrm{H}}\mathbf{\Sigma}_{j,mn}^{\mathrm{H}}\mathbf{v}_j. \tag{4.23}$$

where we recall that $\mathbf{\Sigma}_{k,mn}$ represents the cross-covariance matrix between the mth and nth columns of the original channel $\mathbf{H}_k$, i.e., before applying covariance shaping (see Eq. (2.7)). Observe that $\delta(\mathbf{v}_k, \mathbf{v}_j) = 0$ implies $\bar{\mathbf{\Phi}}_k\bar{\mathbf{\Phi}}_j = \mathbf{0}$, i.e., that $\bar{\mathbf{\Phi}}_k$ and $\bar{\mathbf{\Phi}}_j$ lie on orthogonal supports [13]. Indeed, considering the eigenvalue decomposition of the effective covariance matrices, which may be written as $\{\bar{\mathbf{\Phi}}_i = \mathbf{U}_i\Lambda_i\mathbf{U}_i^{\mathrm{H}}\}_{i\in\{k,j\}}$, the condition of statistical orthogonality requires $\mathbf{U}_k = \mathbf{U}_j$ and $\mathrm{tr}(\Lambda_k\Lambda_j) = 0$ (i.e., $\bar{\mathbf{\Phi}}_k$ and $\bar{\mathbf{\Phi}}_j$ need to be rank-deficient). Clearly, in the general case, this imposes M^2 conditions whereas only $2N$ variables can be adjusted: this means that the resulting system of equations can be solved when $N \geq M^2/2$, which is generally not verified in practice since $M \gg KN$ in massive MIMO scenarios. Hence, while full signal subspace separation can hardly be achieved by simply acting at the UE-side, it is of interest to minimize the spatial correlation between each pair of UEs.

4.2.1 Two-UE case

In the two-UE case (i.e., $K = 2$), the covariance shaping vectors of UEs k and j are computed by solving the optimization problem

Problem 1 (P1_CS)**.**

$$\min_{\{\mathbf{v}_k, \mathbf{v}_j\}} \delta(\mathbf{v}_k, \mathbf{v}_j) \tag{4.24}$$

$$\text{s.t.} \quad \|\mathbf{v}_k\|^2 = \|\mathbf{v}_j\|^2 = 1 \tag{4.25}$$

with $\delta(\mathbf{v}_k, \mathbf{v}_j)$ defined in Eq. (4.20). Although Problem 1 is not jointly convex in $\{\mathbf{v}_k, \mathbf{v}_j\}$, it can

Algorithm 1 Covariance shaping: Alternating optimization algorithm

Initialize $\mathbf{v}_k^{(0)}$, $\mathbf{v}_j^{(0)}$, and ξ.
$n \leftarrow 1$
while $\left|\left(\delta(\mathbf{v}_k^{(n)},\mathbf{v}_j^{(n)}) - \delta(\mathbf{v}_k^{(n-1)},\mathbf{v}_j^{(n-1)})\right)\right| / \delta(\mathbf{v}_k^{(n)},\mathbf{v}_j^{(n)}) > \xi$ **do**
    Given $\mathbf{v}_j^{(n-1)}$, compute $\{\eta_{j,mn}(\mathbf{v}_j^{(n-1)})\}_{m,n=1}^{M}$ as in Eq. (4.26).
    Compute $\mathbf{v}_k^{(n)}$ as in Eq. (4.28).
    Given $\mathbf{v}_k^{(n)}$, compute $\{\eta_{k,mn}(\mathbf{v}_k^{(n)})\}_{m,n=1}^{M}$ as in Eq. (4.26).
    Compute $\mathbf{v}_j^{(n)}$ as in Eq. (4.28).
    Compute $\delta(\mathbf{v}_k^{(n)},\mathbf{v}_j^{(n)})$ as in Eq. (4.20).
end while
Fix $\mathbf{v}_k = \mathbf{v}_k^{(n)}$ and $\mathbf{v}_j = \mathbf{v}_j^{(n)}$.

be efficiently solved via alternating optimization (as done in [20]). Let us begin by defining

$$\eta_{j,mn}(\mathbf{v}_j) \triangleq \frac{\mathbf{v}_j^{\mathrm{H}} \boldsymbol{\Sigma}_{j,mn}^{\mathrm{H}} \mathbf{v}_j}{\mathbf{v}_j^{\mathrm{H}} \left(\sum_{m=1}^{M} \boldsymbol{\Sigma}_{j,mm}\right) \mathbf{v}_j}. \tag{4.26}$$

The optimal covariance shaping vector of UE k for a given $\mathbf{v}_j$, denoted by $\mathbf{v}_k^{\star}$, is obtained as

$$\mathbf{v}_k^{\star} = \underset{\mathbf{v}_k}{\operatorname{argmin}} \frac{\sum_{m,n=1}^{M} \mathbf{v}_k^{\mathrm{H}} \left(\eta_{j,mn}(\mathbf{v}_j) \boldsymbol{\Sigma}_{k,mn}\right) \mathbf{v}_k}{\mathbf{v}_k^{\mathrm{H}} \left(\sum_{m=1}^{M} \boldsymbol{\Sigma}_{k,mm}\right) \mathbf{v}_k}. \tag{4.27}$$

Since Eq. (4.27) is in the form of generalized Rayleigh quotient, it admits the solution

$$\mathbf{v}_k^{\star} = \mathbf{u}_{\min}\left(\left(\sum_{m=1}^{M} \boldsymbol{\Sigma}_{k,mm}\right)^{-1} \left(\sum_{m,n=1}^{M} \eta_{j,mn}(\mathbf{v}_j) \boldsymbol{\Sigma}_{k,mn}\right)\right) \tag{4.28}$$

and the optimal covariance shaping vector of UE j for a given $\mathbf{v}_k$ is obtained in a similar way. Hence, Problem 1 is solved by alternating the optimization between $\mathbf{v}_k$ and $\mathbf{v}_j$ until a predetermined convergence criterion is satisfied (e.g., until the difference between the values of the objective between consecutive iterations is sufficiently small). This scheme is formalized in Algorithm 3, whose convergence properties are characterized in Proposition 2. Note that each UE can compute its covariance shaping vector without any information exchange with the other UE provided that the channel statistics of the latter are known: in fact, in this case, the entire alternating optimization procedure can be implemented locally and independently at each UE.

Proposition 2. *The alternating optimization algorithm described in Algorithm 3 converges to a stationary point of Problem 1.*

Proof. Observe that the objective function in (4.28) does not depend on the scaling of $\mathbf{v}_k$

and, if we relax the nonconvex constraint $\|\mathbf{v}_k\|^2 = 1$ as $\|\mathbf{v}_k\|^2 \leq 1$, (4.35) remains a solution of (4.28). Then, according to [97, Corollary 2], every limit point of the sequence generated by the alternating optimization algorithm applied to problem (1) with the relaxed constraints is a stationary point of the original problem. □

Algorithm 1 can be implemented in a centralized manner at the BS and the covariance shaping vectors are fed back to the corresponding UEs. Alternatively, it can be implemented in a distributed fashion at the UEs. In this case, each UE can compute its covariance shaping vector without any information exchange with the other UE provided that the channel statistics of the latter are known, the order of update is fixed, and the same initial points are used.[1] In fact, under these conditions, the entire alternating optimization procedure can be carried out locally and independently at each UE. Note that the same considerations hold for Algorithm 2 presented in the next section.

The result of the covariance shaping optimization heavily depends on the physical scattering environment. Consider the scenario in Fig. 4.2(a) where there is no LoS path between the BS and the UEs. In this case, as shown in Fig. 4.2(b), the covariance shaping vectors tend to focus their power along reflected paths that are as orthogonal as possible to each other while also carrying sufficient channel power, which results in a nearly interference-free transmission/reception. On the other hand, when a LoS path exists, as in the scenario in Fig. 4.3(a), this generally carries more channel power than any other path. In this case, as shown in Fig. 4.3(b), the propagation directions selected by the covariance shaping vectors tend to partially capture the LoS path while also focusing some of their power along separated reflected paths in order to achieve some degree of statistical orthogonality. Remarkably, in both Fig. 4.2(b) and Fig. 4.3(b), the result of Algorithm 3 is very close to the optimal solution of Problem 1 obtained via exhaustive search, where the former is characterized by negligible complexity with respect to the latter.

Kronecker Channel Model. Let us consider the particular case where each channel $\mathbf{H}_k$ is modeled using the Kronecker channel model [98]. In this setting, we have $\mathbf{H}_k = \mathbf{R}_k^{\frac{1}{2}} \mathbf{H}_k^{(\mathrm{w})} \mathbf{T}_k^{\frac{1}{2}}$, with $\mathbf{R}_k$ and $\mathbf{T}_k$ defined in Chapter 2 and $\mathrm{vec}\big(\mathbf{H}_k^{(\mathrm{w})}\big) \sim \mathscr{CN}(\mathbf{0}, \mathbf{I}_{NM})$. Accordingly, the channel covariance matrix in Eq. (2.7) can be expressed as $\mathbf{\Sigma}_k = \mathbf{T}_k^{\mathrm{T}} \otimes \mathbf{R}_k$ with block elements given by $\mathbf{\Sigma}_{k,mn} = T_{k,mn}^* \mathbf{R}_k$, where $T_{k,mn}$ denotes the (m,n)th element of $\mathbf{T}_k$. Hence, from Eq. (4.20), we

[1] Note that $\mathbf{v}_k^{(0)}$ and $\mathbf{v}_j^{(0)}$ can be any predefined pair of normalized vectors provided by the BS

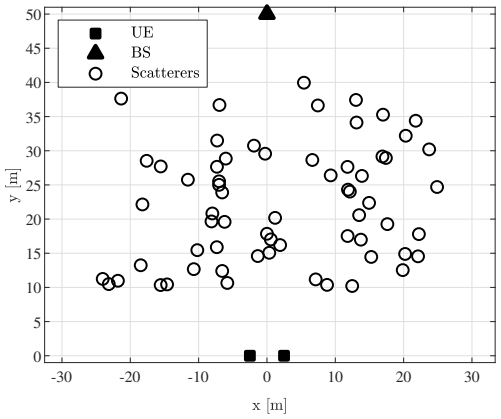

(a) NLoS scenario with $K = 2$.

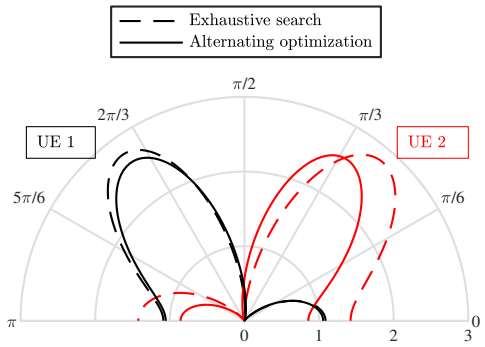

(b) Corresponding covariance shaping vectors.

Figure 4.2 – Map of the considered NLoS scenario with $K = 2$ and $N = 2$ (left) and corresponding covariance shaping vectors obtained via exhaustive search and via Algorithm 3.

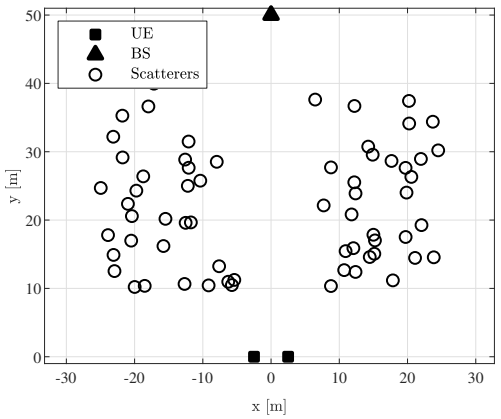

(a) LoS scenario with $K = 2$.

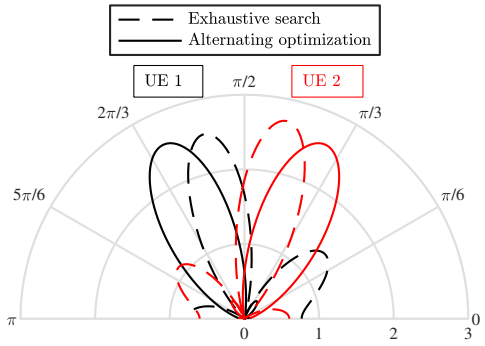

(b) Corresponding covariance shaping vectors.

Figure 4.3 – Map of the considered LoS scenario with $K = 2$ and $N = 2$ (left) and corresponding covariance shaping vectors obtained via exhaustive search and via Algorithm 3.

have

$$\delta(\mathbf{v}_k, \mathbf{v}_j) = \frac{\mathrm{tr}\left((\mathbf{v}_k^{\mathrm{H}} \boldsymbol{\Sigma}_{k,mn} \mathbf{v}_k)_{m,n=1}^{M} (\mathbf{v}_j^{\mathrm{H}} \boldsymbol{\Sigma}_{j,mn}^{\mathrm{H}} \mathbf{v}_j)_{m,n=1}^{M}\right)}{\mathrm{tr}\left((\mathbf{v}_k^{\mathrm{H}} \boldsymbol{\Sigma}_{k,mn} \mathbf{v}_k)_{m,n=1}^{M}\right) \mathrm{tr}\left((\mathbf{v}_j^{\mathrm{H}} \boldsymbol{\Sigma}_{j,mn}^{\mathrm{H}} \mathbf{v}_j)_{m,n=1}^{M}\right)} \tag{4.29}$$

$$= \frac{\mathrm{tr}\left((T_{k,mn} \mathbf{v}_k^{\mathrm{H}} \mathbf{R}_k \mathbf{v}_k)_{m,n=1}^{M} (T_{j,mn} \mathbf{v}_j^{\mathrm{H}} \mathbf{R}_j \mathbf{v}_j)_{m,n=1}^{M}\right)}{\mathrm{tr}\left((T_{k,mn} \mathbf{v}_k^{\mathrm{H}} \mathbf{R}_k \mathbf{v}_k)_{m,n=1}^{M}\right) \mathrm{tr}\left((T_{j,mn} \mathbf{v}_j^{\mathrm{H}} \mathbf{R}_j \mathbf{v}_j)_{m,n=1}^{M}\right)} \tag{4.30}$$

$$= \frac{\mathrm{tr}(\mathbf{T}_k \mathbf{T}_j)}{\mathrm{tr}(\mathbf{T}_k)\mathrm{tr}(\mathbf{T}_j)}. \tag{4.31}$$

It is straightforward to observe that, in this case, $\delta(\mathbf{v}_k, \mathbf{v}_j)$ is independent of $\mathbf{v}_k$ and $\mathbf{v}_j$. Hence, under the Kronecker channel model, it is not possible to alter the channel statistics perceived

at one end of the communication link by acting at the other end: as a consequence, no meaningful effective channel separation can be performed. This is in accordance with the properties of the Kronecker channel model, whereby the transmit and receive covariance matrices are independent. In this context, the signal subspace separation is exclusively determined by the scattering environment and can only be achieved when $\mathrm{tr}(\mathbf{T}_k\mathbf{T}_j) = 0$, which is rarely satisfied in practice [27, 98].

4.2.2 Multi-UE case

In the general case (i.e., $K \geq 2$), the covariance shaping vectors for each set of UEs sharing the same pilot $\mathbf{p}_p$ are computed by solving the optimization problem

Problem 2 (P2_CS)**.**

$$\min_{\{\mathbf{v}_k\}_{k\in\mathscr{S}_p}} \sum_{\substack{k,j\in\mathscr{S}_p \\ k\neq j}} \delta(\mathbf{v}_k,\mathbf{v}_j) \tag{4.32}$$

$$\text{s.t.} \quad \{\|\mathbf{v}_k\|^2 = 1\}_{k=1}^{K} \tag{4.33}$$

with $\delta(\mathbf{v}_k,\mathbf{v}_j)$ defined in Eq. (4.20). Although Problem 2 is not jointly convex in $\{\mathbf{v}_k\}_{k\in\mathscr{S}_p}$, it can be efficiently solved via block coordinate descent, which can be interpreted as an extension of the alternating optimization approach presented in Section 4.2.1 for the two-UE case. The optimal covariance shaping vector of UE $k \in \mathscr{S}_p$ for given $\{\mathbf{v}_j\}_{j\in\mathscr{S}_p\setminus\{k\}}$ is obtained as

$$\mathbf{v}_k^\star = \underset{\mathbf{v}_k}{\mathrm{argmin}} \frac{\sum_{m,n=1}^{M} \mathbf{v}_k^{\mathrm{H}}\big(\big(\sum_{j\in\mathscr{S}_p\setminus\{k\}} \eta_{j,mn}(\mathbf{v}_j)\big)\boldsymbol{\Sigma}_{k,mn}\big)\mathbf{v}_k}{\mathbf{v}_k^{\mathrm{H}}\big(\sum_{m=1}^{M}\boldsymbol{\Sigma}_{k,mm}\big)\mathbf{v}_k} \tag{4.34}$$

with $\eta_{j,mn}(\mathbf{v}_j)$ defined in Eq. (4.26). Like Eq. (4.27), Eq. (4.34) is in the form of generalized Rayleigh quotient and thus admits the solution

$$\mathbf{v}_k^\star = \mathbf{u}_{\min}\left(\left(\sum_{m=1}^{M}\boldsymbol{\Sigma}_{k,mm}\right)^{-1}\left(\sum_{m,n=1}^{M}\sum_{j\in\mathscr{S}_p\setminus\{k\}}\eta_{j,mn}(\mathbf{v}_j)\boldsymbol{\Sigma}_{k,mn}\right)\right) \tag{4.35}$$

and the optimal covariance shaping vectors of the other UEs $j \in \mathscr{S}_p$ for given $\{\mathbf{v}_k\}_{k\in\mathscr{S}_p\setminus\{j\}}$ are obtained in a similar way. Hence, Problem 2 is solved by computing the best response of each UE given the strategies of the other UEs until a predetermined convergence criterion is satisfied. Furthermore, at each iteration n, the update $\mathbf{v}_k^{(n)} = \bar{\alpha}\,\mathbf{v}_k^\star + (1-\bar{\alpha})\mathbf{v}_k^{(n-1)}$ can be used to limit the variation of the covariance shaping vectors between consecutive iterations, where the step size $\bar{\alpha} \in (0,1]$ must be chosen to strike the proper balance between convergence speed and accuracy (see, e.g., [99, 100]). The proposed scheme is formalized in Algorithm 2, whose convergence properties are characterized in the Proposition 3.

Algorithm 2 Covariance shaping: Block coordinate descent algorithm

Initialize $\{\mathbf{v}_k^{(0)}\}_{k\in\mathscr{S}_p}$, $\bar{\alpha}\in(0,1]$ and ξ.
$n \leftarrow 1$
while $\sum_{\substack{k,j\in\mathscr{S}_p \\ k\neq j}} \left|\left(\delta(\mathbf{v}_k^{(n)},\mathbf{v}_j^{(n)}) - \delta(\mathbf{v}_k^{(n-1)},\mathbf{v}_j^{(n-1)})\right)\right| / \delta(\mathbf{v}_k^{(n)},\mathbf{v}_j^{(n)}) > \xi$ **do**
    for $k = 1,\ldots,K$ **do**
        Given $\{\mathbf{v}_j^{(n-1)}\}_{j\in\mathscr{S}_p\setminus\{k\}}$, compute $\{\eta_{j,mn}(\mathbf{v}_j^{(n-1)})\}_{m,n=1}^{M}$ as in Eq. (4.26), $\forall\, j\in\mathscr{S}_p\setminus\{k\}$.
        Compute $\mathbf{v}_k^{\star}$ as in Eq. (4.35).
        Update $\mathbf{v}_k^{(n)} \leftarrow \bar{\alpha}\,\mathbf{v}_k^{\star} + (1-\bar{\alpha})\mathbf{v}_k^{(n-1)}$.
    end for
    Compute $\delta(\mathbf{v}_k^{(n)},\mathbf{v}_j^{(n)})$, $\forall k,j\in\mathscr{S}_p,\ k\neq j$ as in Eq. (4.20).
end while
for $k = 1,\ldots,K$ **do**
    Fix $\mathbf{v}_k = \mathbf{v}_k^{(n)}$.
end for

Proposition 3. *The block coordinate descent algorithm described in Algorithm 2 converges to a limit point of Problem 2.*

Proof. At each iteration n of Algorithm 2, the covariance shaping vector of UE k results from solving Eq. (4.27), which admits the optimal solution in Eq. (4.28). Hence, the sequence $\{\delta(\mathbf{v}_k^{(n)},\mathbf{v}_j^{(n)})\}_n$ is non-increasing since

$$\delta(\mathbf{v}_k^{(n)},\mathbf{v}_j^{(n-1)}) \leq \delta(\mathbf{v}_k^{(n-1)},\mathbf{v}_j^{(n-1)}). \tag{4.36}$$

Moreover, since $\delta(\mathbf{v}_k,\mathbf{v}_j)\geq 0$, the sequence $\{\delta(\mathbf{v}_k^{(n)},\mathbf{v}_j^{(n)})\}_n$ converges to a finite non-negative value. □

4.3 Numerical Results and Discussion

In this section we present numerical results to highlight the advantages of the proposed covariance shaping method at the UE-side. We examine the following alternative transmission schemes in order to highlight the advantages brought by suitably shaping the channel statistics:

1. **RZF+covariance shaping.** Each UE k applies its corresponding covariance shaping vector $\mathbf{v}_k$ both the uplink pilot-aided channel estimation phase and the downlink data transmission phase as discussed in Section 4.2. The BS obtains the MMSE estimates of the effective channels $\{\hat{\tilde{\mathbf{g}}}_k\}_k$ as in (4.4) based on the reception of $\bar{P} < K$ orthogonal pilot vectors. These estimates are used to compute regularized zero-forcing (RZF) precoding

at the BS as [101]

$$\mathbf{W} = P \frac{\left(\hat{\bar{\mathbf{G}}}^{\mathrm{H}}\hat{\bar{\mathbf{G}}} + \sigma_n^2 K \mathbf{I}_M\right)^{-1}\hat{\bar{\mathbf{G}}}^{\mathrm{H}}}{\left\|\left(\hat{\bar{\mathbf{G}}}^{\mathrm{H}}\hat{\bar{\mathbf{G}}} + \sigma_n^2 K \mathbf{I}_M\right)^{-1}\hat{\bar{\mathbf{G}}}^{\mathrm{H}}\right\|} \in \mathbb{C}^{M\times K} \tag{4.37}$$

where $\hat{\bar{\mathbf{G}}} = [\hat{\bar{\mathbf{g}}}_1^{\mathrm{T}}, \ldots, \hat{\bar{\mathbf{g}}}_K^{\mathrm{T}}]^{\mathrm{T}} \in \mathbb{C}^{K\times M}$.

2. **Iterative MMSE+MMSE** The BS obtains the MMSE estimates of the channel matrices $\{\mathbf{H}_k\}_k$ as in (2.9) based on the reception of $\bar{P} < K$ orthogonal pilot matrices. These estimates are used to compute MMSE precoding at the BS and MMSE combining at the UEs via the iterative algorithm proposed in [102].

3. **BD+MMSE** he BS obtains the MMSE estimates of the channel matrices $\{\mathbf{H}_k\}_k$ as in (2.9) based on the reception of $\bar{P} < K$ orthogonal pilot matrices. These estimates are used to compute block diagonalization (BD) precoding at the BS with water-filling (WF) power allocation as in [103]. On the other hand, each UE k Adopts MMSE combining defined as

$$\mathbf{V}_k = \frac{\left(\hat{\mathbf{H}}_k\mathbf{W}_k\mathbf{W}_k^{\mathrm{H}}\hat{\mathbf{H}}_k^{\mathrm{H}} + \mathbf{R}_{\tilde{Z}\tilde{Z}}\right)^{-1}\hat{\mathbf{H}}_k\mathbf{W}_k}{\left\|\left(\hat{\mathbf{H}}_k\mathbf{W}_k\mathbf{W}_k^{\mathrm{H}}\hat{\mathbf{H}}_k^{\mathrm{H}} + \mathbf{R}_{\tilde{Z}\tilde{Z}}\right)^{-1}\hat{\mathbf{H}}_k\mathbf{W}_k\right\|} \in \mathbb{C}^{N\times K} \tag{4.38}$$

where $\mathbf{R}_{\tilde{Z}\tilde{Z}} \triangleq \sum_{j\neq k}\hat{\mathbf{H}}_k\mathbf{W}_j\mathbf{W}_j^{\mathrm{H}}\hat{\mathbf{H}}_k^{\mathrm{H}} + \sigma_n^2\mathbf{I}_N \in \mathbb{C}^{N\times N}$.

Note that the schemes in 2) and 3) imply that the UEs have the same knowledge of the estimated instantaneous channels as the BS as well as perfect knowledge of the instantaneous precoding strategy used by the BS, both of which are necessary to implement MMSE combining. Note that such information must be acquired by each UE in each coherence block via extra feedback resources. On the other hand, the proposed covariance shaping approach relies solely on statistical CSI, i.e., slowly varying information, which substantially reduces the need for extra feedback resources. Furthermore, the schemes in 2) and 3) require antenna-specific pilots for the estimation of the channel matrices $\{\mathbf{H}_k\}_k$. In particular, N orthogonal pilot vectors are assigned to each UE, which implies $\tau > N\bar{P}$. On the other hand, the estimation of the effective channels $\{\bar{\mathbf{g}}_k\}_k$ resulting from covariance shaping requires $\tau > \bar{P}$ and, therefore, the pilot length can be potentially reduced. Lastly, the schemes in 2) and 3) allow the transmission of up to N streams per UE, while only one stream per UE is transmitted when covariance shaping is used. In the following, we demonstrate how the proposed covariance shaping method can effectively outperform the reference schemes, which employ the multiple antennas at the UE for spatial multiplexing, in scenarios where the UEs exhibit high spatial correlation.

We consider a scenario in which the BS is equipped with $M = 128$ antennas and wants to serve K closely spaced UEs each equipped with $N = 3$ antennas. The channel between the BS and

each UE k denoted as $\mathbf{H}_k$ follows the discrete physical channel model as in Eq. (2.4).

In the following we compare the performance in terms of sum rate and channel estimation accuracy of the considered schemes by averaging out over 5000 Monte Carlo simulations where we fix the noise power to $\sigma_n^2 = -80$ dBm. Unless otherwise stated, we use the simulation parameters listed in Table 4.1.

Table 4.1 – Covariance shaping: Simulation parameters

Parameter	Value	Parameter	Value	Parameter	Value	Parameter	Value
M	128	K	$\{2,4\}$	N	$\{2,3\}$	σ_n^2	-80 dBm
P	30 dBm	$\bar{P}$	$\lceil \frac{K}{2} \rceil$	τ	16	$K^r_{H_k}$	2.5 (LoS), 0 (NLoS)
ρ_k	25 dBm	α	2	β	4	$\tilde{\alpha}$	0.8

4.3.1 Two-UE case

We firstly examine the simple two-UEs setting in order to better highlight the key characteristics of the proposed covariance shaping approach. We analyze two different scenarios corresponding to a NLoS scenario in which the direct link between the UEs and the BS is obstructed in addition to scattered paths and a LoS scenario in which such direct link is not obstructed. The considered NLoS scenario is depicted in Fig. 4.2(a) whereas Fig. 4.2(b) shows the corresponding antenna diagram of the covariance shaping vectors obtained via Algorithm 3 and by solving Problem 1 via exhaustive search. In a similar way, Fig. 4.3(a) and Fig. 4.3(b) show the considered LoS scenario and associated covariance shaping vectors.

Fig. 4.4 shows the NMSE of each UE where we have assumed for simplicity that each UE transmits the pilots with power $\rho_1 = \rho_2 = \bar{\rho}$ in the NLoS case for the proposed BD and MMSE precoding scenarios, which is defined in Eq. (2.11), and for the covariance shaping and random beamforming methods as

$$\overline{\mathrm{NMSE}}_k^{(\mathrm{CS})} \triangleq \mathbb{E}\left[\frac{\|\hat{\tilde{\mathbf{g}}}_k - \tilde{\mathbf{g}}_k\|^2}{\|\tilde{\mathbf{g}}_k\|^2}\right]. \tag{4.39}$$

The proposed covariance shaping approach guarantees almost perfect channel estimation when the transmit power is sufficiently high thanks to statistical orthogonality, while the reference scenarios are severely limited by pilot contamination. Fig. 4.5 plots the average sum rate against the transmit power at the BS. Here, it is straightforward to see that the signal subspace separation enforced by covariance shaping during both the uplink pilot-aided channel estimation phase and the downlink data transmission phase has a highly beneficial effect on the system performance.

As a means to measure the difference between the covariance matrices of the two UEs we use

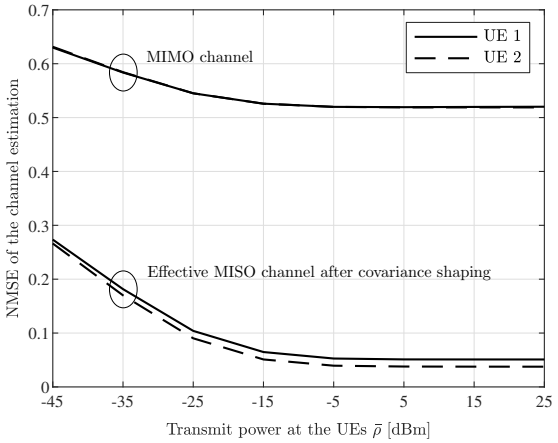

Figure 4.4 – NMSE of the channel estimation versus transmit power at the UEs for the NLoS scenario depicted in Figure 4.2a, with $K = 2$ and $N = 2$.

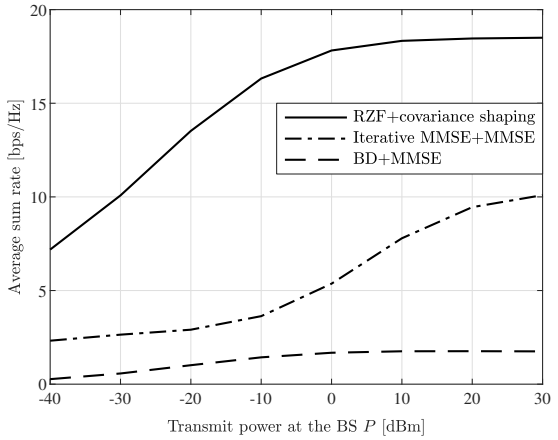

Figure 4.5 – Average sum rate versus the transmit power P at the BS for the NLoS scenario depicted in Figure 4.2a, with $K = 2$ and $N = 2$.

the notion of *chordal distance* defined as [17]

$$d_c \triangleq \|\overline{\mathbf{U}}_k \overline{\mathbf{U}}_k^{\mathrm{H}} - \overline{\mathbf{U}}_j \overline{\mathbf{U}}_j^{\mathrm{H}}\|_{\mathrm{F}}^2 \tag{4.40}$$

where $\overline{\mathbf{U}}_k$ and $\overline{\mathbf{U}}_j$ contain the eigenvectors of the covariance matrices of UEs k and j, respectively. In Fig. 4.6 we evaluate the sum rate obtained with the considered schemes in the LoS scenario against the chordal distance between the covariance matrices of the two UEs as they move away from each other. Note that at the origin of the plot the two UEs are co-located and hence have the same covariance matrix. The reference scenarios are more affected by the similarity in the channel statistics of the UEs, giving poor performance when the covariance matrices are identical. Whereas the covariance shaping method is more resilient since it guarantees sufficient statistical orthogonality.

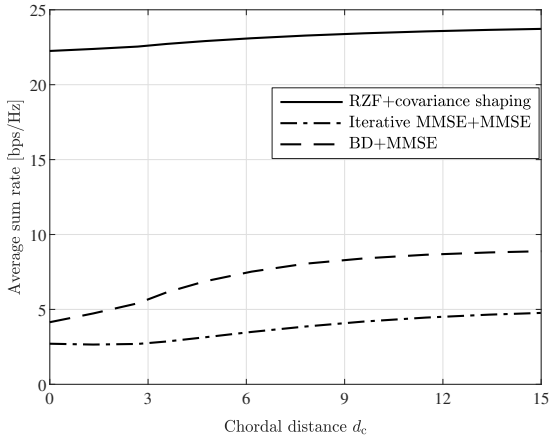

Figure 4.6 – Average sum rate versus chordal distance in the LoS scenario depicted in Figure 4.3a, with $K = 2$ and $N = 2$.

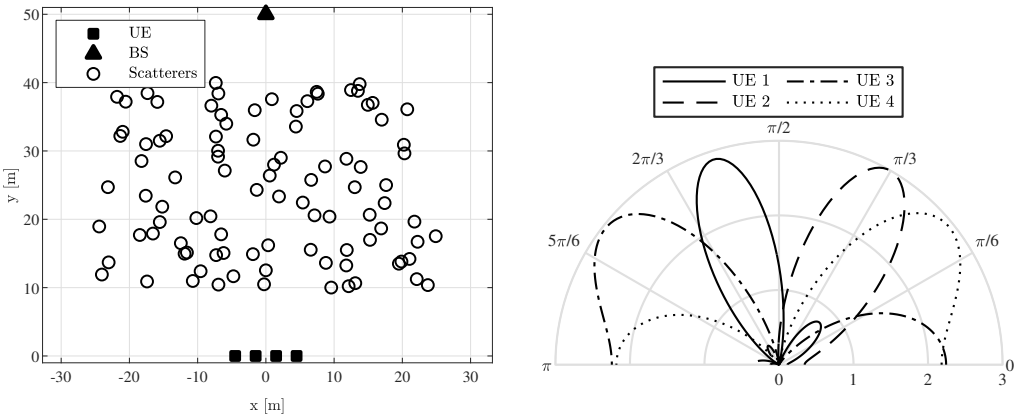

(a) NLoS scenario with $K = 4$.

(b) Corresponding covariance shaping vectors.

Figure 4.7 – Map of the considered NLoS scenario with $K = 4$ and $N = 3$ (left) and corresponding covariance shaping vectors obtained via Algorithm 4 (right).

4.3.2 Multi-UE case

In this section we set $K = 4$ unless otherwise stated and we assume a NLoS scenario, which is depicted in Fig. 4.7(a) where a set of scatterers lie between the UEs and the BS. The antenna diagram of the covariance shaping vectors obtained with Algorithm 4 is shown in Fig. 4.7(b).

Fig. 4.8 shows the average sum rate for the reference and covariance shaping scenarios against the transmit power P at the BS. The reference scenarios are severely interference limited and the corresponding sum rate quickly saturates as the transmit power increases. This is true for both the BD and MMSE precoding despite the availability of multiple degrees of freedom at the UE-side, which allow spatial multiplexing. On the contrary, covariance shaping remarkably achieves much higher performance in terms of sum rate by transmitting only one stream per UE. Moreover, random statistical beamforming does not produce significant gains meaning

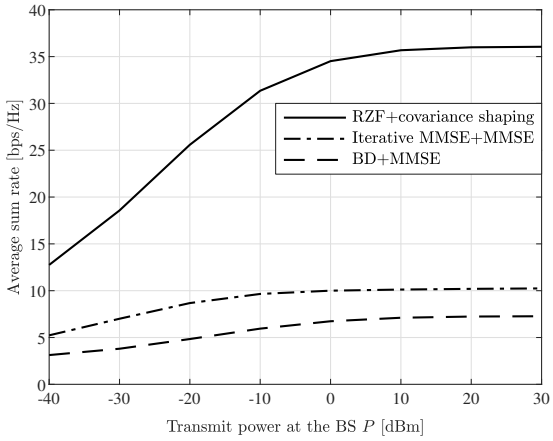

Figure 4.8 – Average sum rate versus the transmit power P at the BS for the NLoS scenario depicted in Figure 4.7a, with $K = 4$ and $N = 3$.

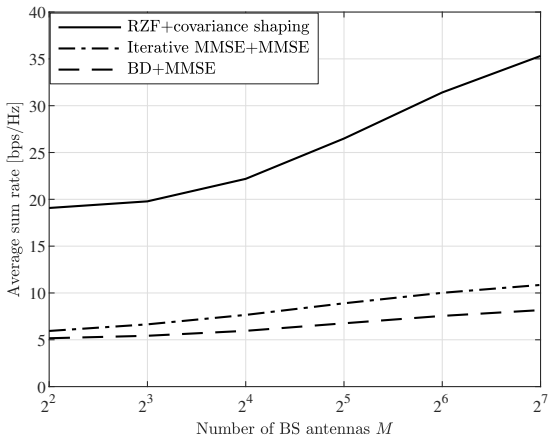

Figure 4.9 – Average sum rate versus the number of BS antennas M for the NLoS scenario depicted in Figure 4.7a, with $K = 4$ and $N = 3$.

that the proposed metric is effective in enforcing statistical orthogonality.

Fig. 4.9 shows the benefits of adding more BS antennas in terms of resulting sum rate for all the considered schemes. Moreover, it demonstrates that an increased number of spatial degrees of freedom does not fundamentally solve the limitations of the reference scenarios, where the performance is still severely limited by interference.

Lastly, Fig. 4.10 compares the sum rate obtained with the considered schemes versus the number of UEs K. The reference scenarios obtain better performance only for a single UE, since they exploit spatial multiplexing. Whereas when $K \geq 2$, the proposed covariance shaping approach guarantees significant performance gains by enforcing statistical orthogonality and despite sacrificing the available degrees of freedom.

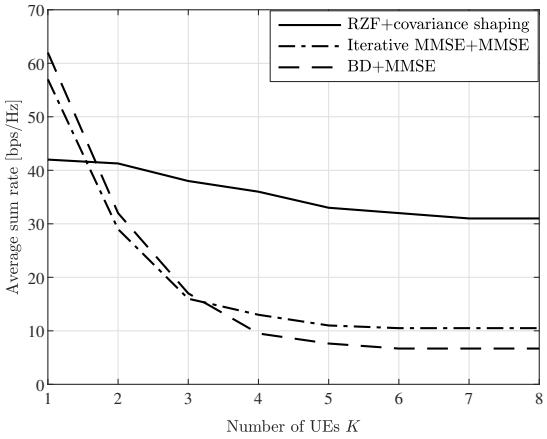

Figure 4.10 – Average sum rate versus the number of UEs K for the NLoS scenario depicted in Figure 4.7a, with $K = 4$ and $N = 3$.

4.4 Conclusions

In this part, we introduced the concept of covariance shaping, i.e., a novel method that ensures statistical favorable propagation among interfering UEs. This is done by applying a statistical beamformer at the UE-side, which is obtained by a simple iterative algorithm with proven convergence targeting the minimization of the inter-UE interference variance. Such a beamforming strategy effectively shapes the second order-statistics of the channel and is used both for pilot decontamination and downlink data transmission. Numerical results show that, despite sacrificing some of the available degrees of freedom, the proposed method is effective in partial or full statistical orthogonality among neighboring UEs and results in substantial gains in terms of system sum rate compared to conventional reference scenarios where the multiple antennas at the UE-side are used for spatial multiplexing.

Part III

D2D-Aided Multi-Antenna Multicasting

Chapter 5

Introduction

Multicasting, where a BS wishes to convey the same message to several UEs, represents a common yet highly challenging wireless scenario. In fact, guaranteeing decodability by the whole UE population proves to be a major performance bottleneck since the UEs in poor channel conditions ultimately determine the achievable rate. To overcome this issue, two-phase cooperative multicasting schemes, which use conventional multicasting in a first phase and leverage D2D communications in a second phase to effectively spread the message, have been extensively studied. However, most works are limited either to the simple case of single-antenna BS or to a specific CSIT setup.

In this part, we propose a general two-phase cooperative multicasting framework that leverages both multi-antenna transmission at the BS and D2D communications between the UEs. In particular, we highlight how endowing the BS with multiple antennas radically transforms the problem of cooperative multicasting. Indeed, the precoding capabilities at the BS introduce additional degrees of freedom for spatial selectivity that, exploited together with the D2D links, modify the nature and the performance of the two-phase schemes described in the previous section. However, this implies the joint optimization of the precoding strategy at the BS and the multicast rate, which is, at first glance, highly complex to tackle: to the best of our knowledge, this is the first work that addresses such a scenario.

We consider a general system model (in terms of both channel model and network topology) and explicitly optimize the precoding strategy at the BS and the multicast rate over the two phases. More specifically, we propose several schemes to tackle different CSIT configurations, namely: *i)* perfect CSIT, where the instantaneous channels are perfectly known; *ii)* statistical CSIT, where only the long-term channel statistics are available; and *iii)* topological CSIT, where only the map of the network area and the UE distribution are accessible. Note that statistical CSIT applies to scenarios with a large number of UEs or limited feedback in FDD mode, while topological CSIT applies to scenarios where neither instantaneous nor statistical CSIT is available and only the UE distribution across the network can be considered for

the optimization (see, e.g., [104]). In addition, following [46], we use the notion of target outage in the optimization of the multicast service, by which the multicast rate is maximized while guaranteeing decodability by most UEs up to the desired success level. In this way, we strategically avoid wasting resources on a small amount of UEs with particularly unfavorable channel conditions [105]. Numerical results show that the proposed schemes significantly outperform conventional single-phase multi-antenna multicasting in all the considered CSIT configurations. Remarkably, they allow to effectively overcome the vanishing behavior of the multicast rate and achieve an increasing performance as the UE population grows large.

The contributions of this part are summarized as follows:

- Assuming a general channel model and network topology, we propose a two-phase cooperative multicasting framework with multi-antenna transmission at the BS. We tackle the joint optimization of the precoding strategy at the BS and the multicast rate subject to some outage constraint. This framework is particularized to three different CSIT configurations, i.e., perfect, statistical, and topological CSIT. An interesting feature of our algorithms is to provide, as by-product, a selection of the UEs that are best positioned to serve as D2D relays to the remaining UEs without the need for any explicit relay selection scheme.
- For the case of perfect CSIT, we propose a low-complexity iterative algorithm that jointly selects a subset of UEs to be served by the BS in the first phase and optimizes the multicast rate while guaranteeing the desired success level. This algorithm, referred to as *D2D-MAM*, is shown to converge to a locally optimal solution.
- For the case of statistical CSIT, we propose a low-complexity algorithm that relies on long-term channel statistics without requiring costly instantaneous CSIT, which is a major advantage in scenarios with a large number of UEs or limited feedback. For this algorithm, referred to as *D2D-SMAM*, we study the scaling of the resulting multicast rate as a function of the number of UEs and BS antennas and show that this is non-vanishing in the case of dense network.
- For the case of topological CSIT, we propose an algorithm based on Monte Carlo sampling that relies uniquely on the map of the network area and the pdf of the UE locations. This approach is desirable in scenarios where neither instantaneous nor statistical CSIT is available and only the UE distribution across the network can be considered for the optimization. The proposed algorithm, referred to as *D2D-TMAM*, runs the D2D-MAM algorithm on several sets of UE locations and channels generated according to the UE distribution, and the outputs are averaged to obtain the actual precoding strategy at the BS and multicast rate.
- We present a comprehensive numerical evaluation of the proposed schemes showing

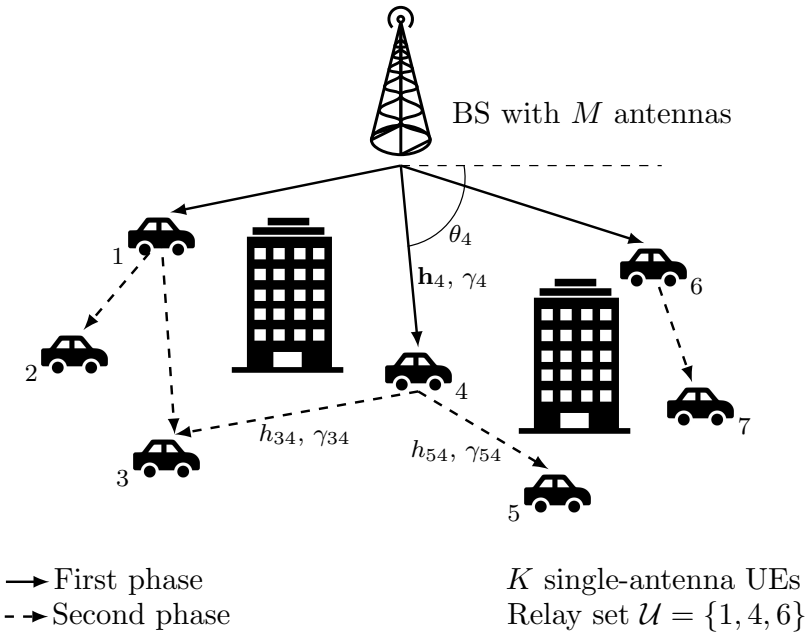

Figure 5.1 – A BS equipped with M antennas multicasts a common message to a subset of UEs with a properly designed precoding strategy in the first phase (solid lines). The UEs who successfully decode the message in the first phase retransmit it in the second phase to the remaining UEs via D2D links (dashed lines).

substantial gains compared to the reference single-phase multi-antenna multicasting in the three different CSIT configurations.

5.1 System Model

5.1.1 A two-phase protocol

We consider a special case of the wireless network described in Chapter 2 where the BS aims at transmitting a common valuable message to a set of single-antenna UEs, i.e., with $N = 1$, $\mathcal{K} \triangleq \{1, \ldots, K\}$. Hence, we let $\mathbf{h}_k \in \mathbb{C}^{M\times 1}$ denote the downlink channel between the BS and UE k. The UEs are also connected to each other via D2D links in half-duplex mode, where $h_{jk} \in \mathbb{C}$ denotes the D2D channel between UEs j and k. We adopt a dense network scenario, i.e., where the number of receivers increases over a fixed network area, and we assume that $K \gg M$. For the sake of simplicity, we follow [33, 34] and focus on a cooperative scheme divided into two phases of equal length. Such a scheme is depicted in Fig. 5.1 and the two phases are described next.

1) **First phase.** The BS transmits the message $\mathbf{x} \in \mathbb{C}^{M\times 1}$ at rate r, referred to as *multicast rate*, and with transmit covariance $\Gamma = \mathbb{E}[\mathbf{x}\mathbf{x}^{\mathrm{H}}]$ as defined in Chapter 2, with $\mathrm{tr}(\Gamma) \leq 1$. The

receive signal at UE k in the first phase is given by

$$y_{k,1} \triangleq \sqrt{\xi_0}\mathbf{h}_k^{\mathrm{H}}\mathbf{x} + n_k \in \mathbb{C} \tag{5.1}$$

where ξ_0 is the transmit power at the BS and, since we assume without loss of generality the AWGN noise term n_k to be distributed as described in Chapter 2 with $\sigma_n^2 = 1$, it can be interpreted as the transmit SNR at the BS. The message is decoded by UE k if its achievable rate in the first phase is greater than or equal to the multicast rate r, i.e., if $\log_2(1+\xi_0\mathbf{h}_k^{\mathrm{H}}\Gamma\mathbf{h}_k) \geq r$. We define the subset of UEs whose achievable rate in the first phase is at least r for a given transmit covariance as

$$\mathscr{U} \triangleq \{k \in \mathscr{K} : \log_2(1+\xi_0\mathbf{h}_k^{\mathrm{H}}\Gamma\mathbf{h}_k) \geq r\}. \tag{5.2}$$

2) **Second phase.** The UEs who were able to decode the message in the first phase jointly retransmit the message in an isotropic fashion, thus acting as opportunistic relays.[1] Hence, the receive signal at UE k in the second phase is a non-coherent sum of the D2D transmit signals and is given by

$$y_{k,2} = \sum_{j\in\mathscr{U}} \sqrt{\xi_j} h_{jk} x_j + n_k \in \mathbb{C}, \quad \forall k \in \mathscr{K}\setminus\mathscr{U} \tag{5.3}$$

where ξ_j is the transmit power at UE j and can be interpreted as the transmit SNR at UE j (cf. Eq. (5.1)); moreover, x_j is the message transmitted by UE j, with $\mathbb{E}[|x_j|^2] = 1$. The message is successfully decoded by UE k if its achievable rate in the second phase is greater than or equal to r, i.e., if $\log_2\left(1+|\sum_{j\in\mathscr{U}}\sqrt{\xi_j}h_{jk}|^2\right) \geq r$.

5.1.2 Single-phase multicasting

As a special case of the above, we describe a single-phase multicasting scheme, which we refer to as *baseline scheme*. This will serve as a means to assess the benefits brought by adding a second phase of D2D communications to traditional multi-antenna multicasting. In this scheme, the BS simply transmits the common message aiming at reaching all the UEs. The receive signal at UE k is the same as in Eq. (5.1) and the multicast capacity is given by (see [31])

$$C(\mathbf{H}) \triangleq \max_{\Gamma\succeq\mathbf{0}\,:\,\mathrm{tr}(\Gamma)\leq 1} \min_{k\in\mathscr{K}} \log_2(1+\xi_0\mathbf{h}_k^{\mathrm{H}}\Gamma\mathbf{h}_k) \tag{5.4}$$

$$= \log_2\left(1+\xi_0 \max_{\Gamma\succeq\mathbf{0}\,:\,\mathrm{tr}(\Gamma)\leq 1} \min_{k\in\mathscr{K}} \mathbf{h}_k^{\mathrm{H}}\Gamma\mathbf{h}_k\right) \tag{5.5}$$

[1] We assume that the UEs retransmit the message with fixed power and do not perform any power control in the second phase.

where $\mathbf{H} = [\mathbf{h}_1, \ldots, \mathbf{h}_K] \in \mathbb{C}^{M \times K}$. Although a closed-form expression of the multicast capacity is not available, $C(\mathbf{H})$ is convex in Γ and, therefore, it can be computed via semidefinite programming. The main drawback of this single-phase scheme is that the multicast capacity is limited by the UE with the worst channel conditions. In particular, for the case of i.i.d. Rayleigh fading channels and when the number of BS antennas M is fixed, the multicast capacity scales as $K^{-1/M}$ [31].

5.1.3 Channel model

Following the mmWave one-ring channel model (see, e.g., [106] and references therein) and simplifying the expression in Eq. (2.4), let us express the direct channel to UE k as[2]

$$\mathbf{h}_k \triangleq \eta_k \sqrt{\gamma_k} \mathbf{a}_k \in \mathbb{C}^{M \times 1} \tag{5.6}$$

where $\eta_k \sim \mathcal{CN}(0,1)$ is the small-scale fading coefficient, γ_k is the average channel power gain, and $\mathbf{a}_k \in \mathbb{C}^{M \times 1}$ is the ULA array response vector at the BS for the steering angle θ_k, with $||\mathbf{a}_k||^2 = M$ as defined in Eq. (2.1). Here, we have $\gamma_k = d_k^{-\alpha}$ in case of LoS conditions, i.e., when the Rician factor $K_{h_k} \to \infty$, and $\gamma_k = d_k^{-\beta}$ in case of NLoS conditions, i.e., when $K_{h_k} = 0$, where d_k denotes the distance between the BS and UE k and α (resp. β) is the LoS (resp. NLoS) pathloss exponent as described in Chapter 2. On the other hand, the D2D channel between UEs k and j is represented as

$$h_{jk} \triangleq \eta_{jk} \sqrt{\gamma_{jk}} \in \mathbb{C} \tag{5.7}$$

where $\eta_{kj} \sim \mathcal{CN}(0,1)$ is the small-scale fading coefficient and γ_{jk} is the average channel power gain. Here, we have $\gamma_{jk} = d_{kj}^{-\alpha}$ in case of LoS conditions and $\gamma_{jk} = d_{kj}^{-\beta}$ in case of NLoS conditions, where d_{jk} denotes the distance between UEs k and j (cf. Eq. (5.6)).

5.1.4 CSIT configurations

In this part, we consider several configurations of CSIT that may be available at the BS under different application scenarios.

i) **Perfect CSIT [Section 6.1].** The knowledge of both the direct channels, i.e., $\{\mathbf{h}_k\}_{k \in \mathcal{K}}$, and the D2D channels, i.e., $\{h_{jk}\}_{k,j \in \mathcal{K}}$, is assumed.

ii) **Statistical CSIT [Section 6.2].** The knowledge of the UE locations is assumed. From this information, the BS can extract long-term statistics such as the average channel power

[2] Note that since the UEs have one antenna, we have modified the notation given in Chapter 2 such that $\mathbf{h}_k \equiv \mathbf{H}_k$, with $\mathbf{H}_k$ defined in Eq. (2.4).

gains of both the direct channels, i.e., $\{\gamma_k\}_{k\in\mathcal{K}}$, and the D2D channels, i.e., $\{\gamma_{jk}\}_{k,j\in\mathcal{K}}$, together with the steering angles $\{\theta_k\}_{k\in\mathcal{K}}$.

iii) **Topological CSIT [Section 6.3].** The knowledge of the map of the network area, i.e., the location and size of the obstacles (such as buildings) within its coverage area, and of the pdf of the UE locations is assumed.

The above configurations correspond to settings with decreasing requirements on the information available at the BS. While configuration i) is relevant for the case of moderate (or finite) number of UEs and low mobility, configuration iii) is relevant for the case of large number of UE and high mobility: for instance, these features arise in vehicular networks, where the BS multi-antenna beam pattern ought to be designed on the basis of a city map and road traffic distribution. Lastly, configuration ii) can be considered as an intermediate case between i) and iii).

5.1.5 Performance metrics

We propose two different performance metrics in terms of service reliability. In order to reflect the inherent difficulty to *guarantee* a given data rate in a wireless setting with uncertainties on the channel conditions across the UEs, we introduce the target outage $\epsilon \in [0,1)$, which describes the trade-off between the multicast rate and the reliability level at which we can maintain such a rate. Furthermore, let $\mathrm{P}_{k,1}(r,\Gamma)$ and $\mathrm{P}_{k,2}(r,\Gamma)$ denote the probabilities that UE k successfully decodes in the first and in the second phase, respectively.

a) **Average multicast rate.** We define the *average success probability* as the probability that a randomly chosen UE successfully decodes over the two phases, which is given by

$$\mathrm{P_A}(r,\Gamma) \triangleq \frac{1}{K}\sum_{k\in\mathcal{K}}\left[\mathrm{P}_{k,1}(r,\Gamma)+\big(1-\mathrm{P}_{k,1}(r,\Gamma)\big)\mathrm{P}_{k,2}(r,\Gamma)\right]. \tag{5.8}$$

Hence, the *average multicast rate* is defined as the maximum transmission rate at which a randomly chosen UE successfully decodes with probability at least $1-\epsilon$ over the two phases, which can be expressed as

$$\mathrm{R_A}(r,\Gamma) \triangleq \frac{1}{2}r \quad \text{with } r \text{ solution to } \mathrm{P_A}(r,\Gamma) \geq 1-\epsilon. \tag{5.9}$$

b) **Outage multicast rate.** Let us introduce the binary variables $z_{k,1}(r,\Gamma)$ and $z_{k,2}(r,\Gamma)$, which are equal to 1 if UE k successfully decodes in the first and in the second phase, respectively, and to 0 otherwise. Furthermore, let $\mathbf{z}_1(r,\Gamma) \triangleq [z_{1,1}(r,\Gamma)\dots z_{K,1}(r,\Gamma)]$. We define the *joint success probability* as the probability that all the UEs successfully decode

over the two phases, which is given by

$$\mathrm{P_J}(r,\Gamma) \triangleq \mathbb{E}\left[\prod_{k\in\mathcal{K}} \mathbb{P}\left[\log_2\left(1+\left|\sum_{j\neq k}\xi_j h_{kj}\right|^2\right) \geq r\big(1-z_{k,1}(r,\Gamma)\big)\middle|\mathbf{z}_1(r,\Gamma)\right]\right]. \tag{5.10}$$

Hence, the *outage multicast rate* is defined as the maximum transmission rate at which all the UEs successfully decode with probability at least $1-\epsilon$ over the two phases, which can be expressed as

$$\mathrm{R_O}(r,\Gamma) \triangleq \frac{1}{2}r \quad \text{with } r \text{ solution to } \mathrm{P_J}(r,\Gamma) \geq 1-\epsilon. \tag{5.11}$$

5.1.6 Problem formulation

Our objective is to jointly optimize the multicast rate r and the transmit covariance Γ under one of the above outage constraints over the two phases. Such a problem can be formalized as[3]

Problem 3 (P_D2D_MAM)**.**

$$\max_{r>0,\Gamma\succeq\mathbf{0}} \quad \frac{1}{2}r \tag{5.12}$$

$$\text{s.t.} \quad \mathrm{tr}(\Gamma) \leq 1, \tag{5.13}$$

$$\mathrm{P_T}(r,\Gamma) \geq 1-\epsilon \tag{5.14}$$

where $\mathrm{T} \in \{\mathrm{A},\mathrm{J}\}$. Hence, when $\mathrm{T}=\mathrm{A}$, we recover the average multicast rate $\mathrm{R_A}(r,\Gamma)$ defined in Eq. (5.9) and, when $\mathrm{T}=\mathrm{J}$, we recover the outage multicast rate $\mathrm{R_O}(r,\Gamma)$ defined in Eq. (5.11). Note that Problem 3 is non-convex in both optimization variables due to the non-convex outage constraint and is thus highly complex to solve. In the following, we detail our proposed methods to tackle Problem 3 in the three CSIT configurations described in Section 5.1.4.

[3]The factor $\frac{1}{2}$ in the objective describes the equal time division between the two phases and is irrelevant for the optimization.

Chapter 6

D2D-Aided Multi-Antenna Multicasting: Strategies with Generalized CSIT

6.1 D2D-Aided Multi-Antenna Multicasting with Perfect CSIT

In this section, we consider the case where all the direct channels, i.e., $\{\mathbf{h}_k\}_{k\in\mathcal{K}}$, and all the D2D channels, i.e., $\{h_{jk}\}_{k,j\in\mathcal{K}}$, are perfectly known at the BS. For each UE k, let us define the binary variables

$$z_{k,1}(r,\Gamma) \triangleq \mathbb{1}\left[\log_2(1+\xi_0\mathbf{h}_k^{\mathrm{H}}\Gamma\mathbf{h}_k) \geq r\right], \tag{6.1}$$

$$z_{k,2}(r,\Gamma) \triangleq \mathbb{1}\left[\log_2\left(1+\left|\sum_{j\in\mathcal{K}\setminus\{k\}} z_{j,1}(r,\Gamma)\sqrt{\xi_j}h_{jk}\right|^2\right) \geq r\right] \tag{6.2}$$

which are equal to 1 if the UE successfully decodes in the first and in the second phase, respectively, and to 0 otherwise. Hence, the probabilities that UE k successfully decodes in the first and in the second phase are given by

$$\mathrm{P}_{k,1}(r,\Gamma) = z_{k,1}(r,\Gamma), \tag{6.3}$$

$$\mathrm{P}_{k,2}(r,\Gamma) = z_{k,2}(r,\Gamma) \tag{6.4}$$

respectively: these stem from the fact that, with perfect CSIT, the decodability of each UE in each phase is deterministic. In this context, the average success probability in Eq. (5.8) can be written as

$$\mathrm{P}_{\mathrm{A}}(r,\Gamma) = \frac{1}{K}\sum_{k\in\mathcal{K}}\left(z_{k,1}(r,\Gamma) + \big(1-z_{k,1}(r,\Gamma)\big)z_{k,2}(r,\Gamma)\right). \tag{6.5}$$

On the other hand, the joint success probability in Eq. (5.10) becomes a product of binary variables, which is equal to 0 if even a single UE does not decode the message over the two phases: hence, it is not suited to accommodate any target outage in the case of perfect CSIT. For this reason, in the rest of the section, we focus on maximizing the average multicast rate in

Eq. (5.9).

6.1.1 Multi-antenna multicasting (MAM) algorithm

Considering the single-phase baseline scheme described in Section 5.1.2, Problem 3 with T = A and perfect CSIT can be solved by selecting the best subset of $\mathcal{K}$ with size $(1-\epsilon)K$ to be served by the BS and computing the transmit covariance that maximizes the multicast rate over such a subset of UEs.[1] Note that, in this case, the outage constraint in Eq. (3) can be simply expressed as $\sum_{k\in\mathcal{K}} z_{k,1}(r,\Gamma) \geq (1-\epsilon)K$. While this problem formulation is also novel, it mainly serves as a benchmark to demonstrate the gains obtained by the adding a second phase of UE cooperation enabled by D2D links in Section 6.4. However, the problem of deriving the optimal UE selection strategy is NP-hard since it requires to evaluate all possible subsets of $\mathcal{K}$ with size $(1-\epsilon)K$. To reduce the complexity, we build on the intuition described in the following lemma to derive a suboptimal UE selection scheme.

Lemma 1. *For a class of channels satisfying* $\mathbb{E}[\mathbf{h}_k\mathbf{h}_k^{\mathrm{H}}] = \gamma_k\mathbf{I}_M$, $\forall\, k \in \mathcal{K}$, *which includes Eq.* (5.6), *the optimal UE selection strategy with statistical channel knowledge is the one choosing the* $(1-\epsilon)K$ *UEs with the highest average channel power gains among* $\{\gamma_k\}_{k\in\mathcal{K}}$.

Proof. If $\{\gamma_k > 0\}_{k\in\mathcal{K}}$ are known at the BS, we have

$$\begin{aligned}
&\max_{\mathcal{U}\subset\mathcal{K}\,:\,|\mathcal{U}|=(1-\epsilon)K} \mathbb{E}\Big[\max_{\Gamma\succeq\mathbf{0}\,:\,\mathrm{tr}(\Gamma)\leq 1} \min_{k\in\mathcal{U}} \mathbf{h}_k^{\mathrm{H}}\Gamma\mathbf{h}_k\Big] \\
&\leq \max_{\mathcal{U}\subset\mathcal{K}\,:\,|\mathcal{U}|=(1-\epsilon)K} \max_{\Gamma\succeq\mathbf{0}\,:\,\mathrm{tr}(\Gamma)\leq 1} \min_{k\in\mathcal{U}} \mathbb{E}[\mathbf{h}_k^{\mathrm{H}}\Gamma\mathbf{h}_k] &(6.6)\\
&= \max_{\mathcal{U}\subset\mathcal{K}\,:\,|\mathcal{U}|=(1-\epsilon)K} \max_{\Gamma\succeq\mathbf{0}\,:\,\mathrm{tr}(\Gamma)\leq 1} \min_{k\in\mathcal{U}} \mathrm{tr}\big(\Gamma\mathbb{E}[\mathbf{h}_k\mathbf{h}_k^{\mathrm{H}}]\big) &(6.7)\\
&= \max_{\mathcal{U}\subset\mathcal{K}\,:\,|\mathcal{U}|=(1-\epsilon)K} \min_{k\in\mathcal{U}} \gamma_k &(6.8)
\end{aligned}$$

where Eq. (6.6) follows from the concavity of $\min_{k\in\mathcal{U}} \mathbf{h}_k^{\mathrm{H}}\Gamma\mathbf{h}_k$ and Eq. (6.8) is due to the fact that the optimal Γ satisfies $\mathrm{tr}(\Gamma) = 1$. Finally, the solution presented in the lemma readily follows from Eq. (6.8). □

Lemma 1 states that, if the channels can be ordered statistically based on the average channel power gains $\{\gamma_k\}_{k\in\mathcal{K}}$, the exhaustive search over all possible subsets of $\mathcal{K}$ with size $(1-\epsilon)K$ reduces to choosing the $(1-\epsilon)K$ UEs with the highest γ_k. Motivated by this observation, we thus propose to apply such a UE selection strategy to the case of perfect CSIT and obtain the *multi-antenna multicasting (MAM) algorithm*. More specifically, we build $\mathcal{U}\subset\mathcal{K}$ by selecting the $(1-\epsilon)K$ UEs with the highest channel power gain $\|\mathbf{h}_k\|^2$ and compute the transmit

[1] Without loss of generality, one can assume that ϵ is chosen such that $(1-\epsilon)K$ is an integer number.

covariance that achieves the multicast capacity over $\mathscr{U}$, i.e.,

$$\Gamma_1 = \underset{\Gamma \succeq \mathbf{0} : \mathrm{tr}(\Gamma) \leq 1}{\operatorname{argmax}} \min_{k \in \mathscr{U}} \mathbf{h}_k^{\mathrm{H}} \Gamma \mathbf{h}_k. \tag{6.9}$$

Since the whole time resource is dedicated to the first phase, the resulting average multicast rate is given by

$$r_1 = \log_2 \left(1 + \xi_0 \min_{k \in \mathscr{U}} \mathbf{h}_k^{\mathrm{H}} \Gamma_1 \mathbf{h}_k\right). \tag{6.10}$$

6.1.2 D2D-aided multi-antenna multicasting (D2D-MAM) algorithm

To solve Problem 3 with T = A and perfect CSIT, we resort to the alternating optimization of the multicast rate r and the transmit covariance Γ. In this respect, we propose an efficient iterative algorithm whose goal is to serve a subset of UEs (which are suitably selected by means of precoding at the BS) in the first phase such that the multicast rate is maximized. At each iteration n, the transmit covariance $\Gamma^{(n)}$ that achieves the multicast capacity over a predetermined subset $\mathscr{U}^{(n-1)} \subset \mathscr{K}$ is computed (see Eq. (5.4)–(5.5)). Then, the multicast rate $r^{(n)}$ is obtained as the maximum rate that guarantees the outage constraint over the two phases given the transmit covariance computed in the previous step, i.e., such that $\mathrm{P_A}(r^{(n)}, \Gamma^{(n)}) \geq 1-\epsilon$. The new $r^{(n)}$ yields an updated $\mathscr{U}^{(n)}$ of UEs that are able to decode in the first phase and, therefore, an improved transmit covariance can be obtained by optimizing over $\mathscr{U}^{(n)}$. This procedure is iterated until the multicast rate converges. The proposed algorithm is referred to as *D2D-aided multi-antenna multicasting (D2D-MAM) algorithm* and is formally described in Algorithm 3. The D2D-MAM algorithm has the key advantage of not requiring any tuning parameter selection. Furthermore, it converges to a local optimum of Problem 3 with T = A, as formalized in the following theorem.

Theorem 1. *The D2D-MAM algorithm converges to a local optimum of Problem 3 with* T = A.

Proof. Since step 5 of Algorithm 3 optimizes $\Gamma^{(n)}$ over $\mathscr{U}^{(n-1)}$, we have

$$\min_{k \in \mathscr{U}^{(n-1)}} \mathbf{h}_k^{\mathrm{H}} \Gamma^{(n)} \mathbf{h}_k \geq \min_{k \in \mathscr{U}^{(n-1)}} \mathbf{h}_k^{\mathrm{H}} \Gamma^{(n-1)} \mathbf{h}_k \tag{6.11}$$

i.e., the minimum rate achievable by the UEs in $\mathscr{U}^{(n-1)}$ increases with the new transmit covariance $\Gamma^{(n)}$. Furthermore, at each iteration n of the D2D-MAM algorithm, the following

Algorithm 3 (D2D-MAM)

1: **Data:** Direct channels $\{\mathbf{h}_k\}_{k\in\mathcal{K}}$ and D2D channels $\{h_{jk}\}_{k,j\in\mathcal{K}}$.
2: Initialize $r^{(0)}=0$ and $r^{(1)}\neq r^{(0)}$
3: Fix $\mathcal{U}^{(0)}=\mathcal{K}$ and $n=1$.
4: **while** $r^{(n)}\neq r^{(n-1)}$ **do**
5: Optimize the transmit covariance as

$$\Gamma^{(n)}=\underset{\Gamma\succeq\mathbf{0}\,:\,\mathrm{tr}(\Gamma)\leq 1}{\operatorname{argmax}}\ \min_{k\in\mathcal{U}^{(n-1)}}\mathbf{h}_k^{\mathrm{H}}\Gamma\mathbf{h}_k.$$

6: Maximize the multicast rate as

$$r^{(n)}=\max\left\{r:\mathrm{P}_{\mathrm{A}}(r,\Gamma^{(n)})=1-\epsilon\right\}.$$

7: Update the subset of UEs successfully decoding in the first phase as

$$\mathcal{U}^{(n)}=\left\{k:\log_2(1+\xi_0\mathbf{h}_k^{\mathrm{H}}\Gamma^{(n)}\mathbf{h}_k)\geq r^{(n)}\right\}.$$

8: **end while**
9: fix $\Gamma=\Gamma^{(n)}$ and $r=r^{(n)}$.

holds:

$$\begin{aligned}r^{(n)}&\geq\log_2\left(1+\rho\min_{k\in\mathcal{U}^{(n-1)}}\mathbf{h}_k^{\mathrm{H}}\Gamma^{(n)}\mathbf{h}_k\right) &(6.12)\\ &\geq\log_2\left(1+\rho\min_{k\in\mathcal{U}^{(n-1)}}\mathbf{h}_k^{\mathrm{H}}\Gamma^{(n-1)}\mathbf{h}_k\right) &(6.13)\\ &\geq r^{(n-1)} &(6.14)\end{aligned}$$

where Eq. (6.12) follows from step 6 of Algorithm 3 (by which it is possible to increase the multicast rate as long as the outage constraint is guaranteed), Eq. (6.13) is a direct consequence of Eq. (6.11), and Eq. (6.14) stems from the fact that $\mathcal{U}^{(n-1)}$ contains the UEs whose achievable rate in the first phase is at least $r^{(n-1)}$. Hence, the multicast rate cannot decrease between consecutive iterations. Finally, if $\mathcal{U}^{(n)}=\mathcal{U}^{(n-1)}$, then it is not possible to further increase the multicast rate, i.e., $r^{(n)}=r^{(n-1)}$, which implies that convergence is reached. □

Regarding the optimization of the multicast rate in step 6 of Algorithm 3, we have

$$r^{(n)}\in\left[r^{(n-1)},\log_2\left(1+\rho\max_{k\in\mathcal{U}^{(n-1)}}\mathbf{h}_k^{\mathrm{H}}\Gamma^{(n)}\mathbf{h}_k\right)\right] \tag{6.15}$$

where the lower bound follows from Theorem 1 and the upper bound is necessary to guarantee that at least one UE is served in the first phase: thus, $r^{(n)}$ can be efficiently computed by means of bisection over the above interval. Accordingly, every iteration of the D2D-MAM algorithm requires the solution of a convex problem in step 5 and a linear search in step 6; in addition, for

the settings considered for our simulations in Section 6.4, convergence is reached after a small number of iterations. Hence, the D2D-MAM algorithm provides a locally optimal solution of Problem 3 with T = A with very low complexity.

6.2 D2D-Aided Multi-Antenna Multicasting with Statistical CSIT

In this section, we consider the case where only the UE locations are known at the BS. From this information, the BS can extract long-term statistics such as the average channel power gains of both the direct channels, i.e., $\{\gamma_k\}_{k\in\mathcal{K}}$, and the D2D channels, i.e., $\{\gamma_{jk}\}_{k,j\in\mathcal{K}}$, together with the steering angles $\{\theta_k\}_{k\in\mathcal{K}}$. On the other hand, the BS has no knowledge of the small-scale fading coefficients, i.e., $\{\eta_k\}_{k\in\mathcal{K}}$ and $\{\eta_{jk}\}_{k,j\in\mathcal{K}}$. Under statistical CSIT, we characterize the service reliability in terms of the joint success probability in Eq. (5.10) and, accordingly, we maximize the outage multicast rate in Eq. (5.11). To alleviate the task of dealing with the involved expression of the joint success probability, we derive its deterministic equivalent in the following proposition.

Proposition 4. *Assuming that all (direct and D2D) channels are independent, we have*

$$\mathrm{P_J}(r,\Gamma) \underset{K\to\infty}{\overset{\mathbb{P}}{\to}} \bar{\mathrm{P}}_\mathrm{J}(r,\Gamma) \tag{6.16}$$

where

$$\bar{\mathrm{P}}_\mathrm{J}(r,\Gamma) \triangleq \exp\Bigg(-\sum_{k\in\mathcal{K}} \frac{(2^r-1)\big(1-\mathrm{P}_{k,1}(r,\Gamma)\big)}{\sum_{j\in\mathcal{K}\setminus\{k\}} \mathrm{P}_{j,1}(r,\Gamma)\gamma_{jk}\xi_j}\Bigg) \tag{6.17}$$

is the deterministic equivalent of $\mathrm{P_J}(r,\Gamma)$ *in Eq.* (5.10).

Proof. The proof follows similar steps as the proof of [46, Thm. 4] and is thus omitted. □

Note that, with statistical CSIT, the probability that UE k successfully decodes in the first phase is given by

$$\begin{aligned}
\mathrm{P}_{k,1}(r,\Gamma) &= \mathbb{P}\big[z_{k,1}(r,\Gamma)=1\big] && (6.18)\\
&= \mathbb{P}\big[\log_2(1+\xi_0\gamma_k|\eta_k|^2\mathbf{a}_k^\mathrm{H}\Gamma\mathbf{a}_k)\geq r\big] && (6.19)\\
&= \exp\bigg(-\frac{2^r-1}{\xi_0\gamma_k\mathbf{a}_k^\mathrm{H}\Gamma\mathbf{a}_k}\bigg). && (6.20)
\end{aligned}$$

with $z_{k,1}(r,\Gamma)$ defined in Eq. (6.1) and where Eq. (6.20) follows from the exponential distribution of $|\eta_k|^2$. In the rest of the section, we replace $\mathrm{P_J}(r,\Gamma)$ with its deterministic equivalent $\bar{\mathrm{P}}_\mathrm{J}(r,\Gamma)$ in Eq. (6.17).

6.2.1 Statistical multi-antenna multicasting (SMAM) algorithm

Considering the single-phase baseline scheme described in Section 5.1.2, Problem 3 with T = J and statistical CSIT can be solved by computing the transmit covariance that maximizes the outage multicast rate. Note that, in this case, the outage constraint in Eq. (3) can be simply expressed as $\prod_{k\in\mathcal{K}} \mathrm{P}_{k,1}(r,\Gamma) \geq 1-\epsilon$. Since this problem is convex in Γ for a fixed r and vice versa, we decouple the optimization over the two variables in the following way. For a given transmit covariance Γ_1, the outage multicast rate, denoted in this context by $R_{\mathrm{O},1}(r_1,\Gamma_1)$, is maximized when the outage constraint is satisfied with equality, leading to

$$R_{\mathrm{O},1}(r_1,\Gamma_1) = \log_2\left(1+\xi_0\log\left(\frac{1}{1-\epsilon}\right)\left(\sum_{k\in\mathcal{K}}\frac{1}{\gamma_k\mathbf{a}_k^{\mathrm{H}}\Gamma_1\mathbf{a}_k}\right)^{-1}\right). \tag{6.21}$$

Then, the optimal transmit covariance is obtained by solving

Problem 4 (P_SMAM)**.**

$$\min_{\Gamma_1\succeq\mathbf{0}} \quad \sum_{k\in\mathcal{K}}\frac{1}{\gamma_k\mathbf{a}_k^{\mathrm{H}}\Gamma_1\mathbf{a}_k} \tag{6.22}$$

$$\text{s.t.} \quad \mathrm{tr}(\Gamma_1)\leq 1 \tag{6.23}$$

by means of semidefinite programming. As in Section 6.1.1, this problem formulation mainly serves for the comparative purposes in Section 6.4. The resulting algorithm is referred to as *statistical multi-antenna multicasting (SMAM) algorithm.*

The following proposition derives a tractable expression of Γ_1 and will be useful in the next section.

Proposition 5. *Assume that $\mathcal{K}$ consists of M UEs exhibiting mutually orthogonal array responses, i.e.,*

$$\sum_{k\in\mathcal{K}}\mathbf{a}_k\mathbf{a}_k^{\mathrm{H}} = M\mathbf{I}_M. \tag{6.24}$$

Then, the optimal transmit covariance for Problem 4 can be written in closed form as

$$\Gamma_1 = \frac{1}{M\nu_{\mathcal{K}}}\sum_{k\in\mathcal{K}}\frac{1}{\sqrt{\gamma_k}}\mathbf{a}_k\mathbf{a}_k^{\mathrm{H}} \tag{6.25}$$

with $\nu_{\mathcal{K}} \triangleq \sum_{k\in\mathcal{K}}\frac{1}{\sqrt{\gamma_k}}$.

Proof. See Appendix B. □

A set of array response vectors satisfying Eq. (6.24) can be obtained as the columns of the

M-dimensional discrete Fourier transform (DFT) matrix or, alternatively, it can be constructed along specific virtual angles as described in [92].

6.2.2 D2D-aided statistical multi-antenna multicasting (D2D-SMAM) algorithm

To solve Problem 3 with T = J and statistical CSIT, we use the deterministic equivalent derived in Proposition 4 and, to further reduce the complexity, we decouple the optimization across the two phases in the following way. First, we carefully select a subset $\mathscr{U} \subset \mathscr{K}$ of UEs with favorable statistical properties to be served in the first phase by the BS. In particular, assuming large K and uniform UE distribution in the angular domain, we build on Proposition 5 and construct $\mathscr{U}$ by selecting M UEs satisfying the condition in Eq. (6.24):[2] by doing so, the BS spreads its transmit power along a set of orthogonal directions spanning the whole angular domain. In this setting, the transmit covariance that maximizes the multicast rate over $\mathscr{U}$ is given by Γ_1 in Eq. (6.25). Next, we fix the joint success probability in the first phase over $\mathscr{U}$ to a given value $1-\epsilon_1$ and obtain the corresponding multicast rate $r(\epsilon_1)$ from Eq. (6.21). Finally, we optimize ϵ_1 in order to obtain the desired joint success probability $1-\epsilon$ over the two phases.

Let us first focus on maximizing the outage multicast rate over $\mathscr{U}$ in the first phase, i.e.,

Problem 5 (P_F1)**.**

$$\max_{r(\epsilon_1)>0,\Gamma\succeq\mathbf{0}} \quad r(\epsilon_1) \tag{6.26}$$

$$\text{s.t.} \quad \mathrm{tr}(\Gamma) \leq 1, \tag{6.27}$$

$$\exp\left(-\sum_{k\in\mathscr{U}} \frac{2^{r(\epsilon_1)}-1}{\xi_0 \gamma_k \mathbf{a}_k^{\mathrm{H}} \Gamma \mathbf{a}_k}\right) \geq 1-\epsilon_1. \tag{6.28}$$

Since the outage constraint is convex in Γ, we can solve Problem 5 by decoupling the optimization of $r(\epsilon_1)$ and Γ. Letting the outage constraint be satisfied with equality, we have that the multicast rate becomes

$$r(\epsilon_1) = \log_2\left(1+\xi_0 \log\left(\frac{1}{1-\epsilon_1}\right)\left(\sum_{k\in\mathscr{U}} \frac{1}{\gamma_k \mathbf{a}_k^{\mathrm{H}} \Gamma \mathbf{a}_k}\right)^{-1}\right) \tag{6.29}$$

and Problem 5 reduces to finding the transmit covariance Γ by solving

Problem 6 (P_Gamma_F1)**.**

$$\min_{\Gamma\succeq\mathbf{0}} \quad \sum_{k\in\mathscr{U}} \frac{1}{\gamma_k \mathbf{a}_k^{\mathrm{H}} \Gamma \mathbf{a}_k} \tag{6.30}$$

$$\text{s.t.} \quad \mathrm{tr}(\Gamma) \leq 1. \tag{6.31}$$

[2] Since K is large, we assume that it is always possible to select M UEs whose steering angles satisfy Eq. (6.32).

Algorithm 4 (D2D-SMAM)

1: **Data:** Build $\mathscr{U}$ by selecting M UEs such that Eq. (6.32) holds.
2: Compute the transmit covariance as in Eq. (6.33) with weights given in Eq. (6.34).
3: Find ϵ_1 by solving Eq. (6.36).
4: Compute the multicast rate as in Eq. (6.35).

From Proposition 5, the transmit covariance resulting from the above problem is known to have a simple closed-form expression when $|\mathscr{U}| = M$ and the UEs in $\mathscr{U}$ exhibit orthogonal array response vectors, i.e.,

$$\sum_{k\in\mathscr{U}} \mathbf{a}_k \mathbf{a}_k^{\mathrm{H}} = M\mathbf{I}_M. \tag{6.32}$$

Since K is large, we assume that it is always possible to build $\mathscr{U}$ by selecting M UEs satisfying the condition in Eq. (6.32). In this case, the optimal transmit covariance is given by

$$\Gamma = \sum_{j\in\mathscr{U}} w_j \mathbf{a}_j \mathbf{a}_j^{\mathrm{H}} \tag{6.33}$$

with weights given by

$$w_j \triangleq \frac{1}{M\bar{\gamma}_{\mathscr{U}}} \frac{1}{\sqrt{\gamma_j}} \quad \forall\, j \in \mathscr{U} \tag{6.34}$$

and where we have defined $\bar{\gamma}_{\mathscr{U}} \triangleq \sum_{k\in\mathscr{U}} \frac{1}{\sqrt{\gamma_k}}$. Finally, plugging Eq. (6.33) and Eq. (6.34) into Eq. (6.29), we obtain

$$r(\epsilon_1) = \log_2\left(1 + \xi_0 \log\left(\frac{1}{1-\epsilon_1}\right)\frac{M}{\bar{\gamma_{\mathscr{U}}}^2}\right). \tag{6.35}$$

Let us now focus on deriving ϵ_1 that achieves the desired joint success probability $1-\epsilon$ over the two phases. This can be done by solving the following expression for $\epsilon_1 \in [0,1)$ (e.g., by means of bisection):

$$(2^{r(\epsilon_1)}-1) \sum_{k\in\mathscr{K}} \frac{1-\exp\left(-\frac{2^{r(\epsilon_1)}-1}{\xi_0\gamma_k \mathbf{a}_k^{\mathrm{H}}\Gamma\mathbf{a}_k}\right)}{\sum_{j\in\mathscr{K}\setminus\{k\}} \exp\left(-\frac{2^{r(\epsilon_1)}-1}{\xi_0\gamma_k \mathbf{a}_k^{\mathrm{H}}\Gamma\mathbf{a}_k}\right)\gamma_{jk}\xi_j} \leq \log\left(\frac{1}{1-\epsilon}\right). \tag{6.36}$$

The proposed algorithm is referred to as *D2D-aided statistical multi-antenna multicasting (D2D-SMAM) algorithm* and is formally described in Algorithm 4. In the next section, we illustrate a possible way to derive an approximation of the optimal ϵ_1.

6.2.3 Asymptotic behavior of the D2D-SMAM algorithm

Let us assume that $\epsilon \to 0$ and, consequently, that $\epsilon_1 \to 0$. By applying the Taylor approximation $\exp\left(-\frac{2^{r(\epsilon_1)-1}}{\xi_0 \gamma_k \mathbf{a}_k^{\mathrm{H}} \Gamma \mathbf{a}_k}\right) \approx 1 - \frac{2^{r(\epsilon_1)-1}}{\xi_0 \gamma_k \mathbf{a}_k^{\mathrm{H}} \Gamma \mathbf{a}_k}$ to Eq. (6.36), we have

$$\epsilon_1 \underset{\epsilon \to 0}{\sim} 1 - \exp\left(- \frac{\bar{\gamma}_{\mathscr{U}}^2}{M \xi_0} \sqrt{\frac{\log\left(\frac{1}{1-\epsilon}\right)}{\sum_{k \in \mathscr{K}} \frac{1}{\xi_0 \gamma_k \mathbf{a}_k^{\mathrm{H}} \Gamma \mathbf{a}_k} \left(\sum_{j \in \mathscr{K} \setminus \{k\}} \gamma_{jk} \xi_j \right)^{-1}}} \right) \tag{6.37}$$

and, hence

$$r \underset{\epsilon \to 0}{\sim} \frac{1}{2} \log_2 \left(1 + \sqrt{\frac{\xi_0 \log\left(\frac{1}{1-\epsilon}\right)}{\sum_{k \in \mathscr{K}} \frac{1}{\gamma_k \mathbf{a}_k^{\mathrm{H}} \Gamma \mathbf{a}_k} \left(\sum_{j \in \mathscr{K} \setminus \{k\}} \gamma_{jk} \xi_j \right)^{-1}}} \right) \tag{6.38}$$

$$\triangleq \tilde{r}. \tag{6.39}$$

Now, assume that $d_k \in [R_{\min}, R_{\max}]$, $\forall k \in \mathscr{K}$, where $R_{\min}$ and $R_{\max}$ denote the minimum and maximum distance, respectively, between each UE and the BS. It follows that the average channel power gains can be bounded as

$$\gamma_k \in [R_{\max}^{-\beta}, R_{\min}^{-\alpha}], \qquad \forall k \in \mathscr{K}, \tag{6.40}$$

$$\gamma_{jk} \in \left[(2R_{\max})^{-\beta}, (2R_{\min})^{-\alpha} \right], \quad \forall k, j \in \mathscr{K}. \tag{6.41}$$

In this setting, we have

$$\mathbf{a}_k^{\mathrm{H}} \Gamma \mathbf{a}_k = \frac{1}{M \bar{\gamma}_{\mathscr{U}}} \sum_{j \in \mathscr{U}} \frac{1}{\sqrt{\gamma_j}} |\mathbf{a}_k^{\mathrm{H}} \mathbf{a}_j|^2 \tag{6.42}$$

$$\geq \frac{M}{\bar{\gamma}_{\mathscr{U}}} R_{\min}^{\alpha/2} \tag{6.43}$$

where Eq. (6.43) follows from assuming that all the UEs in $\mathscr{U}$ are at distance $R_{\min}$ from the BS, i.e., $\{\gamma_j = R_{\min}^{-\alpha}\}_{j \in \mathscr{U}}$. Hence, we have that $\tilde{r}$ defined in Eq. (6.38)–(6.39) can be lower bounded as

$$\tilde{r} \geq \log_2 \left(1 + \sqrt{\frac{\xi_0 \xi_{\mathrm{UE}} (K-1) M \log\left(\frac{1}{1-\epsilon}\right) R_{\min}^{\alpha/2}}{\bar{\gamma}_{\mathscr{U}}^2 (2R_{\max})^{\beta} R_{\min}^{\alpha/2} + 2^{\beta} \bar{\gamma}_{\mathscr{U}} R_{\max}^{2\beta} (K-M)}} \right) \tag{6.44}$$

where, for simplicity, we have assumed that $\{\xi_k = \xi_{\mathrm{UE}}\}_{k \in \mathscr{K}}$ (i.e., all the UEs have the same transmit SNR in the second phase). Finally, we consider the asymptotic behavior of $\tilde{r}$ in the case where both K and M increase with fixed ratio $c \triangleq \frac{K}{M} > 1$ as well as in the case where K

increases for a fixed M. Hence, Eq. (6.44) behaves as

$$\tilde{r} \underset{K\to\infty}{\rightarrow} \begin{cases} \log_2\left(1+\sqrt{\frac{\xi_0\xi_{\mathrm{UE}} M \log\left(\frac{1}{1-\epsilon}\right) R_{\min}^{\alpha/2}}{2^{\beta}\bar{\gamma}_{\mathscr{U}} R_{\max}^{2\beta}}}\right) & \text{for fixed } M \\ \log_2\left(1+\sqrt{\frac{\xi_0\xi_{\mathrm{UE}} \log\left(\frac{1}{1-\epsilon}\right) R_{\min}^{\alpha/2}}{2^{\beta}\bar{\gamma}_{\mathscr{U}} R_{\max}^{2\beta}(c-1)} K}\right) & \text{for } M=\frac{K}{c}, \text{ with } c>1 \end{cases} \tag{6.45}$$

which is non-vanishing in the first case as in [46] and increasing as $\log_2\left(1+\sqrt{K}\right)$ in the second case.

6.3 D2D-Aided Multi-Antenna Multicasting with Topological CSIT

In this section, we consider the case where only the map of the network area, i.e., the location and size of the obstacles (such as buildings) within its coverage area, and the pdf of the UE locations are known at the BS. Such pdf can be obtained on the basis of the city map and long-term information on the traffic distribution. This setting describes a scenario with a high density of UEs (e.g, cars or terminals) where it may not be feasible to design a precoding solution that adapts instantaneously to the channels or, in the longer term, to the channel statistics. In this case, it is meaningful to derive the precoding strategy at the BS based solely on the network topology and on the UE distribution.

First, we slightly adapt the channel model described in Section 3.1.1 to express all the parameters as functions of the possible UE locations within the map. Let $\mathscr{A} \subset \mathbb{R}^2$ denote the continuous set of points representing the network area and let $\mathbf{p} = (\theta, \rho)$ be a random variable denoting a possible position within $\mathscr{A}$ in which a UE can be located, where θ and ρ represent the steering angle and the distance from the BS, respectively. In this setting, we use $f(\mathbf{p})$ to denote the pdf of the UE locations, which describes the probability of finding a UE in the position identified by $\mathbf{p}$. Focusing on the first phase, let us write the direct channel to position $\mathbf{p}$ as (cf. Eq. (5.6))

$$\mathbf{h}(\mathbf{p}) = \eta\sqrt{\gamma(\mathbf{p})}\,\mathbf{a}(\theta) \tag{6.46}$$

where $\eta \sim \mathscr{CN}(0,1)$ is the small-scale fading coefficient, $\gamma(\mathbf{p})$ is the average channel power gain at position $\mathbf{p}$, and $\mathbf{a}(\theta)$ is the array response vector at the BS for the steering angle θ. Here, we have $\gamma(\mathbf{p}) = \rho^{-\alpha}$ in case of LoS conditions and $\gamma(\mathbf{p}) = \rho^{-\beta}$ in case of NLoS conditions. The receive SNR at position $\mathbf{p}$ in the first phase can be expressed as

$$\mathrm{SNR}_1(\mathbf{p}, \Gamma) \triangleq |\eta|^2 \gamma(\mathbf{p}) \xi_0 \mathbf{a}^{\mathrm{H}}(\theta) \Gamma \mathbf{a}(\theta). \tag{6.47}$$

Note that, if position $\mathbf{p}$ falls within the area occupied by an obstacle (e.g., a building), the corresponding receive SNR is zero. Hence, the probability that a UE located at position $\mathbf{p}$

successfully decodes in the first phase is given by

$$\mathrm{P}_1(\mathbf{p}, r, \Gamma) \triangleq \mathbb{P}\big[\log_2\big(1+\mathrm{SNR}_1(\mathbf{p}, \Gamma)\big) \geq r\big] \tag{6.48}$$

$$= \exp\bigg(-\frac{(2^r-1)}{\gamma(\mathbf{p})\xi_0 \mathbf{a}^{\mathrm{H}}(\theta)\Gamma\mathbf{a}(\theta)}\bigg). \tag{6.49}$$

Focusing on the second phase, let us write the D2D channel between positions $\mathbf{p}$ and $\mathbf{p}'$ as (cf. (5.7))

$$h(\mathbf{p}, \mathbf{p}') = \eta\sqrt{\gamma(\mathbf{p}, \mathbf{p}')} \tag{6.50}$$

where $\gamma(\mathbf{p}, \mathbf{p}')$ is the average channel power gain. Here, we have $\gamma(\mathbf{p}, \mathbf{p}') = d(\mathbf{p}, \mathbf{p}')^{-\alpha}$ in case of LoS conditions and $\gamma(\mathbf{p}, \mathbf{p}') = d(\mathbf{p}, \mathbf{p}')^{-\beta}$ in case of NLoS conditions, where $d(\mathbf{p}, \mathbf{p}')$ denotes the distance between positions $\mathbf{p}$ and $\mathbf{p}'$. For simplicity, let us assume that all the UEs in any position within $\mathscr{A}$ have the same transmit SNR ξ_{UE} in the second phase. Furthermore, let $\mathscr{U} \subset \mathscr{A}$ be the subset of positions where a potential UE could successfully decode in the first phase. Hence, the probability that a UE located at position $\mathbf{p}$ successfully decodes the message in the second phase is given by

$$\mathrm{P}_2(\mathbf{p}, r, \Gamma) \triangleq \mathbb{P}\left[\log_2\left(1+\left|\int_{\mathscr{U}} \sqrt{\xi_{\mathrm{UE}}} f(\mathbf{p}') h(\mathbf{p}, \mathbf{p}') \mathrm{d}\mathbf{p}'\right|^2\right) \geq r\right] \tag{6.51}$$

$$= \mathbb{E}\left[\exp\left(-\frac{2^r-1}{\xi_{\mathrm{UE}}\int_{\mathscr{U}} f(\mathbf{p}')\gamma(\mathbf{p}, \mathbf{p}\prime)\mathrm{d}\mathbf{p}'}\right)\right] \tag{6.52}$$

where the expectation is over all the possible combinations of $\mathscr{U}$.

In the context of topological CSIT, the average success probability in Eq. (5.8) can be written as

$$\mathrm{P}_{\mathrm{A}}(r, \Gamma) = \int_{\mathscr{A}} f(\mathbf{p})\big(\mathrm{P}_1(\mathbf{p}, r, \Gamma) + (1-\mathrm{P}_1(\mathbf{p}, r, \Gamma))\mathrm{P}_2(\mathbf{p}, r, \Gamma)\big)\mathrm{d}\mathbf{p}. \tag{6.53}$$

On the other hand, the joint success probability in Eq. (5.10) turns out to be impractical when $\mathscr{A}$ is connected, i.e., when the network area contains infinite points. For this reason, in the rest of the section, we focus on maximizing the average multicast rate in Eq. (5.9). Since Eq. (6.53) is quite difficult to handle even for simple UE distribution models (e.g., uniform), in the next section, we detail a heuristic approach to maximize the average multicast rate based on the Monte Carlo sampling of $f(\mathbf{p})$.

Algorithm 5 (D2D-TMAM)

1: **Data:** Map of the network area and pdf of the UE locations $f(\mathbf{p})$.
2: Fix $b = 1$.
3: **for** $b = 1, \ldots, B$ **do**
4: Generate T test points together with the corresponding direct and D2D channels according to Eq. (6.46) and Eq. (6.50), respectively.
5: Execute Algorithm 3 with the channels generated in step 4 as input data and obtain the multicast rate $r^{(b)}$ and the transmit covariance $\Gamma^{(b)}$ as output data.
6: **end for**
7: Fix $r = \frac{1}{B}\sum_{b=1}^{B} r^{(b)}$ and $\Gamma = \frac{1}{B}\sum_{b=1}^{B} \Gamma^{(b)}$.

6.3.1 D2D-aided topological multi-antenna multicasting (D2D-TMAM) algorithm

To solve Problem 3 with T = A and topological CSIT, we resort to the Monte Carlo sampling of the pdf of the UE locations to generate a set of test points within the map and the corresponding artificial channels, which are subsequently used to run the D2D-MAM algorithm described in Algorithm 3 (see Section 6.1.2). More specifically, we produce B batches of T test points each, where T is a random variable that describes the number of UEs and whose distribution depends on $f(\mathbf{p})$. For each batch b, we artificially generate the direct channels for each test point according to Eq. (6.46) as well as the D2D channels for each pair of test points according to Eq. (6.50). Then, such channels are used as input data to Algorithm 3, which produces the multicast rate $r^{(b)}$ and the transmit covariance $\Gamma^{(b)}$ as output data. Finally, the final multicast rate and transmit covariance are obtained by averaging the output data of the B batches, i.e., $r = \frac{1}{B}\sum_{b=1}^{B} r^{(b)}$ and $\Gamma = \frac{1}{B}\sum_{b=1}^{B} \Gamma^{(b)}$, which provides an approximate solutions to Problem 3 with T = A. The proposed algorithm is referred to as *D2D-aided topological multi-antenna multicasting (D2D-TMAM) algorithm* and is formally described in Algorithm 5. Evidently, evaluating more batches of test points allows to achieve a more precise representation of the long-term network statistics, which produces a more accurate result in terms of average success probability. Since the D2D-TMAM algorithm involves B instances of Algorithm 3, its computational complexity may be quite high. However, it is worth observing that this procedure is based on slowly varying network statistics and needs to be updated only when the UE distribution changes significantly. Therefore, it can be conveniently executed offline using a large value of B.

6.4 Numerical Results

In this section, we present numerical results to validate the proposed algorithms in the three different CSIT configurations, i.e., perfect CSIT (described in Section 6.1), imperfect CSIT (described in Section 6.2), and topological CSIT (described in Section 6.3). Unless otherwise stated, the considered network topology consists of a semicircular area with radius $R_{\max}$ =

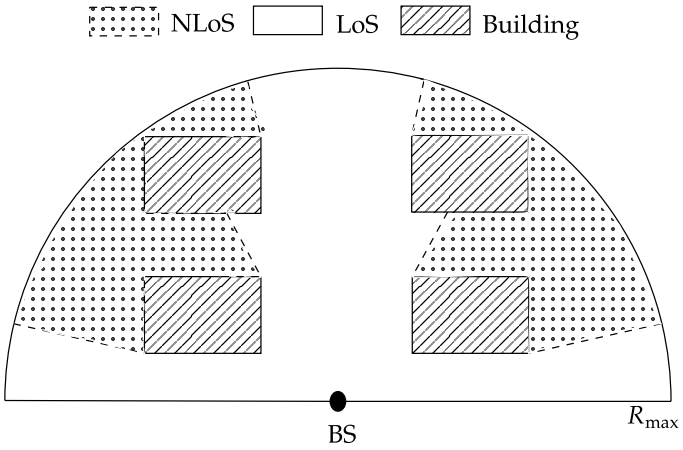

Figure 6.1 – Evaluation scenario: the white area and the dotted areas are in LoS and NLoS conditions, respectively, whereas the UEs are not admitted in the regions occupied by the buildings.

100 m where four rectangular buildings are positioned in a Manhattan-like grid, as shown in Fig. 6.1. We assume that the UEs are distributed uniformly within the network area with the exception of the regions occupied by the buildings and with a minimum distance from the BS of $R_{\min} = 5$ m. The direct and D2D links whose line of sight is obstructed by one or more buildings are considered to be in NLoS conditions both in the first and in the second phase. The LoS and NLoS pathloss exponents are fixed to $\alpha = 2$ and $\beta = 4$, respectively. For simplicity, we assume that all the UEs have the same transmit SNR in the second phase, i.e., $\{\xi_k = \xi_{\text{UE}}\}_{k \in \mathcal{K}}$, and we set $\xi_0 = 30$ dB and $\xi_{\text{UE}} = 20$ dB. Moreover, unless otherwise stated, the BS is equipped with $M = 32$ antennas and the target outage is fixed to $\epsilon = 0.1$. Lastly, all the numerical results are averaged over 5×10^3 independent UE drops.

6.4.1 Perfect CSIT

In the case of perfect CSIT, we evaluate the performance of the proposed D2D-MAM algorithm in Algorithm 3 versus the single-phase MAM algorithm described in Section 6.1.1. Interestingly, the D2D-MAM algorithm converges in very few iterations (typically between 3 and 10) even for large values of K. Fig. 6.2(a) plots the average multicast rate against the number of UEs for different values of ϵ. Indeed, the second phase of D2D communications brings substantial gains with respect to traditional multi-antenna multicasting. In particular, the average multicast rate obtained with the D2D-MAM algorithm increases with K, whereas that resulting from the MAM algorithm quickly vanishes. Hence, the D2D-MAM algorithm effectively overcomes the worst-UE bottleneck behavior of conventional single-phase multicasting and remarkably achieves an increasing trend of the multicast rate. In the same setting of Fig. 6.2(a), Fig. 6.2(b) shows that the average number of UEs who are able to decode in the first

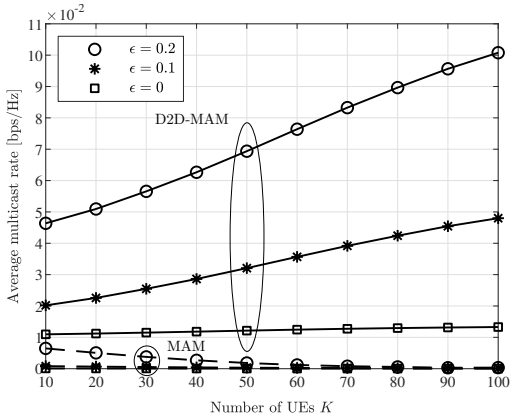

(a) Average multicast rate against the number of UEs with $M = 32$ and for different values of ϵ.

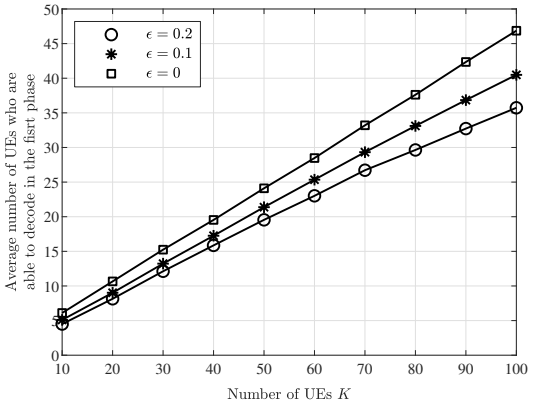

(b) Average number of UEs who are able to decode in the first phase against the number of UEs with $M = 32$ and for different values of ϵ.

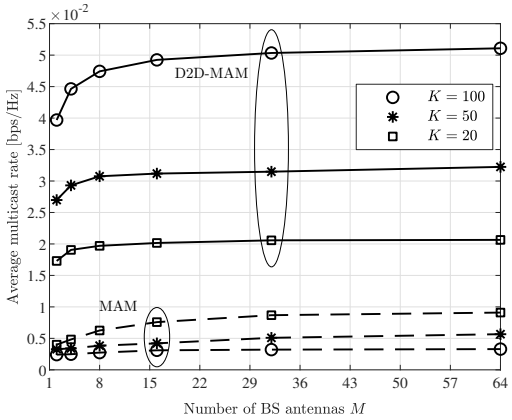

(c) Average multicast rate against the number of BS antennas with $\epsilon = 0.1$ and for different values of K.

Figure 6.2 – Perfect CSIT: D2D-MAM algorithm versus MAM algorithm.

phase varies between 35% and 50% of the total UEs depending on the target outage. Lastly, Fig. 6.2(c) illustrates the average multicast rate against the number of BS antennas for different values of K. Evidently, the BS can better focus its transmit power as M increases, which results in an overall improved performance. Here, the lowest value corresponds to $M = 1$, i.e., when the BS has no beamforming capability and can only transmit in an isotropic fashion in the first phase.

6.4.2 Statistical CSIT

In the case of statistical CSIT, we evaluate the performance of the proposed D2D-SMAM algorithm in Algorithm 4 versus the single-phase SMAM described in Section 6.2.1. In addition, we compare the asymptotic expressions obtained in Section 6.2.3 with numerical simulations.

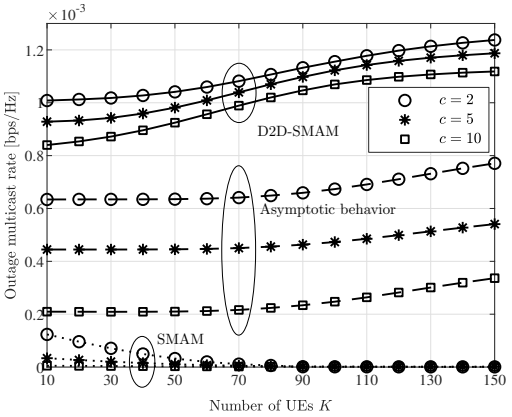

(a) Outage multicast rate against the number of UEs for different values of $c = \frac{K}{M}$.

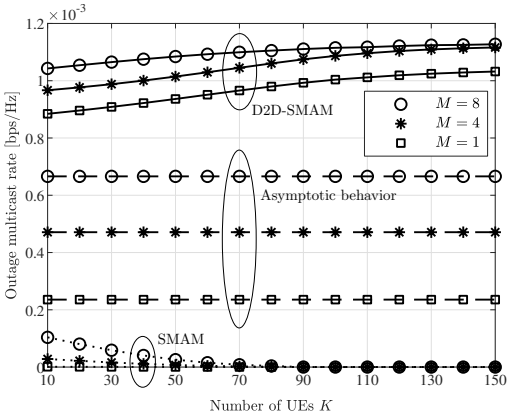

(b) Outage multicast rate against number of UEs for different values M.

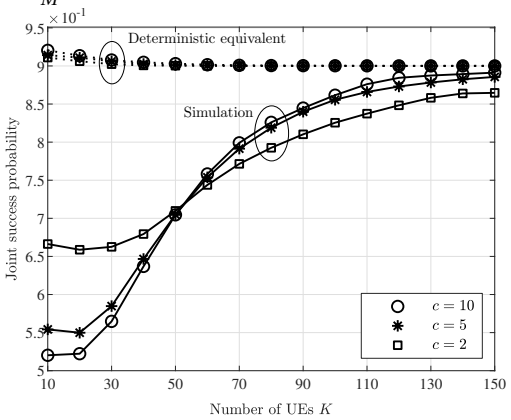

(c) Joint success probability in Eq. (5.10) and its deterministic equivalent in Eq. (6.17) for different values of $c = \frac{K}{M}$.

Figure 6.3 – Statistical CSIT: D2D-SMAM algorithm versus SMAM algorithm.

For the D2D-SMAM algorithm, we build the set $\mathcal{U}$ by identifying M UEs whose steering angles satisfy the condition in Eq. (6.24), while their distance from the BS is uniformly distributed. We consider two cases of interest, i.e., where both the number of UEs K and the number of BS antennas M increase with a fixed ratio $c = \frac{K}{M} > 1$ and where K increases for a fixed M. The first case is depicted in Fig. 6.3(a), which shows that the outage multicast rate always grows as long as M grows together with K. The second case is illustrated in Fig. 6.3(b), which shows how increasing M is always beneficial for any given number of UEs K. Here, the outage multicast rate obtained with the D2D-SMAM algorithm grows with K and reaches a constant value for large K: this is confirmed by its asymptotic behavior, which is constant with K. On the contrary, the SMAM algorithm produces a vanishing outage multicast rate and even increasing M does not fundamentally solve this issue. Lastly, Fig. 6.3(c) compares the joint success probability in Eq. (5.10) with its deterministic equivalent in Eq. (6.17) for different

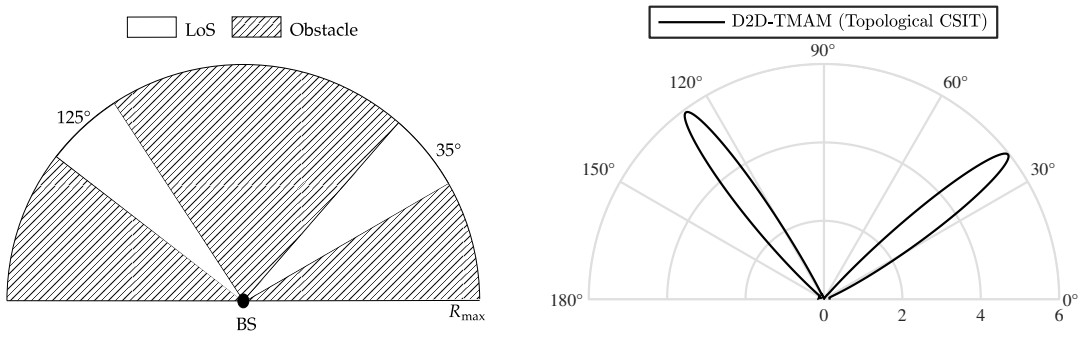

(a) Evaluation scenario.

(b) Antenna diagram of the transmit covariance with $M = 32$.

Figure 6.4 – Toy example with topological CSIT: the UEs are admitted only in the two white sectors.

values of c. Here, the approximation is tight for sufficiently large values of K.

6.4.3 Topological CSIT

In the case of topological CSIT, we evaluate the performance of the proposed D2D-TMAM algorithm in Algorithm 5 versus the D2D-MAM algorithm in Algorithm 3, where the latter is based on the assumption of perfect CSIT. Although unfair to the D2D-TMAM algorithm, this comparison demonstrates how the proposed approach with topological CSIT can accurately sample the long-term network statistics. In turn, this enables to effectively design the precoding strategy at the BS with minimal CSIT requirements and no training overhead without excessively compromising the performance. Let A denote the area of the network excluding the regions occupied by the buildings (expressed in m^2) and let us consider a uniform UE distribution with density $\bar{\lambda}$ (expressed in UEs/m^2). In this setting, we assume that each UE drop consists of K UEs, where K is a Poisson random variable with mean $\bar{K} = \bar{\lambda} A$. Recall that, for the D2D-TMAM algorithm, the transmit covariance and the multicast rate are computed offline by averaging the output of the D2D-MAM algorithm over B batches of T test points, where we fix $B = 10^3$; on the other hand, the D2D-MAM algorithm is executed for each UE drop.

- **Toy example.** As a first experiment to verify the effectiveness of the proposed method, we consider the simplified network topology depicted in Fig. 6.4(a), with $R_{\max} = 20$ m and where only two sectors admit the presence of UEs. In this setting, we have $A = 100$ m^2 and, fixing $\bar{\lambda} = 0.5$ UEs/m^2, the average number of UEs in the network is $\bar{K} = 50$; moreover, we assume that all the links are in LoS conditions. Fig. 6.4(b) shows the antenna diagram of the transmit covariance obtained with the D2D-TMAM algorithm

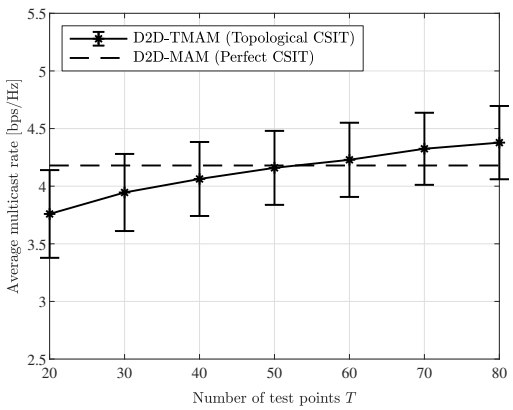

(a) Average multicast rate against number of test points with $M = 32$.

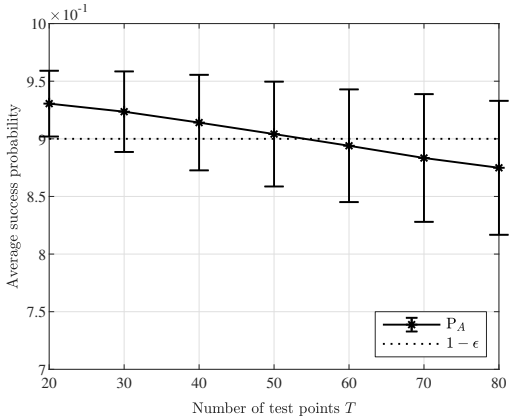

(b) Average success probability against number of test points with $M = 32$.

Figure 6.5 – Topological CSIT applied to the toy example in Fig. 6.4(a): D2D-TMAM algorithm versus D2D-MAM algorithm, where the latter relies on perfect CSIT.

with $T = \bar{K}$ test points for each batch: as expected, the multi-antenna beam pattern uniformly covers the two sectors in which the UEs are concentrated. Now, we evaluate the average multicast rate and the average success probability as T varies in order to verify which value gives the best performance. Fig. 6.5 shows that, when T is too small, the algorithm is overcautious and selects a low multicast rate corresponding to an average success probability above the target; on the other hand, when T is too large, the algorithm is overaggressive and selects a high multicast rate corresponding to an average success probability below the target. As expected, the target outage is reached for $T = \bar{K}$ and the corresponding mean value of the average multicast rate is very close to that obtained with the D2D-MAM algorithm (which relies on perfect CSIT).

Now, let us go back to the original evaluation scenario depicted in Fig. 6.1 and compare the proposed D2D-TMAM algorithm with the D2D-MAM algorithm. Fig. 6.6(a) illustrates the average multicast rate against the UE density for different values of ϵ. First of all, we observe that both schemes benefit from increasing the number of UEs, thus effectively overcoming the worst-UE bottleneck behavior of conventional single-phase multicasting. Furthermore, the performance gap between the D2D-TMAM algorithm and the D2D-MAM algorithm is remarkably small despite the huge difference in the CSIT requirements of the two schemes. Lastly, Fig. 6.6(b) plots the average success probability against the UE density for different values of ϵ, showing that the target success probability is achieved more accurately by the D2D-TMAM algorithm as the UE density increases.

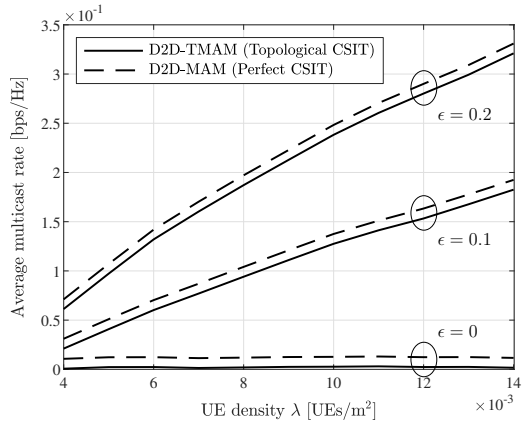

(a) Average multicast rate against UE density with $M = 32$ and for different values of ϵ.

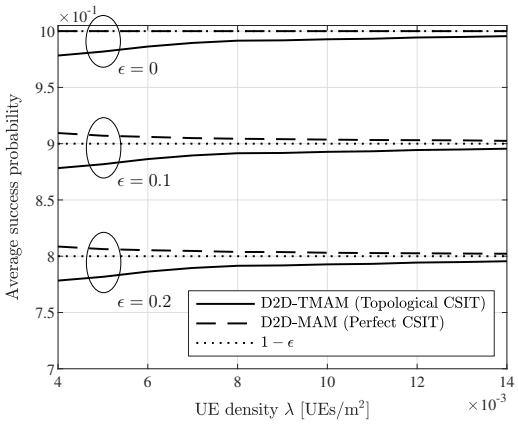

(b) Average success probability against UE density with $M = 32$ and for different values of ϵ.

Figure 6.6 – Topological CSIT applied to the evaluation scenario in Fig. 6.1: D2D-TMAM algorithm versus D2D-MAM algorithm, where the latter relies on perfect CSIT.

6.5 Conclusions

In this part we have proposed a general two-phase cooperative multicasting framework that leverages both multi-antenna transmission at the BS and D2D communications between the UEs. We explicitly optimize the precoding strategy at the BS and the multicast rate over the two phases subject to some outage constraint. In particular, we devise efficient algorithms to tackle three different CSIT configurations, i.e., perfect CSIT, statistical CSIT, and topological CSIT. Numerical results show that the proposed schemes significantly outperform conventional single-phase multi-antenna multicasting in all the considered CSIT configurations. Remarkably, they allow to effectively overcome the vanishing behavior of the multicast rate and achieve an increasing performance as the UE population grows large.

Part IV

Reconfigurable Intelligent Surfaces

Chapter 7

Introduction

Massive access for IoT in beyond-5G networks represents a daunting challenge for conventional bandwidth-limited technologies. MmWave technologies—which provide large chunks of bandwidth at the cost of more complex wireless processors in harsher radio environments—is a promising alternative to accommodate massive IoT but its cost and power requirements are an obstacle for wide adoption in practice. In this context, meta-materials arise as a key innovation enabler to address this challenge. Specifically, the so called *RISs*.

In this part, we introduce and study a beyond-5G scenario consisting of a multi-antenna BS serving a large set of single-antenna UEs with the aid of RISs to cope with NLoS paths. Specifically, we build a mathematical framework to jointly optimize the precoding strategy of the BS and the RIS parameters in order to maximize the system performance. In particular, we propose to exploit the SMSE as an optimization objective. The choice of an objective function is of paramount importance, especially for massive access scenarios. Our objective function is purposely chosen such that we can derive a mechanism that provides high-performing solutions while guaranteeing efficiency and scalability. Interestingly, such metric—which has not been studied so far in the context of RIS-aided networks—reveals a convex structure in the two optimization variables separately, namely the precoding strategy at the transmitter and the RIS parameters. This gives us an edge over prior work because it allows to design very efficient iterative algorithms for RIS control.

We present RISMA, a RIS-aided Multi-UE Alternating optimization algorithm that jointly optimizes the beamforming strategy at the BS and the RIS parameters to provide high-bandwidth low-cost connectivity in massive IoT scenarios. In marked contrast with prior work, RISMA exploits the convex nature of the problem at hand in the two optimization variables separately to ensure scalability, efficiency and provable convergence in the design without the need of setting any system parameter. Moreover, we adapt RISMA, which provides a solution from a theoretical perspective, to accommodate practical constraints when using low-resolution RISs that are comprised of antenna elements that can be activated in a binary fashion. In this way,

these are meta-surfaces that only support phase shift values from a discrete set, rather than any real value from a range, and further compound our problem [107, 108]. To address this scenario, we propose Lo-RISMA, which deals with the optimization of the binary activation coefficients and the quantized phase shits. In particular, we define a discrete set of points consisting of the discrete set of phase shift values plus the zero coefficient, to account for antenna elements who are deactivated. The resulting problem is solved via SDR. Differently than other prior work considering low-resolution RISs [83, 109], Lo-RISMA benefits from the key properties of the chosen SMSE metric. Indeed, for each iteration of the proposed algorithm for a fixed RIS configuration the precoding strategy is found via a simple closed form solution. Whereas once the precoding strategy is fixed the problem of finding the RIS parameters can be efficiently solved via SDR.

Our numerical results show that a joint optimization of both the precoder of the transmitter and the RIS parameters in terms of induced phase shifts and amplitude attenuation produce substantial gains in sum rate performance. Specifically, our joint optimization approach leads to ~40% gain compared to using only a MMSE precoder over a broad range of network area radii, and gains that scale linearly with the network-area's radius compared to a zero-forcing (ZF) precoder, e.g., ~20% and ~120% improvement for radii equal to 100 and 150 meters, respectively.

7.1 Model design

7.1.1 System model

Let us consider a special case of the scenario described in Chapter 2, which is depicted in Fig. 7.1, wherein the BS serves a set of K single-antenna UEs, i.e., with $N = 1$. However, note that the proposed method is not limited to such a case. When considering multiple-antenna UEs, our model can be readily applied by letting each UE activate the antenna with the highest average channel power gain. The connection is established with the aid of a set of RISs installed on the building glasses each of which consists of L equivalent antenna elements. Focusing on the downlink data transmission and using the definitions provided in Chapter 2, the BS communicates to each UE k via a direct link denoted by $\mathbf{h}_k \in \mathbb{C}^{M\times 1}$ which comprises of a LoS path of length d_k and angle of departure (AoD) θ_k when the latter exists, in addition to a multipath NLoS link. Additionally, the BS can exploit a combined link from the BS to the RIS denoted by $\mathbf{G} \in \mathbb{C}^{L\times M}$, which in turns reflects the incoming signal towards the UE through the channel $\mathbf{h}_k^r \in \mathbb{C}^{L\times 1}$. The latter is decomposed into the LoS BS-RIS path of length $d_{1,k}$ and with AoD from the BS and AoA at the RIS denoted by ψ_D and ψ_A, respectively plus a set of scattered NLoS paths and the RIS-UE k link which comprises of a LoS path of length $d_{2,k}$ and AoD ψ_k when available, plus a multipath NLoS link. Lastly, due to high path loss we neglect all signals

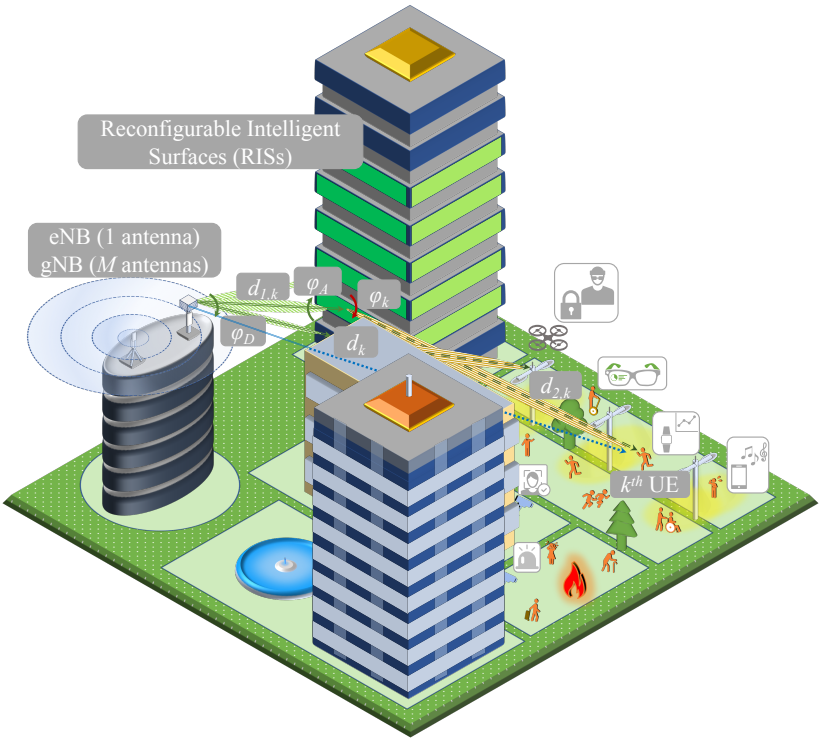

Figure 7.1 – Radio massive access scenario overcoming NLoS issues by means of RISs installed on the building glasses. It might support different use cases, such as Augmented Reality (AR)-glasses, e-health, video-surveillance, Industrial-IoT

reflected two times or more by the RIS as in [66, 79, 82].[1] We further assume that perfect CSI is available at the BS, i.e., the latter knows $\{\mathbf{h}_k\}_{k=1}^K$, $\mathbf{G}$ and $\{\mathbf{h}_k^r\}_{k=1}^K$.[2]

While we focus on the downlink data transmission, our proposed framework might be straightforwardly extended to the uplink direction considering multiple UEs and one single BS. Each UE k receives the sum of two contributions, namely a direct path from the BS and a suitably reflected path upon the RIS. Hence, the receive signal at UE k is given by Eq. (2.13) and repeated in the following for further clarity

$$y_k = \left(\left(\mathbf{h}_k^r\right)^{\mathrm{H}} \mathbf{\Phi} \mathbf{G} + \mathbf{h}_k^{\mathrm{H}}\right) \mathbf{W}\mathbf{s} + n_k \in \mathbb{C} \tag{7.1}$$

where $\mathbf{\Phi} \in \mathbb{C}^{L \times L}$ represents the phase shifts and amplitude attenuation introduced by the RIS, $\mathbf{W} \in \mathbb{C}^{M \times K}$ is the transmit precoder, $\mathbf{s} \in \mathbb{C}^{K \times 1}$ is the transmit symbol vector, and n_k is the noise term. Note that all the above quantities are defined in Chapter 2.

[1] Note that since the UEs have one antenna, we have modified the notation given in Chapter 2 such that $\mathbf{h}_k \equiv \mathbf{H}_k$, with $\mathbf{H}_k$ defined in Eq. (2.4), and $\mathbf{h}_k^r \equiv \mathbf{H}_k^r$, with $\mathbf{H}_k^r$ defined in Eq. (2.6).

[2] When dealing with biased channel information, a channel estimation process is required. However, such a challenge in RIS-aided networks has been already explored in [78, 79] and thus is out of the scope of this dissertation.

Hence, assuming single-UE decoding at the receiver side and given that the UEs have one antenna, i.e., $N = 1$, the system sum rate is given by simplifying the expression in Eq. (2.16) as

$$R = \sum_k \log_2 \left(1 + \frac{\left| \left((\mathbf{h}_k^r)^{\mathrm{H}} \boldsymbol{\Phi} \mathbf{G} + \mathbf{h}_k^{\mathrm{H}} \right) \mathbf{w}_k \right|^2}{\sum_{j \neq k} \left| \left((\mathbf{h}_k^r)^{\mathrm{H}} \boldsymbol{\Phi} \mathbf{G} + \mathbf{h}_k^{\mathrm{H}} \right) \mathbf{w}_j \right|^2 + \sigma_n^2} \right). \tag{7.2}$$

7.1.2 Problem formulation

Our objective is to optimize the overall system performance of the considered RIS-aided network in terms of the system sum rate, as defined in Eq. (7.2). In particular, given the complexity of treating such an expression, we propose to jointly optimize the precoding strategy at the BS and the reflections (as a tunable parameter) introduced by the RIS by minimizing the SMSE over all connected UEs, which is known to relate to the sum rate [102]. In particular, for a given configuration of the RIS the considered system in the downlink is a broadcast channel and duality between broadcast and uplink multiple access channel holds. In the dual multiple access channel the classical relation between MMSE of UE k and maximum SINR of UE k holds for linear filters [110]. Hence, this motivates us to study the SMSE as a means to optimize the system sum rate in the downlink.

As described in Eq. (8.4) of Chapter 2, the receive MSE of UE k is given by

$$\begin{aligned} \mathrm{MSE}_k &= \mathbb{E}[|y_k - s_k|^2] && (7.3)\\ &= \left| \left((\mathbf{h}_k^r)^{\mathrm{H}} \boldsymbol{\Phi} \mathbf{G} + \mathbf{h}_k^{\mathrm{H}} \right) \mathbf{w}_k - 1 \right|^2 + \sum_{j \neq k} \left| \left((\mathbf{h}_k^r)^{\mathrm{H}} \boldsymbol{\Phi} \mathbf{G} + \mathbf{h}_k^{\mathrm{H}} \right) \mathbf{w}_j \right|^2 + \sigma_n^2 && (7.4)\\ &= \sum_j \left| \left((\mathbf{h}_k^r)^{\mathrm{H}} \boldsymbol{\Phi} \mathbf{G} + \mathbf{h}_k^{\mathrm{H}} \right) \mathbf{w}_j \right|^2 - 2\,\mathrm{Re}\left\{ \left((\mathbf{h}_k^r)^{\mathrm{H}} \boldsymbol{\Phi} \mathbf{G} + \mathbf{h}_k^{\mathrm{H}} \right) \mathbf{w}_k \right\} + 1 + \sigma_n^2. && (7.5) \end{aligned}$$

The receive SMSE over all UEs is thus expressed as (cf. Eq. 2.19)

$$\begin{aligned} \mathrm{SMSE} &= \sum_k \mathrm{MSE}_k && (7.6)\\ &= \sum_k \sum_j \left| \left((\mathbf{h}_k^r)^{\mathrm{H}} \boldsymbol{\Phi} \mathbf{G} + \mathbf{h}_k^{\mathrm{H}} \right) \mathbf{w}_j \right|^2 - 2 \sum_k \mathrm{Re}\left\{ \left((\mathbf{h}_k^r)^{\mathrm{H}} \boldsymbol{\Phi} \mathbf{G} + \mathbf{h}_k^{\mathrm{H}} \right) \mathbf{w}_k \right\} + K(1 + \sigma_n^2). && (7.7) \end{aligned}$$

For ease of presentation, let us define

$$\boldsymbol{\theta} = [\alpha_1 e^{-j\phi_1}, \ldots, \alpha_L e^{-j\phi_L}, 1]^{\mathrm{T}} \in \mathbb{C}^{L+1 \times 1}, \tag{7.8}$$

and

$$\bar{\mathbf{H}}_k \triangleq \begin{bmatrix} \mathrm{diag}\left(\left(\mathbf{h}_k^r\right)^{\mathrm{H}}\right)\mathbf{G} \\ \mathbf{h}_k^{\mathrm{H}} \end{bmatrix} \in \mathbb{C}^{L+1\times M}, \tag{7.9}$$

such that $\boldsymbol{\Phi} = \mathrm{diag}(\boldsymbol{\theta}[1:L]^{\mathrm{H}})$ and [3]

$$\left(\left(\mathbf{h}_k^r\right)^{\mathrm{H}}\boldsymbol{\Phi}\mathbf{G} + \mathbf{h}_k^{\mathrm{H}}\right)\mathbf{w}_j = \boldsymbol{\theta}^{\mathrm{H}}\bar{\mathbf{H}}_k\mathbf{w}_j \quad \forall k, j. \tag{7.10}$$

Hence, our optimization problem can be formulated as follows

Problem 7 (P_SMSE)**.**

$$\begin{aligned} \underset{\boldsymbol{\theta},\mathbf{W}}{\text{minimize}} \quad & \sum_k \sum_j |\boldsymbol{\theta}^{\mathrm{H}}\bar{\mathbf{H}}_k\mathbf{w}_j|^2 - 2\sum_k \mathrm{Re}\{\boldsymbol{\theta}^{\mathrm{H}}\bar{\mathbf{H}}_k\mathbf{w}_k\} \\ \text{s.t.} \quad & |\theta_i|^2 \leq 1, \quad i = 1,\ldots,L; \\ & \theta_{L+1} = 1; \\ & \|\mathbf{W}\|_{\mathrm{F}}^2 \leq P; \end{aligned}$$

with $\boldsymbol{\theta}$ defined in Eq. (7.8). Note that the constraint $|\theta_i|^2 \leq 1$ ensures that the i-th RIS element does not amplify the incoming signal, thus guaranteeing a passive structure overall. We remark that contrarily to previous works on beamforming optimization in RIS-aided networks [79–84], our proposed framework has the key advantage of being convex in the two optimization variables $\boldsymbol{\theta}$ and $\mathbf{W}$ separately. *This allows us to find simple and efficient solutions to the problem at hand.* Moreover, thanks to this aforementioned key property the use of alternating optimization between the two optimization variables $\boldsymbol{\theta}$ and $\mathbf{W}$ allows us to guarantee convergence to a critical point of Problem 7, i.e., a point that satisfies the Karush-Kuhn-Tucker (KKT) conditions of Problem 7 [97, 111]. Note that given the non convex nature of Problem 7, the KKT conditions are necessary but not sufficient conditions for optimality. We now deeply examine our problem for two main use cases: *i*) single-UE receiver and *ii*) multi-UE receiver.

[3] Note that the last element of $\boldsymbol{\theta}$ is introduced to obtain a more compact expression of our optimization problems.

Chapter 8

RISMA: Reconfigurable Intelligent Surfaces Enabling Beamforming for IoT Massive Access

8.1 Single-UE Case

We firstly focus on the case of $K = 1$ to better highlight the key feature of the proposed RISMA method. In order to separately exploit the convexity in $\boldsymbol{\theta}$ and $\mathbf{W}$ of our objective function in Problem 7, let the RIS parameters in $\boldsymbol{\theta}$ be fixed such that we can firstly focus on finding the precoding strategy $\mathbf{W}$. Since perfect CSI is available at the BS, when $\boldsymbol{\theta}$ is fixed the optimal linear transmit precoding vector is known to be the one matched to the (here, effective) channel between the BS and the UE maximizing the receive SNR, which is given by MRT, i.e.,

$$\mathbf{w}_{\text{MRT}} = \sqrt{P}\frac{\mathbf{G}^{\text{H}}\boldsymbol{\Phi}^{\text{H}}\mathbf{h}^{r} + \mathbf{h}}{\|\mathbf{G}^{\text{H}}\boldsymbol{\Phi}^{\text{H}}\mathbf{h}^{r} + \mathbf{h}\|}. \tag{8.1}$$

Thus, once the precoding strategy is obtained the problem reduces to the optimization of the RIS setting parameters in $\boldsymbol{\Phi}$. Consider the receive MSE after MRT precoding

$$\text{MSE}_{\text{MRT}} = \mathbb{E}[|y - s|^2], \tag{8.2}$$

where the expectation is over the symbol s and the noise n, which are assumed to be independent. Hence, we have that

$$\text{MSE}_{\text{MRT}} = \mathbb{E}\left[\left|\left[\left(\left(\mathbf{h}^{r}\right)^{\text{H}}\boldsymbol{\Phi}\mathbf{G} + \mathbf{h}^{\text{H}}\right)\mathbf{w}_{\text{MRT}} - 1\right]s + n\right|^2\right] \tag{8.3}$$

$$= P\left\|\left(\mathbf{h}^{r}\right)^{\text{H}}\boldsymbol{\Phi}\mathbf{G} + \mathbf{h}^{\text{H}}\right\|^2 - 2\sqrt{P}\left\|\left(\mathbf{h}^{r}\right)^{\text{H}}\boldsymbol{\Phi}\mathbf{G} + \mathbf{h}^{\text{H}}\right\|^2 + 1 + \sigma_n^2. \tag{8.4}$$

We thus formulate the following optimization problem

Problem 8 (P1)**.**

$$\min_{\boldsymbol{\Phi}} \left\| \left(\mathbf{h}^r\right)^{\mathrm{H}} \boldsymbol{\Phi}\mathbf{G} + \mathbf{h}^{\mathrm{H}} \right\|^2 - 2\frac{\sqrt{P}}{P} \left\| \left(\mathbf{h}^r\right)^{\mathrm{H}} \boldsymbol{\Phi}\mathbf{G} + \mathbf{h}^{\mathrm{H}} \right\| \tag{8.5}$$

$$\text{s.t.} |[\boldsymbol{\Phi}]_{ii}|^2 \leq 1 \quad \forall i \tag{8.6}$$

$$[\boldsymbol{\Phi}]_{ij} = 0 \quad \forall i \neq j. \tag{8.7}$$

By substituting Eq. (7.8) and Eq. (7.9) into Problem (8), we recast the latter into the following

Problem 9 (P2)**.**

$$\begin{aligned} \min_{\boldsymbol{\theta}} \quad & \|\boldsymbol{\theta}^{\mathrm{H}} \bar{\mathbf{H}}\|^2 - 2\frac{\sqrt{P}}{P} \|\boldsymbol{\theta}^{\mathrm{H}} \bar{\mathbf{H}}\| \\ \text{s.t.} \quad & |\theta_i|^2 \leq 1, \quad i = 1, \ldots, L; \\ & \theta_{L+1} = 1. \end{aligned}$$

Note that Problem 9 is non-convex in $\boldsymbol{\theta}$ but it can be solved efficiently by standard convex-concave programming as it is a summation of a convex function, i.e., the squared norm term, minus a second convex function, i.e., the norm term [112].

An alternative yet simpler approach defines $\Theta = \boldsymbol{\theta}\boldsymbol{\theta}^{\mathrm{H}}$ and solve the following optimization problem

Problem 10 (P3)**.**

$$\begin{aligned} \min_{\boldsymbol{\theta}, \Theta \succeq \mathbf{0}} \quad & \mathrm{tr}(\bar{\mathbf{H}}\bar{\mathbf{H}}^{\mathrm{H}}\Theta) - 2\frac{\sqrt{P}}{P}\sqrt{\mathrm{tr}(\bar{\mathbf{H}}\bar{\mathbf{H}}^{\mathrm{H}}\Theta)} \\ \text{s.t.} \quad & [\Theta]_{ii} \leq 1, \quad i = 1, \ldots, L; \\ & [\Theta]_{L+1,L+1} = 1, \theta_{L+1} = 1; \\ & \begin{bmatrix} \Theta & \boldsymbol{\theta} \\ \boldsymbol{\theta}^{\mathrm{H}} & 1 \end{bmatrix} \succeq \mathbf{0}, \\ & \mathrm{rank}(\Theta) = 1. \end{aligned}$$

Note that Problem 10 is non-convex in Θ due to the rank constraint. However, by employing SDR the latter can be turned into a convex problem by relaxing the rank constraint. The resulting problem can be then solved via standard semidefinite programming (SDP) as, e.g., Disciplined Convex Programming (CVX). An approximate solution of Problem 10 can be obtained from the relaxed convex problem via Gaussian randomization [113]. While the optimality of Gaussian Randomization is only proven for a small well-defined family of optimization problems, it guarantees an $\frac{\pi}{4}$-approximation of the optimal objective value of the

original problem for a sufficiently large number of randomizations, as shown in [114].

Lastly, note that the RIS parameters $\{\alpha_i\}_{i=1}^L$ and $\{\phi_i\}_{i=1}^L$ can be obtained by setting

$$\alpha_i = |\theta_i|, \quad \text{and} \tag{8.8}$$

$$\phi_i = \arg(\theta_i^*), \quad i = 1, \ldots, L. \tag{8.9}$$

8.1.1 Practical systems: low-resolution RIS

In practical systems, it is difficult to control exactly the state of each reflecting element as this control is implemented through sensible variations of the equivalent impedance of each reflecting cell. It is thus not practical to allow any possible state for the absorption coefficients $\{\alpha_i\}_{i=1}^L$ and phase reflection $\{\phi_i\}_{i=1}^L$ of the i-th reflecting element [71, 75]. In this respect, we propose an extension of the method proposed in Section 8.1, dubbed as Lo-RISMA, which decouples the optimization of $\{\alpha_i\}_{i=1}^L$ and $\{\phi_i\}_{i=1}^L$ to include practical implementation constraints, namely, each reflecting element is activated in a binary fashion and each phase shift can vary on a given set of discrete values.

Binary activation.

We start by treating the binary activation assumption, namely each reflecting element can have only one of two states, i.e., $\alpha_i \in \{0,1\}\ \forall i$. Hence, we solve Problem (9) or Eq. (10) in order to obtain the values of $\{\phi\}_{i=1}^L$ as per Eq. (8.9).

In the considered single-UE scenario, the maximization of the sum rate is equivalent to the minimization of the receive MSE or the maximization of the receive SNR. Let us define the effective channel as the following

$$\widetilde{\mathbf{H}} = \begin{bmatrix} \mathrm{diag}\left(\left(\mathbf{h}^r\right)^{\mathrm{H}}\right)\bar{\mathbf{\Phi}}\mathbf{G} \\ \mathbf{h}^{\mathrm{H}} \end{bmatrix} \in \mathbb{C}^{L+1\times M}, \tag{8.10}$$

with $\bar{\mathbf{\Phi}} \triangleq \mathrm{diag}[e^{j\phi_1}, \ldots, e^{j\phi_L}]$ and the binary vector $\mathbf{b} \in \{0,1\}^{L+1}$, where each b_i indicates whether the corresponding reflecting element is active or not. Hence, we have that $\alpha_i = b_i,\ i = 1, \ldots, N$ and $\mathbf{\Phi} = \mathrm{diag}(b_1 e^{j\phi_1}, \ldots, b_L e^{j\phi_L})$. The receive SNR after MRT precoding is given by

$$\mathrm{SNR}_{\mathrm{MRT}} = \frac{\|\mathbf{b}^{\mathrm{T}}\widetilde{\mathbf{H}}\|^2}{\sigma_n^2}, \tag{8.11}$$

which is clearly maximized when $\mathbf{b} = \mathbf{1}$.

Quantized phase shifts.

Consider now the case where the phases $\{\phi_i\}_{i=1}^{L}$ are quantized with a given number of bits $\bar{b}$ as explained in [71, 83, 109, 115]. The ideal feasible set $[0, 2\pi)$ is thus quantized into $2^{\bar{b}}$ uniformly spaced discrete points as

$$\phi_i \in \mathcal{Q} \triangleq \left\{ \frac{2\pi}{2^{\bar{b}}} m \right\}_{m=0}^{2^{\bar{b}}-1} \quad m \in \mathbb{Z},\ i = 1, \ldots, L. \tag{8.12}$$

To achieve such quantization, we simply project the phase shifts obtained by solving Problem 9 or 10 onto the closest point within the constellation in $\mathcal{Q}$.

8.2 Multi-UE Case

Hereafter, we consider the multi-UE scenario described in Section 7.1. Differently than the single UE case, here the optimal transmit precoder is not know a priori and needs to be optimized. In particular, we show how the chosen optimization metric—which has not been analyzed so far in RIS-aided communication systems—yields simple expressions for both the optimized precoding strategy at the BS and the RIS parameters when employing alternating optimization between the two. Specifically, we solve the problem of jointly optimizing the precoding strategy and the RIS parameters by fixing in turn one of the two optimization variables and analyzing the resulting partial problems. It is interesting to see that such partial problems allow simple empirical closed-form solutions. The resulting algorithm provides an effective solution to the original joint optimization which can be proven to be a stationary point of the Lagrangian of the latter.

8.2.1 Alternating optimization

Let us consider Problem 7 (P_SMSE), which is not jointly convex in $\boldsymbol{\theta}$ and $\mathbf{W}$ whereas, differently than prior work, is convex in the two optimization variables, separately. We can thus solve Problem 7 efficiently via alternating optimization. If $\mathbf{W}$ is fixed, then Problem 7 (P_SMSE) reduces as follows

Problem 11 (P_SMSE_v)**.**

$$\begin{aligned} \min_{\boldsymbol{\theta}} \quad & \sum_k \|\boldsymbol{\theta}^{\mathrm{H}} \bar{\mathbf{H}}_k \mathbf{W}\|^2 - 2 \sum_k \mathrm{Re}\{\boldsymbol{\theta}^{\mathrm{H}} \bar{\mathbf{H}}_k \mathbf{w}_k\} \\ \text{s.t.} \quad & |\theta_i|^2 \leq 1 \quad i = 1, \ldots, L; \\ & \theta_{L+1} = 1. \end{aligned}$$

Problem 11 admits the following solution

$$\boldsymbol{\theta} = \left(\sum_k \bar{\mathbf{H}}_k \mathbf{W}\mathbf{W}^{\mathrm{H}} \bar{\mathbf{H}}_k^{\mathrm{H}} + \mathrm{Diag}(\boldsymbol{\mu}) \right)^{-1} \left(\sum_k \bar{\mathbf{H}}_k \mathbf{w}_k - \nu \, \mathbf{e}_{N+1} \right) \tag{8.13}$$

where $\boldsymbol{\mu} \geq \mathbf{0}$ is a vector of non-negative variables to be determined in the following way

$$\begin{aligned} &\mu_i = 0 \text{ and } |\theta_i|^2 \leq 1, \\ &\mu_i \geq 0 \text{ and } |\theta_i|^2 = 1, \quad \forall i = 1, \ldots, L. \end{aligned} \tag{8.14}$$

To alleviate the task of finding $\boldsymbol{\mu}$ in Eq. (8.14) we set $\boldsymbol{\mu} = \sigma_n^2 \mathbf{1}$ following the results in [101]. Let

$$\bar{\boldsymbol{\theta}} = \left(\sum_k \bar{\mathbf{H}}_k \mathbf{W}\mathbf{W}^{\mathrm{H}} \bar{\mathbf{H}}_k^{\mathrm{H}} + \sigma_n^2 \mathbf{I}_{L+1} \right)^{-1} \left(\sum_k \bar{\mathbf{H}}_k \mathbf{w}_k - \nu \, \mathbf{e}_{N+1} \right). \tag{8.15}$$

Hence we have that

$$\boldsymbol{\theta} = \frac{\bar{\boldsymbol{\theta}}}{\|\bar{\boldsymbol{\theta}}\|}. \tag{8.16}$$

Lastly, ν is found by letting $\theta_{L+1} = 1$ as

$$\nu = \frac{\mathbf{e}_{L+1}^{\mathrm{T}} \mathbf{B}\mathbf{r} - 1}{\mathbf{e}_{L+1}^{\mathrm{T}} \mathbf{B}\mathbf{e}_{L+1}}. \tag{8.17}$$

where

$$\mathbf{B} = \left(\sum_k \bar{\mathbf{H}}_k \mathbf{W}\mathbf{W}^{\mathrm{H}} \bar{\mathbf{H}}_k^{\mathrm{H}} + \sigma_n^2 \mathbf{I}_{L+1} \right)^{-1}, \tag{8.18}$$

and $\mathbf{r} = \sum_k \bar{\mathbf{H}}_k \mathbf{w}_k$.

Proof. The solution of Problem 11 is analytically derived in Appendix C by solving KKT conditions. □

When $\boldsymbol{\theta}$ is fixed, Problem 7(P_SMSE) reduces to the following

Problem 12 (P_SMSE_w)**.**

$$\begin{aligned} \min_{\mathbf{W}} \quad & \sum_k \|\bar{\mathbf{h}}_k^{\mathrm{H}} \mathbf{W}\|^2 - 2 \sum_k \mathrm{Re}\{\bar{\mathbf{h}}_k^{\mathrm{H}} \mathbf{W}\mathbf{e}_k\} \\ \text{s.t.} \quad & \|\mathbf{W}\|_{\mathrm{F}}^2 \leq P; \end{aligned}$$

where we define $\bar{\mathbf{h}}_k \triangleq \bar{\mathbf{H}}_k^{\mathrm{H}} \boldsymbol{\theta}$. Again, given the convexity of Problem 12, the KKT conditions are

necessary and sufficient for the solution of the problem and yield the following

$$\mathbf{W} = \left(\bar{\mathbf{H}}\bar{\mathbf{H}}^{\mathrm{H}} + \mu \mathbf{I}_M\right)^{-1}\bar{\mathbf{H}}, \tag{8.19}$$

with $\bar{\mathbf{H}} = [\bar{\mathbf{h}}_1, \ldots, \bar{\mathbf{h}}_K]$ and $\mu \geq 0$ such that $\|\mathbf{W}\|_{\mathrm{F}}^2 = P$ is satisfied[1]. Leveraging the results in [101] we set $\mu = K\sigma_n^2/P$ which is proven to maximize the UEs SINR in the limit of large K, while proving to be tight for even small values of K. Hence we obtain the following empirical closed-form expression for the precoding matrix $\mathbf{W}$

$$\mathbf{W} = \sqrt{P}\frac{\bar{\mathbf{W}}}{\|\bar{\mathbf{W}}\|_{\mathrm{F}}} \tag{8.20}$$

where $\bar{\mathbf{W}} = \left(\bar{\mathbf{H}}\bar{\mathbf{H}}^{\mathrm{H}} + \frac{K\sigma_n^2}{P}\mathbf{I}_M\right)^{-1}\bar{\mathbf{H}}$.

Proof. We derive Eq. (8.19) in Appendix D by solving the KKT conditions. □

Due to the convex nature of Problem 11 and 12, we propose an efficient algorithm, namely RISMA, which alternates the optimization of both the precoding strategy at the BS $\mathbf{W}$ and the RIS setting parameters in $\boldsymbol{\theta}$. Thanks to the convex nature of the two partial problems for which we have found an optimal solution, it can be proven that RISMA converges to a critical point of Problem 7, i.e., a point that satisfies the KKT conditions of Problem 7 ([97, 111]). The proposed algorithm is formally described in Algorithm 6 where step 5 implements Eq. (8.17).

8.2.2 Practical systems: low resolution RIS

As described in Section 8.1.1, in practical conditions it is difficult to control the state of each reflecting element perfectly. In the following, we reformulate the problem in Section 8.2.1 to cope with the limits of practical hardware implementations and we assume that each reflecting element can be activated in a binary fashion and introduces only quantized phase shifts. The proposed algorithm dubbed Lo-RISMA is formally described in Algorithm 7.

If $\mathbf{W}$ is fixed then Problem 11 (P_SMSE_v) stated in Section 8.2.1 is modified as follows

Problem 13 (P_SMSE_Lo)**.**

$$\begin{aligned} \min_{\boldsymbol{\theta}} \quad & \sum_k \|\boldsymbol{\theta}^{\mathrm{H}}\bar{\mathbf{H}}_k\mathbf{W}\|^2 - 2\sum_k \mathrm{Re}\{\boldsymbol{\theta}^{\mathrm{H}}\bar{\mathbf{H}}_k\mathbf{w}_k\} \\ \text{s.t.} \quad & \theta_i \in \bar{\mathcal{Q}} \quad i = 1, \ldots, L; \\ & \theta_{L+1} = 1, \end{aligned}$$

[1] In order to determine μ we can apply a bisection method.

Algorithm 6 RISMA: RIS-aided Multi-UE Alternating optimization

Initialize $\mathbf{W}^{(0)}$, $\text{SMSE}^{(0)}$ and ξ
$n \leftarrow 1$
while $\left|\left(\text{SMSE}^{(n)} - \text{SMSE}^{(n-1)}\right)/\text{SMSE}^{(n)}\right| > \xi$ **do**
  $\boldsymbol{\mu} = \sigma_n^2 \mathbf{1}$
  $\nu \leftarrow$ Force $\theta_{L+1}^{(n)} = 1$

$$\bar{\boldsymbol{\theta}} = \left(\sum_k \bar{\mathbf{H}}_k \mathbf{W}\mathbf{W}^{\mathrm{H}} \bar{\mathbf{H}}_k^{\mathrm{H}} + \text{Diag}(\boldsymbol{\mu})\right)^{-1} \left(\sum_k \bar{\mathbf{H}}_k \mathbf{w}_k - \nu \mathbf{e}_{L+1}\right)$$

$$\boldsymbol{\theta}^{(n)} = \frac{\bar{\boldsymbol{\theta}}}{\|\bar{\boldsymbol{\theta}}\|}$$

  $\bar{\mathbf{H}} = [\bar{\mathbf{H}}_1^{\mathrm{H}} \boldsymbol{\theta}^{(n)}, \ldots, \bar{\mathbf{H}}_K^{\mathrm{H}} \boldsymbol{\theta}^{(n)}]$

$$\mu = \frac{K\sigma_n^2}{P}$$

  $\bar{\mathbf{W}} = \left(\bar{\mathbf{H}}\bar{\mathbf{H}}^{\mathrm{H}} + \mu \mathbf{I}_M\right)^{-1} \bar{\mathbf{H}}$

$$\mathbf{W}^{(n)} = \sqrt{P} \frac{\bar{\mathbf{W}}}{\|\bar{\mathbf{W}}\|_{\mathrm{F}}}$$

$$\text{SMSE}^{(n)} = \sum_k \sum_j |(\boldsymbol{\theta}^{(n)})^{\mathrm{H}} \bar{\mathbf{H}}_k \mathbf{w}_j^{(n)}|^2 - 2 \sum_k \text{Re}\{(\boldsymbol{\theta}^{(n)})^{\mathrm{H}} \bar{\mathbf{H}}_k \mathbf{w}_k^{(n)}\} + K(1 + \sigma_n^2)$$

end while
$\boldsymbol{\theta} = \boldsymbol{\theta}^{(n)}$
$\mathbf{W} = \mathbf{W}^{(n)}$

where we have defined the constellation of discrete points $\bar{\mathcal{Q}}$ as

$$\bar{\mathcal{Q}} \triangleq \left\{0,\ e^{j\frac{2\pi}{2^{\bar{b}}}m}\right\}_{m=0}^{2^{\bar{b}}-1} \quad m \in \mathbb{Z},\ i = 1, \ldots, L; \tag{8.21}$$

to include the deactivated RIS antenna elements and the quantized phase shifts. Let the effective channel matrix of the k-th UE be defined as follows

$$\widetilde{\mathbf{H}}_k = \begin{bmatrix} \bar{\mathbf{H}}_k \mathbf{W}\mathbf{W}^{\mathrm{H}} \bar{\mathbf{H}}_k^{\mathrm{H}} & -\bar{\mathbf{H}}_k \mathbf{w}_k \\ -\mathbf{w}_k^{\mathrm{H}} \bar{\mathbf{H}}_k^{\mathrm{H}} & 0 \end{bmatrix} \in \mathbb{C}^{L+2 \times L+2}. \tag{8.22}$$

Lastly, let us define $\bar{\boldsymbol{\theta}} \triangleq [\boldsymbol{\theta}^{\mathrm{T}}\ f]^{\mathrm{T}}$ and $\bar{\Theta} = \bar{\boldsymbol{\theta}}\bar{\boldsymbol{\theta}}^{\mathrm{T}}$ with $|f|^2 = 1$. Hence, Problem (13) (P_SMSE_Lo) is equivalent to the following homogeneous quadratic problem

Algorithm 7 Lo-RISMA: Low-Resolution RISMA Algorithm

Initialize $\mathbf{W}^{(0)}$, $\text{SMSE}^{(0)}$ and ξ

$n \leftarrow 1$

while $\left|\left(\text{SMSE}^{(n)} - \text{SMSE}^{(n-1)}\right)/\text{SMSE}^{(n)}\right| > \xi$ **do**

$$\widetilde{\mathbf{H}}_k = \begin{bmatrix} \bar{\mathbf{H}}_k \mathbf{W}\mathbf{W}^{\mathrm{H}} \bar{\mathbf{H}}_k^{\mathrm{H}} & -\bar{\mathbf{H}}_k \mathbf{w}_k \\ -\mathbf{w}_k^{\mathrm{H}} \bar{\mathbf{H}}_k^{\mathrm{H}} & 0 \end{bmatrix}, \quad k = 1, \ldots, K$$

$$\hat{\bar{\boldsymbol{\theta}}}^{(n)} = \underset{\bar{\boldsymbol{\theta}}}{\operatorname{argmin}} \sum_k \bar{\boldsymbol{\theta}}^{\mathrm{H}} \widetilde{\mathbf{H}}_k \bar{\boldsymbol{\theta}}$$

$$\text{s.t.} \quad \bar{\boldsymbol{\theta}} \in \bar{\mathcal{Q}}^{L+1}$$

$$\bar{\boldsymbol{\theta}} = [\boldsymbol{\theta} \ f], \quad |f|^2 = 1$$

$\boldsymbol{\theta}^{(n)} = (c^{(n)})^* \hat{\bar{\boldsymbol{\theta}}}^{(n)}$

$\bar{\mathbf{H}} = [\bar{\mathbf{H}}_1^{\mathrm{H}} \boldsymbol{\theta}^{(n)}, \ldots, \bar{\mathbf{H}}_K^{\mathrm{H}} \boldsymbol{\theta}^{(n)}]$

$$\mu = \frac{K\sigma_n^2}{P}$$

$\bar{\mathbf{W}} = \left(\bar{\mathbf{H}}\bar{\mathbf{H}}^{\mathrm{H}} + \mu \mathbf{I}_M\right)^{-1} \bar{\mathbf{H}}$

$$\mathbf{W}^{(n)} = \sqrt{P} \frac{\bar{\mathbf{W}}}{\|\bar{\mathbf{W}}\|_{\mathrm{F}}}$$

$$\text{SMSE}^{(n)} = \sum_k \sum_j |(\boldsymbol{\theta}^{(n)})^{\mathrm{H}} \bar{\mathbf{H}}_k \mathbf{w}_j^{(n)}|^2 - 2\sum_k \text{Re}\{(\boldsymbol{\theta}^{(n)})^{\mathrm{H}} \bar{\mathbf{H}}_k \mathbf{w}_k^{(n)}\} + K(1+\sigma_n^2)$$

end while

$\boldsymbol{\theta} = \boldsymbol{\theta}^{(n)}$

$\mathbf{W} = \mathbf{W}^{(n)}$

Problem 14 (P_SMSE_LoE)**.**

$$\begin{aligned} \min_{\bar{\boldsymbol{\theta}}, \bar{\Theta}} \quad & \sum_k \text{tr}(\widetilde{\mathbf{H}}_k \bar{\Theta}) \\ \text{s.t.} \quad & \text{diag}(\bar{\Theta}) \in \{0,1\}; \\ & \bar{\Theta}_{L+1,L+1} = \bar{\Theta}_{L+2,L+2} = 1; \\ & \begin{bmatrix} \bar{\Theta} & \bar{\boldsymbol{\theta}} \\ \bar{\boldsymbol{\theta}}^{\mathrm{T}} & 1 \end{bmatrix} \succeq \mathbf{0}; \\ & \text{rank}(\bar{\Theta}) = 1. \end{aligned}$$

Following the results in [116, 117], we relax Problem 14 (P_SMSE_LoE) by removing the rank constraint and substituting the binary constraint on the diagonal of $\bar{\Theta}$ with the convex constraint $\mathbf{0} \leq \text{diag}(\bar{\Theta}) \leq \mathbf{1}$. Let $\bar{\Theta}^*$ denote the solution of Problem 14. By applying the Gaussian

randomization method in [113], we use $\bar{\Theta}^*$ to generate V random vectors $\mathbf{t}_v \sim \mathscr{CN}(\mathbf{0}, \bar{\Theta}^*)$. Such vectors are then quantized into the nearest point within the constellation $\bar{\mathscr{Q}}$, thus obtaining the set of V vectors $\{\bar{\mathbf{t}}_v\}$. We then obtain an approximate solution of Problem 14 as follows

$$\bar{\mathbf{t}}^\star = \underset{v=1,\ldots,V}{\operatorname{argmin}} \sum_k \bar{\mathbf{t}}_l^{\mathrm{T}} \tilde{\mathbf{H}}_k \bar{\mathbf{t}}_l. \tag{8.23}$$

Let us obtain $\hat{\mathbf{t}}^\star$ from $\bar{\mathbf{t}}^\star = [(\hat{\mathbf{t}}^\star)^{\mathrm{H}} \; f^\star]^{\mathrm{H}}$. A suboptimal solution to Problem 13 (P_SMSE_Lo) is thus given by

$$\boldsymbol{\theta} = f^\star \hat{\mathbf{t}}^\star. \tag{8.24}$$

Lastly, note that such optimization framework can be readily extended to any discrete set of phase shifts by simply changing the definition of $\bar{\mathscr{Q}}$ in Eq. (8.21) and modifying accordingly the quantization operation on the random vectors $\{\mathbf{t}_v\}$.

8.3 Numerical Results and Discussion

We present numerical results to analyze the benefits of the proposed algorithms both in the single UE case as per Section 8.1 and in a general multi-UE setting as per Section 8.2. Moreover, we show that our proposed scheme provides substantial gains compared to conventional massive MIMO schemes such as ZF or MMSE precoding (without the aid of RIS) as the transmit power P, the number of BS antennas M and the network area radius vary on a broad range of values. Finally, we show that similar outstanding gains can be attained even when considering RIS as a low-resolution surface whose antenna elements are activated in a binary fashion thereby introducing only uniformly spaced discrete phase shifts.

8.3.1 Channel model

The channel model used for our numerical results is defined as in Chapter 2. The LoS component of $\mathbf{h}_k$ is defined as

$$\mathbf{h}_{k,\mathrm{LoS}} \triangleq \sqrt{\gamma_k}\, \mathbf{a}(\theta_k) \in \mathbb{C}^{M\times 1}, \tag{8.25}$$

where $\gamma_k = d_k^{-\alpha}$ is the large-scale fading coefficient with α the LoS pathloss exponent and $\mathbf{a}(\theta_k)$ is the ULA response vector at the BS for the given steering angle θ_k defined as in Eq. (2.1). In a similar way, we define the NLoS component as the following

$$\mathbf{h}_{k,\mathrm{NLoS}} \triangleq \sqrt{\frac{\gamma_k}{P_k}} \sum_{p=1}^{P_k} \eta_{k,p}\, \mathbf{a}(\theta_{k,p}) \in \mathbb{C}^{M\times 1}, \tag{8.26}$$

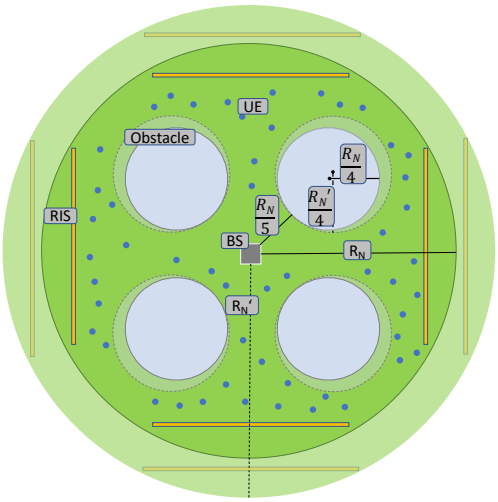

Figure 8.1 – Single-BS scenario where multiple obstacles and RISs are placed while UEs are normally distributed within a R_{N}-radius area.

where $\gamma_k = \mathbf{d}_k^{-\beta}$ with β the NLoS pathloss exponent, $\eta_{k,p} \sim \mathscr{CN}(0,1)$, P_k and $\theta_{k,p}$ are the small-scale fading coefficient, the number of scattered paths and the steering angle of the p-th scattered path between the BS and UE k, respectively. The (deterministic) LoS component of the channel between the BS and the RIS is defined as

$$\mathbf{G}_{\mathrm{LoS}} \triangleq \sqrt{\gamma_G}\mathbf{b}(\psi_A)\mathbf{a}(\psi_D)^{\mathrm{H}} \in \mathbb{C}^{L\times M}, \tag{8.27}$$

where $\gamma_G = d_1^{-\alpha}$ is the large-scale fading coefficient with $\mathbf{b}(\psi_A)$ the PLA response vector, which models the RIS response for the steering angle $\psi_A = (\psi_{A,x}, \psi_{A,z})$. The NLoS component of the BS-RIS link is defined as

$$\mathbf{G}_{\mathrm{NLoS}} \triangleq \sqrt{\frac{\gamma_G}{P_G}} \sum_{p=1}^{P_G} \mathbf{G}_p^{(w)} \circ \left(\mathbf{b}(\psi_{A,p})\mathbf{a}(\psi_{D,p})^{\mathrm{H}}\right) \in \mathbb{C}^{L\times M} \tag{8.28}$$

where $\gamma_G = d_1^{-\beta}$, P_G is the total number of scattered paths, $\mathbf{G}^{(w)}$ represents the small-scale fading coefficients of the p-th path with $\mathrm{vec}(\mathbf{G}_p^{(w)}) \sim \mathscr{CN}(\mathbf{0}, \mathbf{I}_{NM})$, and $\psi_{A,p}$ and $\psi_{D,p}$ are the AoA and AoD of the p-th path, respectively. Lastly, the LoS component of the RIS-UE k link is defined as

$$\mathbf{h}_{k,\mathrm{LoS}}^r = \sqrt{\gamma_k^r}\mathbf{b}(\psi_k) \in \mathbb{C}^{L\times 1}, \tag{8.29}$$

where $\gamma_k^r = d_{2,k}^{-\alpha}$ is the large-scale fading coefficient. The NLoS component of the RIS-UE k link is defined as the following

$$\mathbf{h}_{k,\text{NLoS}}^r \triangleq \sqrt{\frac{\gamma_k^r}{P_k^r}} \sum_{p=1}^{P_k} \eta_{k,p}\, \mathbf{b}(\psi_{k,p}) \in \mathbb{C}^{L\times 1}, \tag{8.30}$$

where $\gamma_k^r = d_{2,k}^{-\beta}$ and $\eta_{k,p} \sim \mathscr{CN}(0,1)$, P_k^r and $\psi_{k,p}$ denote the small-scale fading coefficient, the number of scattered paths and the steering angle of the p-th scattered path related to the RIS-UE k link, respectively.

8.3.2 Power scaling law

We derive the power scaling law of the channel model proposed in Section 8.3.1. For the sake of clarity, we focus on a single UE and single BS antenna case, i.e., $M = 1$ and hence $G \equiv g$ and $\mathbf{w}_{\text{MRT}} \equiv w_{\text{MRT}}$. Moreover, we assume that $\mathbf{h}^r \sim \mathscr{CN}(\mathbf{0}, \gamma^r \mathbf{I}_L)$, $\mathbf{g} \sim \mathscr{CN}(\mathbf{0}, \gamma_G \mathbf{I}_L)$ and $h \sim \mathscr{CN}(0,\gamma)$. The average receive power at the UE is given by

$$\begin{aligned} P_{\text{UE}} &= \mathbb{E}\left[\left\| \left(\left(\mathbf{h}^r\right)^{\text{H}} \mathbf{\Phi} \mathbf{g} + h^{\text{H}}\right) w_{\text{MRT}} \right\|^2\right] && (8.31)\\ &= P\left(\mathbb{E}\left[\left\| \left(\mathbf{h}^r\right)^{\text{H}} \mathbf{\Phi} \mathbf{g} \right\|^2\right] + \mathbb{E}[|h|^2]\right) \\ &= P\left(\mathbb{E}\left[\left| \sum_{i=1}^{L} |h_i^r||g_i| e^{j(\phi_i - \arg(h_i^r) + \arg(g_i))} \right|^2\right] + \gamma\right) \\ &\leq P\left(\frac{\pi^2}{16} d_2^{-\alpha}\, d_1^{-\alpha}\, L^2 + d^{-\alpha}\right). && (8.32) \end{aligned}$$

In Eq. (8.31) we assume that $\mathbf{h}^r$, $\mathbf{g}$ and h are statistically independent and Eq. (8.32) follows by assuming optimal choice of the RIS phase shifts as $\phi_i = \arg(h_i^r) - \arg(g_i)$, $\forall i$ and the fact that $\mathbb{E}[|h_i^r|^2|g_i|^2] = \pi^2 \gamma^r \gamma_G / 16$. The receive power thus scales as the inverse of the product of the distance of the individual paths from the BS to the RIS and from the RIS to the UE. Additionally, it scales as the square of the number of the RIS reflecting elements L (in accordance with recent works on pathloss modelling [55, 57, 63, 64]). Hence, by increasing the number of RIS antenna elements, we can counteract the decrease in receive power due to the distance of the combined path from the BS to RIS and from the RIS to the UE. This notably suggests that *RISs can be used smartly to effectively increase the coverage area of wireless networks.*

8.3.3 Scenario and setting parameters

As a special case of the general scenario described in Chapter 2, we consider a circular single-cell network of radius R_N with a central BS as depicted in Fig. 8.1. Here, our goal is to evaluate the performance of the proposed scheme in terms of the sum rate defined in Eq. (7.2) while

increasing the radius of the network area to prove how the considered RIS-aided network is effective in increasing the coverage area of cellular networks. Indeed, we vary R_N for a fixed number of UEs K.

For each value of R_N we average our simulations over 1000 different realizations of the UEs' positions, according to a uniform distribution over the considered circular area. There are four circular obstacles, which determine whether each UE is in LoS with the BS or not. To maintain consistency, we fix the radii of such obstacles to $R_N/4$ and the distance from the BS to the centers of said obstacles to $R_N/4 + R_N/5$. Moreover, we assume that there are four different RISs in LoS with the BS, each one with $L_x = L_y = \sqrt{L}$ antenna elements, positioned at distance R_N from the BS and angles 0, $\pi/2$, π and $3\pi/2$, respectively. Hence, for each RIS $d_1 = R_N$, $\psi_{A,x} = \pi$, $3\pi/2$, 0 and $\pi/2$ with $\psi_{A,z} = 0$, respectively. Furthermore, the AoD are $\psi_D = 0$, $\pi/2$, π and $3\pi/2$, respectively. Each UE k is served by a single RIS, according to the highest average channel power gain $\bar{\gamma}_k$ of the corresponding link, defined as the following

$$\begin{aligned}\bar{\gamma}_k &= \mathbb{E}[\|\mathbf{h}_k^r\|^2] \\ &= \frac{K_{h_k^r}^r}{1+K_{h_k^r}^r}\gamma_k^r L + \frac{1}{1+K_{h_k^r}^r}\gamma_k^r L \\ &= \begin{cases} d_{2,k}^{-\alpha} L & \text{if LoS} \\ d_{2,k}^{-\beta} L & \text{if NLoS} \end{cases}. \end{aligned} \tag{8.33}$$

Hence, we assume that each UE k is served by the closest RIS in terms of distance.[2] For simplicity we let $K_{h_k^r}^r = \bar{K}_{h^r}^r$, $P_k^r = \bar{P}^r$, $P_k = \bar{P}$, $K_{h_k}^r = K_h^r$. We set $\bar{K}_{h^r}^r = \bar{K}_{h^r,\text{LoS}}^r$, $K_h^r = K_{h,\text{LoS}}$ for LoS UEs while we let $\bar{K}_{h^r}^r = \bar{K}_{h^r,\text{NLoS}}^r$, $K_h^r = K_{h,\text{NLoS}}^r$ for NLoS UEs. All simulations parameters are set as per Table 8.1, unless otherwise stated.

Table 8.1 – RIS-aided network: Simulation parameters

Parameter	**Value**	**Parameter**	**Value**	**Parameter**	**Value**	**Parameter**	**Value**
L	100	L_x	10	K_G^r	2.5	P_G	$2LM$
α	2	β	4	$\bar{K}_{h^r,\text{LoS}}^r$	2.5	$\bar{K}_{h^r,\text{NLoS}}^r$	0
$\bar{P}$	$2L$	$K_{h,\text{LoS}}^r$	2	$K_{h,\text{NLoS}}^r$	0	K	12
L_y	10	M	8	$\bar{P}^r$	$2M$	σ_n^2	-80 dBm

8.3.4 Single-UE case

In the single UE case, we set $L_x = L_y = 5$, $K_h^r = 0$, $K_{h^r}^r = 2.5$, and $\theta = 0$. In addition, we assume that a single RIS is at distance $d_1 = 25$ m from the BS with AoD $\psi_D = \pi/4$ and AoA $\psi_A = 5\pi/4$

[2] Note that when (unlikely) more than one RIS is at the same distance from UE k, we solve the conflict by simply flipping a coin.

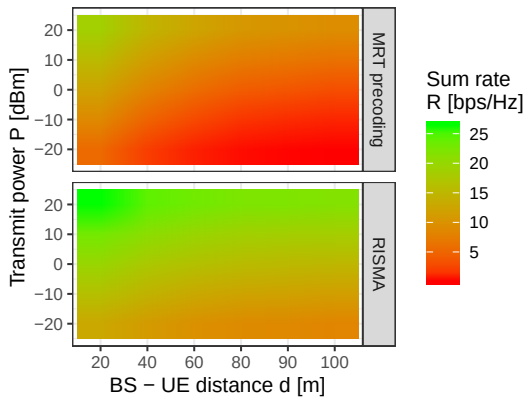

Figure 8.2 – Average sum rate in the single-UE case obtained with the proposed RISMA algorithm (bottom plot) and with conventional MRT precoding (upper plot) versus the transmit power P at the BS for different values of BS-UE distance d.

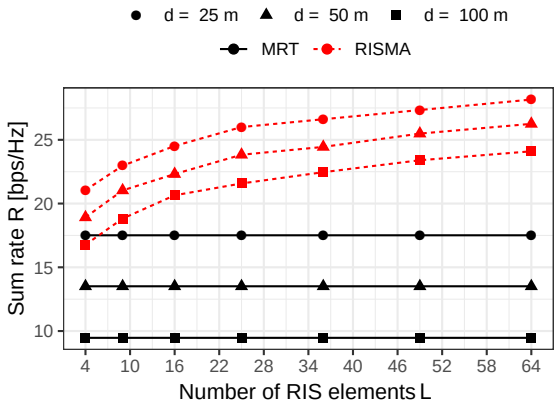

Figure 8.3 – Average sum rate in the single-UE case obtained with the proposed RISMA algorithm (red lines) and with conventional MRT precoding (black lines) versus the number of RIS elements L with $P = 24$ dBm and for different values of the distance between the BS and the UE d.

while we vary d as the distance from the BS to the UE. The distance from the RIS to the UE and the AoD ψ are thus calculated based on the aforementioned parameters.

Fig. 8.2 shows the average sum rate R obtained with the proposed RIS-aided optimization in Problem 10 (bottom plot) versus conventional MRT precoding (upper plot) without the aid of a RIS, defined as in Eq. (8.1) with $\mathbf{\Phi} = \mathbf{0}$ versus the transmit power P at the BS and for different values of distance d from the BS to the UE. While both schemes exhibit an increasing sum rate with the transmit power P, our proposed scheme consistently outperforms a conventional network with no RIS. Moreover, the gain further increases with d demonstrating how the effectiveness of a RIS in increasing the coverage area of wireless networks. For example RISMA can support up to $d = 90$ m with a target sum rate of 20 bps/Hz, thus increasing the coverage

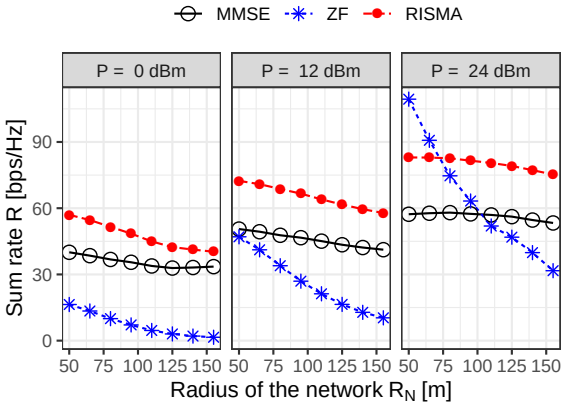

Figure 8.4 – Average sum rate in the multi-UE case obtained with the proposed RISMA algorithm (red curves), with conventional MMSE precoding (black curves) and with conventional ZF precoding (red green curves) versus the radius of the network area R_N and for different values of the transmit power P.

area of about 350% with respect to conventional MRT precoding with no RIS. Indeed, as the UE moves far away from the BS, conventional MRT suffers from the diminishing power in the channel $\mathbf{h}$. On the contrary the RIS-aided scheme is able to counteract this effect by steering the transmitted signal upon the RIS and towards the UE.

In Fig. 8.3 we show the average sum rate R obtained with the proposed RIS-aided optimization (red lines) versus conventional MRT (black lines) with $P = 24$ dBm versus the number of RIS elements L and for different values of the BS-UE distance d. While the benefits introduced by adding antenna elements on the RIS are clear, interestingly the conventional MRT scheme without the aid of the RIS attains similar performance to the proposed RIS-aided scheme only for small values of L and d. This further supports our claim that RISs can be effectively used to increase the coverage area of wireless networks at low expenses, i.e., limited number of antenna elements.

8.3.5 Multi-UE case

In the multi-UE the simulation parameters are set as per Table 8.1 unless otherwise stated. The values of $\{d_k\}_{k=1}^K$, $\{\theta_k\}_{k=1}^K$, $\{d_{2,k}\}_{k=1}^K$ and $\{\psi_k\}_{k=1}^K$ are calculated based on the UE positions of each random realization. We compare our proposed algorithms against two benchmark schemes, namely MMSE precoding defined as per [101]:

$$\mathbf{W}_{\text{MMSE}} = \sqrt{P}\frac{\left(\mathbf{H}\mathbf{H}^{\text{H}} + \frac{M\sigma_n^2}{P}\mathbf{I}_M\right)^{-1}\mathbf{H}}{\left\|\left(\mathbf{H}\mathbf{H}^{\text{H}} + \frac{M\sigma_n^2}{P}\mathbf{I}_M\right)^{-1}\mathbf{H}\right\|_{\text{F}}}, \tag{8.34}$$

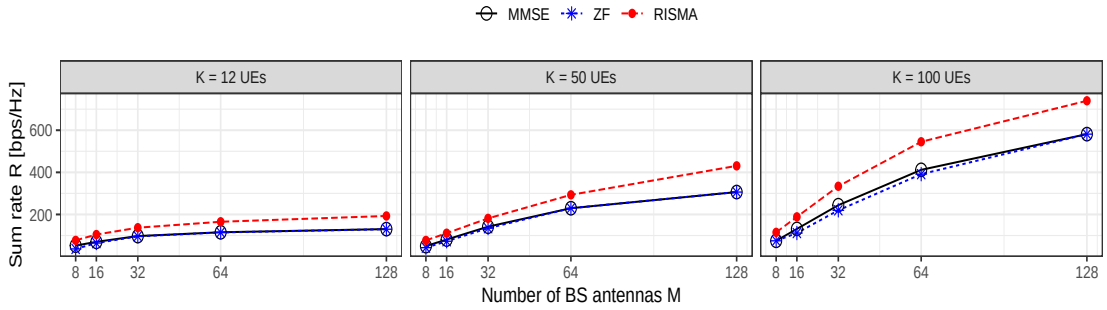

Figure 8.5 – Average sum rate in the multi-UE case obtained with the proposed RISMA algorithm (red line), with conventional MMSE precoding (black line) and with conventional ZF precoding (blue line) versus the number of BS antennas M, for fixed network area radius $R_N = 150$ m, transmit power $P = 24$ dBm and for different number of UEs K.

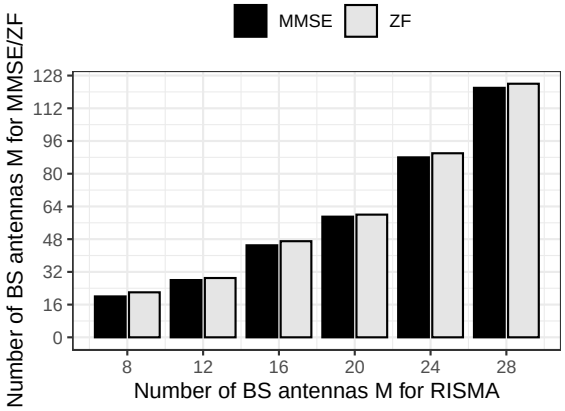

Figure 8.6 – Number of BS antennas M required by the MMSE (black) and ZF (blue) precoding schemes versus the number of BS antennas required by the proposed RISMA algorithm for the same target average sum rate, fixed network area radius $R_N = 100$ m and transmit power $P = 24$ dBm.

with $\mathbf{H} = [\mathbf{h}_1, \ldots, \mathbf{h}_K]$ and ZF precoding defined as

$$\mathbf{W}_{\mathrm{ZF}} = \sqrt{P}\frac{\mathbf{H}\left(\mathbf{H}^{\mathrm{H}}\mathbf{H}\right)^{-1}}{\|\mathbf{H}\left(\mathbf{H}^{\mathrm{H}}\mathbf{H}\right)^{-1}\|_{\mathrm{F}}}. \tag{8.35}$$

Fig. 8.4 shows the average sum rate R in the multi-UE case obtained with the proposed RISMA algorithm (solid red line), with conventional MMSE precoding (dashed black line) and ZF precoding (dashed green line) versus the radius of the network area R_N and for different values of the transmit power P. While the ZF scheme obtains the best results for small cells and high transmit power, the proposed RISMA algorithm achieves higher throughput for cells larger than say 75 m or a low-to-moderate transmit power. This is because as the radius of

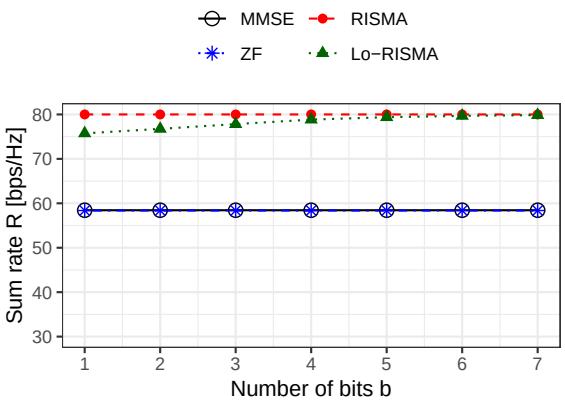

Figure 8.7 – Average sum rate in the multi-UE case obtained with the new Lo-RISMA algorithm (green line), with the novel RISMA algorithm (red line), with conventional MMSE precoding (black line) and with conventional ZF precoding (blue line) versus the number of quantization bits $\bar{b}$, for fixed network area radius $R_N = 100$ m and transmit power $P = 24$ dBm.

the network area increases, it becomes infeasible to design orthogonal beamformers with ZF precoding if multiple UEs are close to each other and far from the BS. Indeed, according to the proposed model, the channel response $\mathbf{h}_k$ depends essentially on the AoD θ_k and distance d_k, plus the NLoS components, which carry significantly less power. Hence, UEs who are close to each other exhibit statistically similar channels, thus limiting the performance of ZF precoding due to interference among neighboring UEs. In contrast, the use of the RIS greatly alleviates interference even for closely spaced UEs in large networks thanks to steering operated by the RIS. Additionally, RISMA outperforms MMSE precoding over all the considered range of network radii and transmit powers due to the coherent sum of both the contribution of the direct path from the BS to the UE and the contribution steered by the RIS towards the intended UE.

In Fig. 8.5, for a fixed network area radius $R_N = 150$ m and transmit power $P = 24$ dBm, we vary the number of BS antennas M and compare the proposed RISMA algorithm against both MMSE and ZF precoding in terms of sum rate. We evaluate three different scenarios by increasing the number of simultaneous UEs up to $K = 100$, which reasonably unveils a classical IoT environment. Note that the gain brought by adding BS antennas is larger in RISMA algorithm than the two considered benchmarks since they are limited by interference due to neighboring UEs. In addition, the proposed method benefits in terms of sum rate from an increase in the number of UEs while maintaining a simple and scalable optimization routine, demonstrating its relevance in IoT scenarios. Moreover, RISMA is considerably more energy-efficient. This is made evident in Fig. 8.6 that shows the number of equivalent antennas needed by either our MMSE and ZF benchmarks to achieve the same sum gain performance than our approach with $M = \{8, 12, 16, 20, 24, 28\}$ antennas. For instance, given a target sum

rate equal to 100 bps/Hz, RISMA requires a number of BS antennas that is ~ 67% lower.

Lastly, Fig. 8.7 shows the average sum rate R obtained with the proposed Lo-RISMA, i.e., when the RIS is a low resolution metasurface, the proposed RISMA algorithm, i.e., with an ideal RIS, conventional MMSE and ZF precoding versus the number of quantization bits $\bar{b}$ for fixed network area radius R_N = 100 m and transmit power P = 24 dBm. As the number of quantization bits increases, the Lo-RISMA algorithm approaches the performance of the ideal RISMA algorithm. Moreover, even for a single bit quantization our proposed method achieves better performance than the considered benchmark schemes thus demonstrating the feasibility of RIS-aided networks.

Remarkably, both the proposed RISMA and Lo-RISMA algorithms converge within few iterations, specifically, between 3 to 10 iterations. Note that the observed lower limit in the number of iterations is due to the random initialization of the optimization variables $\mathbf{W}$ and $\boldsymbol{\theta}$ in both the proposed algorithms.

8.4 Conclusions

In this part we have introduced the concept of RIS highlighting its key characteristics and advantages. In particular, two RIS-aided beamforming solutions have been proposed, RISMA and Lo-RISMA, for addressing massive IoT access challenges in beyond-5G networks. We have analyzed RIS benefits to cope with NLoS issues in dense urban environments where massive IoT deployments are expected in the near future.

Our contributions are: i) a novel mathematical framework to minimize the SMSE of RIS-aided beamforming communication systems, ii) RISMA, a low-complexity scheme that finds a simple and effective solution for such systems, iii) Lo-RISMA, an efficient algorithm for deployments with low-resolution meta-surfaces, and iv) a numerical evaluation that shows substantial gains in terms of sum rate performance, i.e. 40% gain over an MMSE precoder and 20% to 120% with respect to a ZF precoder, depending on the network radius.

Part V

Concluding Remarks

Chapter 9

Conclusions and Future Work

This thesis focuses on the design of novel scalable multi-antenna methods for performance enhancement of a beyond-5G massive access scenario. In Part I, we describe the limitations of current state-of-the-art multi-antenna technologies and associated open challenges. Indeed, existing solutions suffer from scalability issues due to the large number of heterogeneous UEs to be served and motivate a re-design of signal processing and transmission schemes. The considered system model is described in Chapter 2, where we provide the main assumptions, physical quantities of interest, and performance metrics. In the subsequent parts of this thesis, we focus on different optimization aspects, which are all special cases of the aforementioned general model.

In Part II, we tackle the problem of CSI overhead reduction and interference suppression in a massive MIMO system by introducing the concept of covariance shaping, i.e., a novel approach that ensures statistical favorable propagation among interfering UEs. Covariance shaping consists in applying a statistical beamformer at each UE as to enforce a statistical separation of interfering transmissions in space and therefore effectively shaping the statistics of the channel perceived by the BS. Such beamformers, denoted as covariance shaping vectors, are obtained via a simple iterative algorithm with provable convergence targeting the minimization of the inter-UE interference variance and are used both for uplink pilot decontamination and downlink data transmission. Moreover, we point out that the commonly used Kronecker channel model represents an over-simplification of the true nature of MIMO channels since it does not allow to modify the channel statistics on one end of the link as perceived at the other end. In this respect, we turn a generally inconvenient non-Kronecker channel model into a benefit. Despite sacrificing some of the available degrees of freedom, we show that the proposed method is effective in enforcing partial or full statistical orthogonality among neighboring UEs and results in substantial gains in terms of system sum rate compared to conventional reference scenarios where the multiple antennas at the UE-side are used for spatial multiplexing with no concern for pilot contamination. Practical implementations of

covariance shaping would require either a centralized processing at the BS who would then inform each UE of its corresponding covariance shaping vector, or a distributed processing performed directly at the UEs. The latter solution could be tackled in future works in order to identify the amount of information necessary to compute the covariance shaping vectors that needs to be shared among the UEs. Indeed, there exists an underlying trade-off between communication overhead and sum rate performance resulting from a distributed implementation of covariance shaping.

The study of a two-phase cooperative multicasting framework that leverages both multi-antenna transmission at the BS and D2D communications between the UEs is the main topic of Part III. Contrarily to existing state-of-the-art, we propose efficient algorithms to tackle the optimization of both the precoding strategy at the BS and the multicast rate over the two phases subject to some outage constraint under three different CSIT configurations, i.e., perfect, statistical, and topological CSIT. Such algorithms, namely D2D-MAM, D2D-SMAM, and D2D-TMAM for the three cases, respectively, find the best possible candidate relay set to be targeted via beamforming at the BS and the maximum achievable multicast rate for the given outage constraint. We show that the proposed schemes significantly outperform conventional single-phase multi-antenna multicasting and two-phase single-antenna multicasting in all the considered CSIT configurations. Remarkably, they allow to effectively overcome the vanishing behavior of the multicast rate and achieve an increasing performance as the UE population grows large. However, the proposed schemes share the underlying assumption that the UEs are perfectly synchronized such that no interference is caused during the second phase of D2D retransmissions. This assumption may be relaxed in future works by redesigning the aforementioned algorithms in order to accommodate practical synchronization issues. Other challenges yet to be explored are related to the interplay between the two phases in terms of time allocation and operations performed both at the UEs and at the BS. Indeed, as shown in [45, 46], the time allocation between the two phases should be optimized as a function of the distance of the UEs from the BS. Moreover, to further enhance the performance of the proposed schemes the signal received from the BS in the first phase could be stored at each UE (even if the received SNR is not sufficient to decode the signal) and combined together with the signal retransmitted via the D2D links in the second phase to obtain higher multicast rate overall.

In Part IV, we explore the integration of the novel concept of RIS in beyond-5G mmWave massive IoT communications as a means to overcome the current associated limitations, which are essentially due to high propagation losses and the large number of UEs to be served. Specifically, we analyze how RISs can cope with NLoS issues in dense urban environments and introduce a novel mathematical framework to minimize the SMSE of a RIS-aided beamforming communication system. Such an objective function is purposely chosen to guarantee both high performance, and efficiency and scalability of the resulting optimization procedure.

Indeed, when employing alternating optimization the SMSE reveals a convex structure in the two optimization variables separately, namely the beamforming at the BS and the RIS parameters, which allows to find closed-form solutions to the resulting sub-problems. In this respect, we propose two RIS-aided beamforming solutions, RISMA and Lo-RISMA, i.e., a low-complexity scheme that finds a simple and effective solution by iterating over two closed-form solutions, and an efficient algorithm for deployments with low-resolution RISs, respectively. In our numerical evaluation we demonstrate the effectiveness of the proposed RISMA approach by showing substantial gains in terms of sum rate performance of up to 40% over a conventional MMSE precoder and from 20% to 120% with respect to a ZF precoder, depending on the network radius. Moreover, the performance of Lo-RISMA is shown to approach the one obtained in the ideal case (i.e., with the RISMA algorithm that assumes an ideal RIS) even for small values of angular resolution at the RIS, thus demonstrating the feasibility of RISs. Nevertheless, the proposed approaches are based on the availability of perfect CSIT, which might be challenging to acquire in practice. Hence, in the future we will study how to extend the proposed framework to the case of statistical CSIT as in [118]. Such an approach would bring together the benefits of the chosen objective function in terms of performance and scalability, and the overhead reduction necessary to acquire instantaneous CSI, thus taking a further step towards successfull deployments of RIS-aided networks.

Appendices

Appendix A

Derivations of the effective SINR in Eq. (4.13)

Given the multi-UE effective channel matrix $\bar{\mathbf{G}} = [\bar{\mathbf{g}}_1^{\mathrm{T}}, \ldots, \bar{\mathbf{g}}_K^{\mathrm{T}}]^{\mathrm{T}} \in \mathbb{C}^{K \times M}$, where the effective MISO channels $\{\bar{\mathbf{g}}_k\}_{k=1}^{K}$ are mutually independent, we have

$$\mathbb{E}[\|\bar{\mathbf{G}}\|_{\mathrm{F}}^2] = \mathbb{E}[\mathrm{tr}(\bar{\mathbf{G}}\bar{\mathbf{G}}^{\mathrm{H}})] \tag{A.1}$$

$$= \mathrm{tr}(\mathbb{E}[\bar{\mathbf{G}}\bar{\mathbf{G}}^{\mathrm{H}}]) \tag{A.2}$$

$$= \sum_{k=1}^{K} \mathrm{tr}(\bar{\mathbf{\Phi}}_k) \tag{A.3}$$

where we recall that $\bar{\mathbf{g}}_k \sim \mathcal{CN}(\mathbf{0}, \bar{\mathbf{\Phi}}_k)$.

Considering now a random vector $\mathbf{t} \in \mathbb{C}^{M \times 1}$ and a Hermitian matrix $\mathbf{A} \in \mathbb{C}^{M \times M}$, we have

$$\mathbb{E}[\mathbf{t}\mathbf{t}^{\mathrm{H}}\mathbf{A}\mathbf{t}\mathbf{t}^{\mathrm{H}}] = \left(\mathbb{E}\left[\sum_{u=1}^{M}\sum_{v=1}^{M} A_{uv} t_s^* t_t t_u^* t_v\right]\right)_{s,t=1}^{M} \tag{A.4}$$

where A_{uv} is the (u,v)th element of $\mathbf{A}$ and t_s is the sth element of $\mathbf{t}$, with

$$\mathbb{E}\left[A_{uu} t_s^* t_t t_u^* t_v\right] = \begin{cases} \mu_4 A_{uu}, & \text{if } s = t = u = v \\ \mu_2^2 A_{uu}, & \text{if } s = t \neq u = v \\ \mu_2^2 A_{uv}, & \text{if } s = u \neq t = v \\ 0, & \text{otherwise} \end{cases} \tag{A.5}$$

where μ_2 and μ_4 are the second- and fourth-order moments of $\mathbf{t}$, respectively. When $\mathbf{t} \sim \mathcal{CN}(\mathbf{0}, \mathbf{I}_M)$, we have $\mu_2 = 1$ and $\mu_4 = 2$, and we obtain

$$\mathbb{E}\left[\sum_{u=1}^{M}\sum_{v=1}^{M} A_{uv} t_s^* t_t t_u^* t_v\right] = \begin{cases} 2A_{tt} + (\mathrm{tr}(\mathbf{A}) - A_{tt}), & \text{if } s = t \\ A_{st}, & \text{if } s \neq t \end{cases} \tag{A.6}$$

which yields

$$\mathbb{E}[\mathbf{t}\mathbf{t}^{\mathrm{H}}\mathbf{A}\mathbf{t}\mathbf{t}^{\mathrm{H}}] = \mathbf{A} + \mathrm{tr}(\mathbf{A})\mathbf{I}_M. \tag{A.7}$$

Let us define $\bar{\mathbf{n}} \triangleq \mathbf{N}\mathbf{p}_p^{\mathrm{H}} \in \mathbb{C}^{M\times 1}$, which is distributed as $\mathscr{CN}(\mathbf{0}, \sigma_n^2\mathbf{I}_M)$. Hence, the variance of $\bar{\mathbf{g}}_k\hat{\bar{\mathbf{g}}}_k^{\mathrm{H}}$ can be expressed as

$$\begin{aligned}
\mathrm{Var}[\bar{\mathbf{g}}_k\hat{\bar{\mathbf{g}}}_k^{\mathrm{H}}] &= \mathbb{E}\big[|\bar{\mathbf{g}}_k\hat{\bar{\mathbf{g}}}_k^{\mathrm{H}}|^2\big] - \big|\mathbb{E}[\bar{\mathbf{g}}_k\hat{\bar{\mathbf{g}}}_k^{\mathrm{H}}]\big|^2 && \text{(A.8)}\\
&= \mathbb{E}\Bigg[\Bigg(\bar{\mathbf{g}}_k\bar{\mathbf{\Phi}}_k\mathbf{U}_k^{-1}\Bigg(\bar{\mathbf{g}}_k^{\mathrm{H}} + \sum_{j\in\mathscr{S}_p\setminus\{k\}}\sqrt{\frac{\rho_j}{\rho_k}}\bar{\mathbf{g}}_j^{\mathrm{H}} + \frac{1}{\sqrt{\rho_k}}\bar{\mathbf{n}}\Bigg)\Bigg)\\
&\quad\times\Bigg(\Bigg(\bar{\mathbf{g}}_k + \sum_{j\in\mathscr{S}_p\setminus\{k\}}\sqrt{\frac{\rho_j}{\rho_k}}\bar{\mathbf{g}}_j + \frac{1}{\sqrt{\rho_k}}\bar{\mathbf{n}}^{\mathrm{H}}\Bigg)\mathbf{U}_k^{-1}\bar{\mathbf{\Phi}}_k\bar{\mathbf{g}}_k^{\mathrm{H}}\Bigg)\Bigg]\\
&\quad - \Bigg|\mathbb{E}\Bigg[\bar{\mathbf{g}}_k\bar{\mathbf{\Phi}}_k\mathbf{U}_k^{-1}\Bigg(\bar{\mathbf{g}}_k^{\mathrm{H}} + \sum_{j\in\mathscr{S}_p\setminus\{k\}}\sqrt{\frac{\rho_j}{\rho_k}}\bar{\mathbf{g}}_j^{\mathrm{H}} + \frac{1}{\sqrt{\rho_k}}\bar{\mathbf{n}}\Bigg)\Bigg]\Bigg|^2 && \text{(A.9)}\\
&= \mathbb{E}[\bar{\mathbf{g}}_k\bar{\mathbf{\Phi}}_k\mathbf{U}_k^{-1}\bar{\mathbf{g}}_k^{\mathrm{H}}\bar{\mathbf{g}}_k\mathbf{U}_k^{-1}\bar{\mathbf{\Phi}}_k\bar{\mathbf{g}}_k^{\mathrm{H}}] + \sum_{j\in\mathscr{S}_p\setminus\{k\}}\frac{\rho_j}{\rho_k}\mathbb{E}[\bar{\mathbf{g}}_k\bar{\mathbf{\Phi}}_k\mathbf{U}_k^{-1}\bar{\mathbf{g}}_j^{\mathrm{H}}\bar{\mathbf{g}}_j\mathbf{U}_k^{-1}\bar{\mathbf{\Phi}}_k\bar{\mathbf{g}}_k^{\mathrm{H}}]\\
&\quad + \rho_k^{-1}\mathbb{E}[\bar{\mathbf{g}}_k\bar{\mathbf{\Phi}}_k\mathbf{U}_k^{-1}\bar{\mathbf{n}}\bar{\mathbf{n}}^{\mathrm{H}}\mathbf{U}_k^{-1}\bar{\mathbf{\Phi}}_k\bar{\mathbf{g}}_k^{\mathrm{H}}] - \big|\mathbb{E}[\bar{\mathbf{g}}_k\bar{\mathbf{\Phi}}_k\mathbf{U}_k^{-1}\bar{\mathbf{g}}_k^{\mathrm{H}}]\big|^2 && \text{(A.10)}
\end{aligned}$$

where in Eq. (A.9) we have used the expression of $\hat{\bar{\mathbf{g}}}_k$ in Eq. (4.4) and in Eq. (A.10) we have exploited the independence between $\bar{\mathbf{g}}_k$ and $\bar{\mathbf{g}}_j$, $\forall k \neq j$, and between $\bar{\mathbf{g}}_k$ and $\bar{\mathbf{n}}$. Since each $\bar{\mathbf{g}}_k$ can be expressed as $\bar{\mathbf{g}}_k = \bar{\mathbf{g}}_k^{(0)}\bar{\mathbf{\Phi}}_k^{\frac{1}{2}}$, where $\bar{\mathbf{g}}_k^{(0)} \in \mathbb{C}^{1\times M}$ is distributed as $\sim \mathscr{CN}(0, \mathbf{I}_M)$, we have

$$\begin{aligned}
\mathrm{Var}[\bar{\mathbf{g}}_k\hat{\bar{\mathbf{g}}}_k^{\mathrm{H}}] &= \mathbb{E}\big[\bar{\mathbf{g}}_k^{(0)}\bar{\mathbf{\Phi}}_k^{\frac{1}{2}}\bar{\mathbf{\Phi}}_k\mathbf{U}_k^{-1}\bar{\mathbf{\Phi}}_k^{\frac{1}{2}}(\bar{\mathbf{g}}_k^{(0)})^{\mathrm{H}}\bar{\mathbf{g}}_k^{(0)}\bar{\mathbf{\Phi}}_k^{\frac{1}{2}}\mathbf{U}_k^{-1}\bar{\mathbf{\Phi}}_k\bar{\mathbf{\Phi}}_k^{\frac{1}{2}}(\bar{\mathbf{g}}_k^{(0)})^{\mathrm{H}}\big]\\
&\quad + \sum_{j\in\mathscr{S}_p\setminus\{k\}}\frac{\rho_j}{\rho_k}\mathbb{E}\big[\bar{\mathbf{g}}_k^{(0)}\bar{\mathbf{\Phi}}_k^{\frac{1}{2}}\bar{\mathbf{\Phi}}_k\mathbf{U}_k^{-1}\bar{\mathbf{\Phi}}_j^{\frac{1}{2}}(\bar{\mathbf{g}}_j^{(0)})^{\mathrm{H}}\bar{\mathbf{g}}_j^{(0)}\bar{\mathbf{\Phi}}_j^{\frac{1}{2}}\mathbf{U}_k^{-1}\bar{\mathbf{\Phi}}_k\bar{\mathbf{\Phi}}_k^{\frac{1}{2}}(\bar{\mathbf{g}}_k^{(0)})^{\mathrm{H}}\big]\\
&\quad + \rho_k^{-1}\mathbb{E}\big[\bar{\mathbf{g}}_k^{(0)}\bar{\mathbf{\Phi}}_k^{\frac{1}{2}}\bar{\mathbf{\Phi}}_k\mathbf{U}_k^{-1}\bar{\mathbf{n}}\bar{\mathbf{n}}^{\mathrm{H}}\mathbf{U}_k^{-1}\bar{\mathbf{\Phi}}_k\bar{\mathbf{\Phi}}_k^{\frac{1}{2}}(\bar{\mathbf{g}}_k^{(0)})^{\mathrm{H}}\big] - \big|\mathbb{E}\big[\bar{\mathbf{g}}_k^{(0)}\bar{\mathbf{\Phi}}_k^{\frac{1}{2}}\bar{\mathbf{\Phi}}_k\mathbf{U}_k^{-1}\bar{\mathbf{\Phi}}_k^{\frac{1}{2}}(\bar{\mathbf{g}}_k^{(0)})^{\mathrm{H}}\big]\big|^2.
\end{aligned} \tag{A.11}$$

Rearranging the terms, we obtain

$$
\begin{aligned}
\mathrm{Var}[\bar{\mathbf{g}}_k\hat{\bar{\mathbf{g}}}_k^{\mathrm{H}}] &= \mathrm{tr}\Big(\bar{\mathbf{\Phi}}_k^{\frac{1}{2}}\bar{\mathbf{\Phi}}_k\mathbf{U}_k^{-1}\bar{\mathbf{\Phi}}_k^{\frac{1}{2}}\mathbb{E}\big[(\bar{\mathbf{g}}_k^{(0)})^{\mathrm{H}}\bar{\mathbf{g}}_k^{(0)}\bar{\mathbf{\Phi}}_k^{\frac{1}{2}}\mathbf{U}_k^{-1}\bar{\mathbf{\Phi}}_k\bar{\mathbf{\Phi}}_k^{\frac{1}{2}}(\bar{\mathbf{g}}_k^{(0)})^{\mathrm{H}}\bar{\mathbf{g}}_k^{(0)}\big]\Big) \\
&\quad + \sum_{j\in\mathscr{S}_p\setminus\{k\}}\frac{\rho_j}{\rho_k}\mathrm{tr}\Big(\mathbb{E}\big[(\bar{\mathbf{g}}_k^{(0)})^{\mathrm{H}}\bar{\mathbf{g}}_k^{(0)}\big]\bar{\mathbf{\Phi}}_k^{\frac{1}{2}}\bar{\mathbf{\Phi}}_k\mathbf{U}_k^{-1}\bar{\mathbf{\Phi}}_j^{\frac{1}{2}}\mathbb{E}\big[(\bar{\mathbf{g}}_j^{(0)})^{\mathrm{H}}\bar{\mathbf{g}}_j^{(0)}\big]\bar{\mathbf{\Phi}}_j^{\frac{1}{2}}\mathbf{U}_k^{-1}\bar{\mathbf{\Phi}}_k\bar{\mathbf{\Phi}}_k^{\frac{1}{2}}\Big) \\
&\quad + \rho_k^{-1}\mathrm{tr}\Big(\mathbb{E}\big[(\bar{\mathbf{g}}_k^{(0)})^{\mathrm{H}}\bar{\mathbf{g}}_k^{(0)}\big]\bar{\mathbf{\Phi}}_k^{\frac{1}{2}}\bar{\mathbf{\Phi}}_k\mathbf{U}_k^{-1}\mathbb{E}[\bar{\mathbf{n}}\bar{\mathbf{n}}^{\mathrm{H}}]\mathbf{U}_k^{-1}\bar{\mathbf{\Phi}}_k\bar{\mathbf{\Phi}}_k^{\frac{1}{2}}\Big) \\
&\quad - \mathrm{tr}\Big(\mathbb{E}\big[(\bar{\mathbf{g}}_k^{(0)})^{\mathrm{H}}\bar{\mathbf{g}}_k^{(0)}\big]\bar{\mathbf{\Phi}}_k^{\frac{1}{2}}\bar{\mathbf{\Phi}}_k\mathbf{U}_k^{-1}\bar{\mathbf{\Phi}}_k^{\frac{1}{2}}\Big)^2 \qquad \text{(A.12)} \\
&= \mathrm{tr}(\bar{\mathbf{\Phi}}_k^2\mathbf{U}_k^{-1}\bar{\mathbf{\Phi}}_k\mathbf{U}_k^{-1}\bar{\mathbf{\Phi}}_k) + \mathrm{tr}(\bar{\mathbf{\Phi}}_k\mathbf{U}_k^{-1}\bar{\mathbf{\Phi}}_k)^2 + \sum_{j\in\mathscr{S}_p\setminus\{k\}}\frac{\rho_j}{\rho_k}\mathrm{tr}(\bar{\mathbf{\Phi}}_k^2\mathbf{U}_k^{-1}\bar{\mathbf{\Phi}}_j\mathbf{U}_k^{-1}\bar{\mathbf{\Phi}}_k) \\
&\quad + \varrho_k^{-1}\mathrm{tr}(\bar{\mathbf{\Phi}}_k^2\mathbf{Q}_k^{-2}\bar{\mathbf{\Phi}}_k) - \mathrm{tr}(\bar{\mathbf{\Phi}}_k\mathbf{U}_k^{-1}\bar{\mathbf{\Phi}}_k)^2 \qquad \text{(A.13)} \\
&= \mathrm{tr}(\bar{\mathbf{\Phi}}_k^2\mathbf{U}_k^{-1}\bar{\mathbf{\Phi}}_k\mathbf{U}_k^{-1}\bar{\mathbf{\Phi}}_k) + \sum_{j\in\mathscr{S}_p\setminus\{k\}}\frac{\rho_j}{\rho_k}\mathrm{tr}(\bar{\mathbf{\Phi}}_k^2\mathbf{U}_k^{-1}\bar{\mathbf{\Phi}}_j\mathbf{U}_k^{-1}\bar{\mathbf{\Phi}}_k) + \varrho_k^{-1}\mathrm{tr}(\bar{\mathbf{\Phi}}_k^2\mathbf{Q}_k^{-2}\bar{\mathbf{\Phi}}_k) \qquad \text{(A.14)} \\
&= \mathrm{tr}\Big(\bar{\mathbf{\Phi}}_k^2\mathbf{U}_k^{-1}\Big(\bar{\mathbf{\Phi}}_k + \sum_{j\in\mathscr{S}_p\setminus\{k\}}\frac{\rho_j}{\rho_k}\bar{\mathbf{\Phi}}_j + \varrho_k^{-1}\mathbf{I}_M\Big)\mathbf{U}_k^{-1}\bar{\mathbf{\Phi}}_k\Big) \qquad \text{(A.15)} \\
&= \mathrm{tr}(\bar{\mathbf{\Phi}}_k^2\mathbf{U}_k^{-1}\bar{\mathbf{\Phi}}_k) \qquad \text{(A.16)}
\end{aligned}
$$

where in Eq. (A.13) we have used the property in Eq. (A.7). Finally, following similar steps, the expectation of $|\bar{\mathbf{g}}_k\hat{\bar{\mathbf{g}}}_j^{\mathrm{H}}|^2$ can be expressed as

$$
\begin{aligned}
\mathbb{E}\big[|\bar{\mathbf{g}}_k\hat{\bar{\mathbf{g}}}_j^{\mathrm{H}}|^2\big] &= \sum_{\ell\in\mathscr{S}_p\setminus\{j\}}\frac{\rho_\ell}{\rho_j}\mathrm{tr}\Big(\mathbb{E}\big[(\bar{\mathbf{g}}_k^{(0)})^{\mathrm{H}}\bar{\mathbf{g}}_k^{(0)}\big]\bar{\mathbf{\Phi}}_k^{\frac{1}{2}}\bar{\mathbf{\Phi}}_j\mathbf{Q}_j^{-1}\bar{\mathbf{\Phi}}_\ell^{\frac{1}{2}}\mathbb{E}\big[(\bar{\mathbf{g}}_\ell^{(0)})^{\mathrm{H}}\bar{\mathbf{g}}_\ell^{(0)}\big]\bar{\mathbf{\Phi}}_\ell^{\frac{1}{2}}\mathbf{Q}_j^{-1}\bar{\mathbf{\Phi}}_j\bar{\mathbf{\Phi}}_k^{\frac{1}{2}}\Big) \\
&\quad + \mathrm{tr}\Big(\mathbb{E}\big[(\bar{\mathbf{g}}_k^{(0)})^{\mathrm{H}}\bar{\mathbf{g}}_k^{(0)}\big]\bar{\mathbf{\Phi}}_k^{\frac{1}{2}}\bar{\mathbf{\Phi}}_j\mathbf{Q}_j^{-1}\bar{\mathbf{\Phi}}_j^{\frac{1}{2}}\mathbb{E}\big[(\bar{\mathbf{g}}_j^{(0)})^{\mathrm{H}}\bar{\mathbf{g}}_j^{(0)}\big]\bar{\mathbf{\Phi}}_j^{\frac{1}{2}}\mathbf{Q}_j^{-1}\bar{\mathbf{\Phi}}_j\bar{\mathbf{\Phi}}_k^{\frac{1}{2}}\Big) \\
&\quad + \rho_j^{-1}\mathrm{tr}\Big(\mathbb{E}\big[(\bar{\mathbf{g}}_k^{(0)})^{\mathrm{H}}\bar{\mathbf{g}}_k^{(0)}\big]\bar{\mathbf{\Phi}}_k^{\frac{1}{2}}\bar{\mathbf{\Phi}}_j\mathbf{Q}_j^{-1}\mathbb{E}[\bar{\mathbf{n}}\bar{\mathbf{n}}^{\mathrm{H}}]\mathbf{Q}_j^{-1}\bar{\mathbf{\Phi}}_j\bar{\mathbf{\Phi}}_k^{\frac{1}{2}}\Big) \qquad \text{(A.17)} \\
&= \sum_{\ell\in\mathscr{S}_p\setminus\{j\}}\frac{\rho_\ell}{\rho_j}\mathrm{tr}(\bar{\mathbf{\Phi}}_k\bar{\mathbf{\Phi}}_j\mathbf{Q}_j^{-1}\bar{\mathbf{\Phi}}_\ell\mathbf{Q}_j^{-1}\bar{\mathbf{\Phi}}_j) + \mathbb{1}_{\mathscr{S}_p}(k,j)\mathrm{tr}(\bar{\mathbf{\Phi}}_k\mathbf{Q}_j^{-1}\bar{\mathbf{\Phi}}_j)^2 \\
&\quad + \mathrm{tr}(\bar{\mathbf{\Phi}}_k\bar{\mathbf{\Phi}}_j\mathbf{Q}_j^{-1}\bar{\mathbf{\Phi}}_j\mathbf{Q}_j^{-1}\bar{\mathbf{\Phi}}_j) + \varrho_j^{-1}\mathrm{tr}(\bar{\mathbf{\Phi}}_k\bar{\mathbf{\Phi}}_j\mathbf{Q}_j^{-2}\bar{\mathbf{\Phi}}_j) \qquad \text{(A.18)} \\
&= \mathrm{tr}\Big(\bar{\mathbf{\Phi}}_k\bar{\mathbf{\Phi}}_j\mathbf{Q}_j^{-1}\Big(\bar{\mathbf{\Phi}}_j + \sum_{\ell\in\mathscr{S}_p\setminus\{j\}}\frac{\rho_\ell}{\rho_j}\bar{\mathbf{\Phi}}_\ell + \varrho_j^{-1}\mathbf{I}_M\Big)\mathbf{Q}_j^{-1}\bar{\mathbf{\Phi}}_j\Big) \\
&\quad + \mathbb{1}_{\mathscr{S}_p}(k,j)\mathrm{tr}(\bar{\mathbf{\Phi}}_k\mathbf{Q}_j^{-1}\bar{\mathbf{\Phi}}_j)^2 \qquad \text{(A.19)} \\
&= \mathrm{tr}(\bar{\mathbf{\Phi}}_k\bar{\mathbf{\Phi}}_j\mathbf{Q}_j^{-1}\bar{\mathbf{\Phi}}_j) + \mathbb{1}_{\mathscr{S}_p}(k,j)\,\mathrm{tr}(\bar{\mathbf{\Phi}}_k\mathbf{Q}_j^{-1}\bar{\mathbf{\Phi}}_j)^2. \qquad \text{(A.20)}
\end{aligned}
$$

Appendix B

Proof of Proposition 5

Since Problem 4 is convex, a given Γ_1 is optimal if and only if it satisfies the KKT conditions. Let us define the Lagrangian and its gradient as

$$\mathscr{L}(\Gamma_1, \mu, \Psi) \triangleq \sum_{k \in \mathscr{K}} \frac{1}{\gamma_k \mathbf{a}_k^{\mathrm{H}} \Gamma_1 \mathbf{a}_k} + \mu\big(\mathrm{tr}(\Gamma_1) - 1\big) - \mathrm{tr}(\Psi \Gamma_1), \tag{B.1}$$

$$\nabla \mathscr{L}(\Gamma_1, \mu, \Psi) \triangleq - \sum_{k \in \mathscr{K}} \frac{1}{\gamma_k (\mathbf{a}_k^{\mathrm{H}} \Gamma_1 \mathbf{a}_k)^2} \mathbf{a}_k \mathbf{a}_k^{\mathrm{H}} + \mu \mathbf{I}_M - \Psi \tag{B.2}$$

respectively, where we have introduced the dual variables $\mu \in \mathbb{R}$ and $\Psi \in \mathbb{C}^{M \times M}$. The KKT conditions of Problem 4 can be written as

$$\sum_{k \in \mathscr{K}} \frac{1}{\gamma_k (\mathbf{a}_k^{\mathrm{H}} \Gamma_1 \mathbf{a}_k)^2} \mathbf{a}_k \mathbf{a}_k^{\mathrm{H}} = \mu \mathbf{I}_M - \Psi, \tag{B.3a}$$

$$\mathrm{tr}(\Gamma_1) \leq 1, \ \Gamma_1 \succeq \mathbf{0}, \tag{B.3b}$$

$$\mu \geq 0, \ \Psi \succeq \mathbf{0}, \tag{B.3c}$$

$$\mu\big(\mathrm{tr}(\Gamma_1) - 1\big) = 0, \ \Psi \Gamma_1 = \mathbf{0}. \tag{B.3d}$$

The condition in Eq. (B.3a) suggests that the transmit covariance has the structure

$$\Gamma_1 = \sum_{k \in \mathscr{K}} w_k \mathbf{a}_k \mathbf{a}_k^{\mathrm{H}} \tag{B.4}$$

where $\sum_{k \in \mathscr{K}} w_k = 1/M$ implies $\mathrm{tr}(\Gamma_1) = 1$ and $\{w_k \geq 0\}_{k \in \mathscr{K}}$ implies $\Gamma_1 \succeq \mathbf{0}$. From Eq. (B.4), we can write

$$\mathbf{a}_k^{\mathrm{H}} \Gamma_1 \mathbf{a}_k = \sum_{j \in \mathscr{K}} w_j \phi_{kj} \tag{B.5}$$

where we have defined $\phi_{kj} \triangleq |\mathbf{a}_k^{\mathrm{H}} \mathbf{a}_j|^2$, with $\widetilde{\mathbf{\Phi}} \triangleq [\phi_{kj}]_{k,j \in \mathscr{K}} \in \mathbb{C}^{K \times K}$ being a symmetric matrix with diagonal elements equal to M^2. Plugging Eq. (B.4) into Eq. (B.3), the KKT conditions

become

$$\sum_{k\in\mathcal{K}} \frac{1}{\gamma_k\left(\sum_{j\in\mathcal{K}} w_j\phi_{kj}\right)^2}\mathbf{a}_k\mathbf{a}_k^{\mathrm{H}} = \mu\mathbf{I}_M - \Psi, \tag{B.6a}$$

$$\sum_{k\in\mathcal{K}} w_k = \frac{1}{M},\ \{w_k \geq 0\}_{k\in\mathcal{K}}, \tag{B.6b}$$

$$\mu \geq 0,\ \Psi \succeq \mathbf{0}, \tag{B.6c}$$

$$\mu\left(\sum_{k\in\mathcal{K}} w_k - \frac{1}{M}\right) = 0,\ \Psi\sum_k w_k\mathbf{a}_k\mathbf{a}_k^{\mathrm{H}} = \mathbf{0}. \tag{B.6d}$$

Let us define $\mathbf{w} \triangleq [w_1,\ldots,w_K]^{\mathrm{T}} \in \mathbb{R}^{K\times 1}$. Choosing the weights that satisfy Eq. (B.6b) allows us to set $\Psi = \mathbf{0}$ and, from Eq. (B.6a), we can show that

$$\mathbf{w} = \frac{1}{\sqrt{\mu M}}\widetilde{\mathbf{\Phi}}^{-1}\mathbf{b} \tag{B.7}$$

where we have defined

$$\mathbf{b} \triangleq \left[\frac{1}{\sqrt{\gamma_1\mathbf{1}^{\mathrm{T}}\widetilde{\mathbf{\Phi}}^{-1}\mathbf{e}_1}},\ldots,\frac{1}{\sqrt{\gamma_K\mathbf{1}^{\mathrm{T}}\widetilde{\mathbf{\Phi}}^{-1}\mathbf{e}_K}}\right]^{\mathrm{T}}. \tag{B.8}$$

On the other hand, μ can be obtained by plugging Eq. (B.7) into the first condition in Eq. (B.6d), i.e.,

$$\mu = M(\mathbf{1}^{\mathrm{T}}\widetilde{\mathbf{\Phi}}^{-1}\mathbf{b})^2 \tag{B.9}$$

and, by plugging Eq. (B.9) into Eq. (B.7), we obtain

$$w_k = \frac{\mathbf{e}_k^{\mathrm{T}}\widetilde{\mathbf{\Phi}}^{-1}\mathbf{b}}{M\mathbf{1}^{\mathrm{T}}\widetilde{\mathbf{\Phi}}^{-1}\mathbf{b}}, \quad \forall k \in \mathcal{K}. \tag{B.10}$$

Finally, choosing $\{w_k\}_{k\in\mathcal{K}}$ as in Eq. (B.10), μ as in Eq. (B.9), and $\Psi = \mathbf{0}$ readily satisfies Eq. (B.6b)–(B.6d), whereas Eq. (B.6a) yields

$$\sum_{k\in\mathcal{K}} (\mathbf{1}^{\mathrm{T}}\widetilde{\mathbf{\Phi}}^{-1}\mathbf{e}_k)\mathbf{a}_k\mathbf{a}_k^{\mathrm{H}} = \frac{1}{M}\mathbf{I}_M. \tag{B.11}$$

The latter is satisfied when $\widetilde{\mathbf{\Phi}} = M^2\mathbf{I}_K$, i.e., when $K = M$ and the steering angles of the UEs are such that $\mathbf{a}_k^{\mathrm{H}}\mathbf{a}_j = 0$, $\forall k \neq j$ (see, e.g., [92] for more details). In this setting, it follows from Eq. (B.10) that $w_k = 1/(M\sqrt{\gamma_k}\nu_{\mathcal{K}})$, from which we obtain the expression of the optimal transmit covariance in Eq. (6.25). □

Appendix C

Proof of Eq. (8.13)

Problem 11 is convex and thus the optimal solution solves the KKT conditions. Let the Lagrangian and its gradient as

$$\mathscr{L}(\boldsymbol{\theta},\boldsymbol{\mu},\nu) = \sum_k \|\boldsymbol{\theta}^{\mathrm{H}}\bar{\mathbf{H}}_k\mathbf{W}\|^2 - 2\sum_k \mathrm{Re}\{\boldsymbol{\theta}^{\mathrm{H}}\bar{\mathbf{H}}_k\mathbf{w}_k\} + \sum_{i=1}^{L}\mu_i(|\theta_i|^2-1) + \nu(\theta_{L+1}-1) \tag{C.1}$$

$$\nabla\mathscr{L}(\boldsymbol{\theta},\boldsymbol{\mu},\nu) = \sum_k \bar{\mathbf{H}}_k\mathbf{W}\mathbf{W}^{\mathrm{H}}\bar{\mathbf{H}}_k^{\mathrm{H}}\boldsymbol{\theta} - \sum_k \bar{\mathbf{H}}_k\mathbf{w}_k + \sum_{i=1}^{L}\mu_i\mathbf{e}_i\mathbf{e}_i^{\mathrm{T}}\boldsymbol{\theta} + \nu\mathbf{e}_{L+1} \tag{C.2}$$

respectively. Note that to find the derivative of the real part of $\boldsymbol{\theta}^{\mathrm{H}}\hat{\mathbf{H}}_k\mathbf{e}_k$ we have used again the property in Eq. (D.3). The KKT conditions of Problem 11 can be written as

$$\left(\sum_k \bar{\mathbf{H}}_k\mathbf{W}\mathbf{W}^{\mathrm{H}}\bar{\mathbf{H}}_k^{\mathrm{H}} + \mathrm{diag}(\boldsymbol{\mu})\right)\boldsymbol{\theta} = \left(\sum_k \bar{\mathbf{H}}_k\mathbf{w}_k - \nu\mathbf{e}_{L+1}\right) \tag{C.3}$$

$$|\theta_i|^2 \le 1 \quad i=1,\ldots,L; \quad \theta_{L+1}=1; \quad \boldsymbol{\mu}\ge\mathbf{0};$$

$$\mu_i(|\theta_i|^2-1) = 0 \quad i=1,\ldots,L \tag{C.4}$$

whose solution is given by

$$\boldsymbol{\theta} = \left(\sum_k \bar{\mathbf{H}}_k\mathbf{W}\mathbf{W}^{\mathrm{H}}\bar{\mathbf{H}}_k^{\mathrm{H}} + \mathrm{diag}(\boldsymbol{\mu})\right)^{-1}\left(\sum_k \bar{\mathbf{H}}_k\mathbf{w}_k - \nu\mathbf{e}_{L+1}\right), \tag{C.5}$$

with $\boldsymbol{\mu}\ge\mathbf{0}$ found in the following way

$$\begin{aligned} &\mu_i = 0 \text{ and } |\theta_i|^2 \le 1, \\ &\mu_i \ge 0 \text{ and } |\theta_i|^2 = 1, \quad \forall i = 1,\ldots,L. \end{aligned} \tag{C.6}$$

Lastly, ν is determined by forcing $\theta_{L+1} = 1$. Note that

$$\theta_{L+1} = \mathbf{e}_{L+1}^{\mathrm{T}} \boldsymbol{\theta} \tag{C.7}$$

$$= \mathbf{e}_{L+1}^{\mathrm{T}} \mathbf{B}\mathbf{r} - \nu\, \mathbf{e}_{L+1}^{\mathrm{T}} \mathbf{B}\mathbf{e}_{L+1} \tag{C.8}$$

where we have defined

$$\mathbf{B} = \left(\sum_k \bar{\mathbf{H}}_k \mathbf{W}\mathbf{W}^{\mathrm{H}} \bar{\mathbf{H}}_k^{\mathrm{H}} + \mathrm{diag}(\boldsymbol{\mu}) \right)^{-1}, \tag{C.9}$$

and $\mathbf{r} = \sum_k \bar{\mathbf{H}}_k \mathbf{w}_k$. Hence we have that

$$\nu = \frac{\mathbf{e}_{L+1}^{\mathrm{T}} \mathbf{B}\mathbf{z} - 1}{\mathbf{e}_{L+1}^{\mathrm{T}} \mathbf{B}\mathbf{e}_{L+1}}. \tag{C.10}$$

□

Appendix D

Proof of Eq. (8.19)

Problem 12 is convex and thus the optimal solution solves the KKT conditions. Let the Lagrangian and its gradient as

$$\mathscr{L}(\mathbf{W},\mu) = \|\bar{\mathbf{H}}^{\mathrm{H}}\mathbf{W}\|_{\mathrm{F}}^2 - 2\,\mathrm{tr}(\mathrm{Re}\{\bar{\mathbf{H}}^{\mathrm{H}}\mathbf{W}\}) + \mu(\|\mathbf{W}\|_{\mathrm{F}}^2 - P) \tag{D.1}$$

$$\nabla\mathscr{L}(\mathbf{W},\mu) = \bar{\mathbf{H}}\bar{\mathbf{H}}^{\mathrm{H}}\mathbf{W} - \bar{\mathbf{H}} + \mu\mathbf{W} \tag{D.2}$$

respectively. Note that to find the derivative of the real part of $\mathrm{tr}(\bar{\mathbf{H}}^{\mathrm{H}}\mathbf{W})$ we have used the following property, valid for any given scalar function $f(z)$ of complex variable z

$$\frac{df(z)}{dz} = \frac{1}{2}\left(\frac{\partial f(z)}{\partial \mathrm{Re}\{z\}} - j\frac{\partial f(z)}{\partial \mathrm{Im}\{z\}}\right). \tag{D.3}$$

The KKT conditions of Problem 12 can be written as the following

$$\begin{aligned} &(\bar{\mathbf{H}}\bar{\mathbf{H}}^{\mathrm{H}} + \mu\mathbf{I}_M)\mathbf{W} = \bar{\mathbf{H}}; \quad \|\mathbf{W}\|_{\mathrm{F}}^2 \le P; \quad \mu \ge 0; \\ &\mu(\|\mathbf{W}\|_{\mathrm{F}}^2 - P) = 0; \end{aligned} \tag{D.4}$$

whose solution is given by $\mathbf{W} = (\bar{\mathbf{H}}\bar{\mathbf{H}}^{\mathrm{H}} + \mu\mathbf{I}_M)^{-1}\bar{\mathbf{H}}$, with $\mu \ge 0$ chosen such that $\|\mathbf{W}\|_{\mathrm{F}}^2 = P$ (e.g., by bisection). □

List of Publications

The research carried out during this reporting period has lead to the publication of the following scientific papers:

Journal papers

1. [90] P. Mursia, V. Sciancalepore, A. Garcia-Saavedra, L. Cottatellucci, X. Costa-Perez, and D. Gesbert, "RISMA: Reconfigurable Intelligent Surfaces Enabling Beamforming for IoT Massive Access," *IEEE J. Sel. Areas Commun. (JSAC)*, vol. 8716, no. c, pp. 1–1, 2020

2. [89] P. Mursia, I. Atzeni, M. Kobayashi, and D. Gesbert, "D2D-Aided Multi-Antenna Multicasting under Generalized CSIT," 2021, submitted to *IEEE Trans. Wireless Commun. (TWC)* [Online]. Available: https://arxiv.org/abs/2102.01624

3. [86] P. Mursia, I. Atzeni, D. Gesbert, and L. Cottatellucci, "Enforcing Statistical Orthogonality in Massive MIMO Systems via Covariance Shaping," 2021, submitted to *IEEE Trans. Wireless Commun. (TWC)* [Online]. Available: https://arxiv.org/abs/2106.07952

Conference papers

1. [20] P. Mursia, I. Atzeni, D. Gesbert, and L. Cottatellucci, "Covariance Shaping for Massive MIMO Systems," in *Proc. IEEE Global Commun. Conf. (GLOBECOM)*, Abu Dhabi, UAE, 2018

2. [21] P. Mursia, I. Atzeni, D. Gesbert, and L. Cottatellucci, "On the Performance of Covariance Shaping in Massive MIMO Systems," in *Proc. IEEE Int. Workshop Computer-Aided Modeling and Design of Commun. Links and Netw. (CAMAD)*, Barcelona, Spain, 2018

3. [87] P. Mursia, I. Atzeni, D. Gesbert, and M. Kobayashi, "D2D-Aided Multi-Antenna Multicasting," in *Proc. IEEE Int. Conf. Commun. (ICC)*, Shanghai, China, 2019, **best paper award.**

4. [88] P. Mursia, I. Atzeni, M. Kobayashi, and D. Gesbert, "D2D-Aided Multi-Antenna Multicasting in a Dense Network," in *Proc. Asilomar Conf. Signals, Syst., and Comput. (ASILOMAR)*, Pacific Grove, USA, 2019

Résumé [Français]

Les réseaux de cinquième génération (5G) et aprés se démarqueront des déploiements de quatrième génération (4G) précédents de plusieurs manières importantes [1]: (i) la nécessité de fournir un trafic à très haut débit à une population dense d'internautes très exigeants; (ii) l'hétérogénéité des appareils qui téléchargeront/chargeront des données depuis/vers le réseau, des tablettes et téléphones classiques contrôlés par l'homme, aux objets connectés utilisés pour les villes intelligentes et les usines intelligentes, et aux véhicules connectés des prochains réseaux de transport intelligents (ITN); (iii) l'hétérogénéité des mesures de performance par lesquelles la satisfaction sera mesurée par les opérateurs de réseau et sur ces divers appareils, c'est-à-dire du débit de données maximal à la latence, à la fiabilité et à la consommation d'énergie. Ces départs combinés des réseaux 4G motivent une refonte des mécanismes de traitement du signal et de codage de l'information afin d'offrir les performances et l'adaptabilité requises.

Dans cette thèse, nous considérons un scénario aprés-5G dans lequel un grand nombre d'equipements utilisateur (UEs) hétérogènes accèdent simultanément au réseau, noté *accès massif*, et nous relevons le défi de concevoir un roman méthodes multi-antennes pour faire face aux défis techniques qui en résultent et pour atteindre les demandes sans précédent associées en termes de performances du réseau [2,3].

9.1 Massive MIMO

Parmi les technologies candidates, les sorties multiples massives à entrées multiples (massive MIMO) jouent un rôle central dans les déploiements 5G [1, 4, 5] actuels et devraient également conserver ce rôle dans les futurs réseaux sans fil 5G [6–9]. En effet, grâce à son grand nombre d'antennes, le masssive MIMO est capable de desservir plusieurs UEs dans les mêmes ressources temps-fréquence et peut augmenter leur puissance utile reçue d'un facteur qui évolue linéairement avec le nombre des antennes disponibles. Ceci est réalisé grâce à la formation de faisceaux hautement directionnelle, qui résulte de la combinaison cohérente des signaux d'émission au niveau du réseau massif. Cependant, alors que les promesses de le massive MIMO sont nombreuses et bien étudiées, certains défis restent à

résoudre [5]. En particulier, les le massive MIMO présentent des problèmes d'évolutivité dans les scénarios d'accès massifs en raison du grand nombre des UEs à servir. En effet, la transmission cohérente des signaux nécessite la disponibilité de l'informations sur l'état du canal à l'émetteur (CSIT), ce qui pose plusieurs défis en termes de conception de système dans des scénarios d'accès massif. Les informations sur l'état du canal (CSI) sont nécessaires pour atteindre les avantages mentionnés ci-dessus des le massive MIMO, mais implique également une complexité accrue de la mise en œuvre des précodeurs/décodeurs et une plus grande surcharge liée à la formation assistée par le pilote et au retour de le CSI en tant que nombre des antennes et UEs grandit.

Plus précisément, la dimensionnalité élevée du canal nécessite l'allocation de ressources de communication considérables pour l'acquisition de le CSI assistée par pilote et les opérations de grande matrice. Dans les systèmes de division de fréquence (FDD), le CSI est obtenu au moyen d'une transmission pilote de liaison descendante de la station base (BS) aux UEs. Dans ce cas, la quantité de ressources de communication requise pour l'estimation de canal dans la liaison descendante est mise à l'échelle avec le nombre d'antennes M, ce qui entraîne un surcoût à mesure que M augmente [10]. En revanche, dans les systèmes de la division des temps (TDD), le CSI est acquis au moyen d'une transmission pilote de liaison montante depuis les UEs vers la BS, et les estimations de canal de liaison montante sont ensuite utilisées également dans la liaison descendante grâce à la réciprocité des canaux. Ainsi, la quantité de ressources de communication requises évolue avec le nombre des UEs K. Cependant, comme le temps de cohérence du canal est limité, les mêmes séquences pilotes doivent être réutilisées à travers différents UEs, générant ainsi une contamination pilote qui réduit considérablement la qualité de le CSI [11, 12]. En conséquence, le canal des UEs interférents qui partagent la même séquence pilote devient corrélé, ce qui pose une limitation fondamentale sur l'efficacité spectrale (SE) réalisables. Néanmoins, il est montré dans [13] que, lors de l'utilisation du précodage multi-cellules d'erreur quadratique moyenne minimale (MMSE), le SE réalisable de massive MIMO n'est pas limité par la contamination du pilote à mesure que M grandit grande. Cependant, ce type de précodage nécessite un partage de le CSI complet entre toutes les cellules, ce qui augmente considérablement la surcharge de signalisation globale.

9.1.1 Le rôle des informations statistiques sur le canal

Pour contrer ces problèmes, plusieurs travaux importants ont proposé d'utiliser des CSI statistiques dans le régime massive MIMO [14–26]. En particulier, ces informations sont représentées par la matrice de covariance de canal, qui caractérise l'ensemble des directions de canal statistiques et des gains de puissance de canal moyens associés. De telles propriétés statistiques du canal massive MIMO sont essentiellement dictées par l'étalement de l'angle parcouru par les angles d'arrivée (AoAs) de la propagation par trajets multiples des signaux qui frappent le tableau massif. La dispersion angulaire du AoAs est souvent limitée en raison de la

haute résolution spatiale du tableau massif par rapport à l'environnement de diffusion limité. En conséquence, les matrices de covariance de canal dans le massive MIMO ont tendance à être de bas rang et dominées par quelques directions de canal majeures [13, 15, 18, 19]. Cette propriété particulière peut être exploitée pour plusieurs applications telles que la réduction du surdébit de rétroaction dans la phase d'estimation de canal et l'atténuation des interférences dans la phase de transmission de données de liaison descendante. Comme le montre [19], cela est possible si les UEs interférents qui sont suffisamment éloignés présentent des sous-espaces de signaux non chevauchants ou orthogonaux. De plus, dans [15], les auteurs montrent la dépendance de la richesse du sous-espace du signal associé à chaque UE sur le rayon de diffusion autour de l'UE.

A cet égard, plusieurs travaux ont étudié le problème du précodage hybride où la formation de faisceau appliquée à la BS est divisée en un précodeur interne et externe [16–18, 23]. Le précodeur interne est basé sur le CSI instantané local tandis que le précodeur externe ne dépend que des statistiques de canal du second ordre. Une telle approche aboutit à une réduction du nombre de symboles pilotes requis pour l'acquisition de le CSI, comme indiqué dans [23]. De plus, dans le contexte des systèmes FDD où le problème de surcoût d'acquisition de CSI est encore plus prononcé, les auteurs de [16] ont proposé d'utiliser un tel schéma de précodage hybride afin de réduire la taille de les vecteurs de CSI efficaces résultants en exploitant la quasi-orthogonalité des étalements angulaires des canaux pour différents groupes UE. La matrice de formation de faisceau interne est ensuite calculée sur la base des canaux instantanés effectifs réduits des UEs. Dans [18], cette approche n'entraîne aucune perte par rapport au cas CSIT complet lorsque le nombre d'antennes au niveau de la BS augmente. De plus, dans [17], les auteurs montrent qu'une telle mise à l'échelle est également obtenue dans le cas d'un nombre fini d'antennes au niveau de la BS en employant une planification d'UE appropriée.

Dans les systèmes TDD, les travaux existants ont montré comment la BS peut discriminer les UEs interférents basés uniquement sur des informations statistiques de canal, même en présence de contamination pilote, offrant ainsi la possibilité de réutiliser des pilotes à travers multiples UEs [14, 19, 22, 26]. Dans [14], une réutilisation pilote pour une transmission massive MIMO sur des canaux à évanouissements de Rayleigh spatialement corrélés est proposée comme un moyen de réduire le surcoût pour l'estimation de canal. En effet, la somme d'erreur quadratique moyenne (MSE) des estimations de canal peut être minimisée à condition que les intervalles des AoAs des UEs réutilisant les pilotes ne se chevauchent pas, entraînant ainsi une décontamination du pilote. Dans [22], les statistiques de second ordre du canal sont utilisées pour précoder les signaux pilotes. Cette méthode réduit la variance de l'erreur d'estimation de canal d'un facteur proportionnel au nombre d'antennes au niveau des UEs et offre donc la possibilité de réutiliser des pilotes. Une méthode robuste d'estimation de canal est étudiée dans [26] en exploitant la diversité de chemin dans le domaine angulaire, faisant ainsi face à

des scénarios dans lesquels les canaux interférents peuvent chevaucher les canaux désirés en termes des AoAs des trajets multiples du canal.

Les statistiques CSI peuvent également être utilisées dans la conception de précodeurs pour atténuer les interférences dans la phase de transmission de données de liaison descendante [24, 25]. Grâce à la disponibilité des matrices de covariance de canal, la BS peut précoder le signal de telle sorte que les chemins de propagation choisis n'interfèrent pas en moyenne. Les auteurs de [24] proposent de maximiser une borne inférieure sur le débit de somme ergodique d'un paramètre à deux-UE où les UEs sont équipés d'une seule antenne. Dans [25], les auteurs conçoivent un émetteur-récepteur robuste basé sur une borne inférieure de la matrice MSE moyenne sous différentes conditions CSI.

Cependant, les performances des schémas ci-dessus reposent sur la structure de la matrice de covariance de canal des UEs en termes de rang et de degré de séparation par rapport aux sous-espaces de signal des autres UEs. Ces propriétés sont dictées par l'environnement de diffusion physique et *sont généralement hors du contrôle du concepteur*. Par conséquent, la condition des sous-espaces de signaux non chevauchants ou orthogonaux est rarement satisfaite en pratique, alors que dans de nombreux scénarios pratiques, tels que celui représenté sur la Fig. 9.1, les UEs présentent corrélation statistique élevée [13]. De plus, les travaux existants supposent souvent le modèle de canal dit de Kronecker en raison de sa structure analytique simple. Cependant, un tel modèle s'est avéré être une simplification excessive de la vraie nature du canal sans fil [27]. Comment utiliser les informations statistiques de canal pour la réduction de la surcharge d'acquisition de le CSI et l'atténuation des interférences sous l'hypothèse de modèles de canaux plus réalistes est le principal sujet de discussion dans la Partie II de cette thèse.

9.2 Communications D2D

En parallèle, les communications appareil à appareil (D2D) ont récemment pris de l'ampleur en raison des applications émergentes dans les systèmes sans fil 5G tels que le multicast, la communication de machine à machine et le déchargement cellulaire [28, 29], et devraient être inclus dans les prochains déploiements 5G en tant que nouveau paradigme pour améliorer les performances du réseau [1, 2, 30]. En effet, les communications D2D peuvent être utilisées comme une approche alternative pour faire face à des scénarios d'accès massifs en permettant aux UEs à proximité d'établir une communication directe. Ainsi, en remplaçant une liaison radio relativement longue via la BS, qui est sévèrement limitée par le pathloss, par deux communications directes plus courtes permet de réduire la consommation d'énergie et la latence, et d'obtenir des débits de données plus élevés.

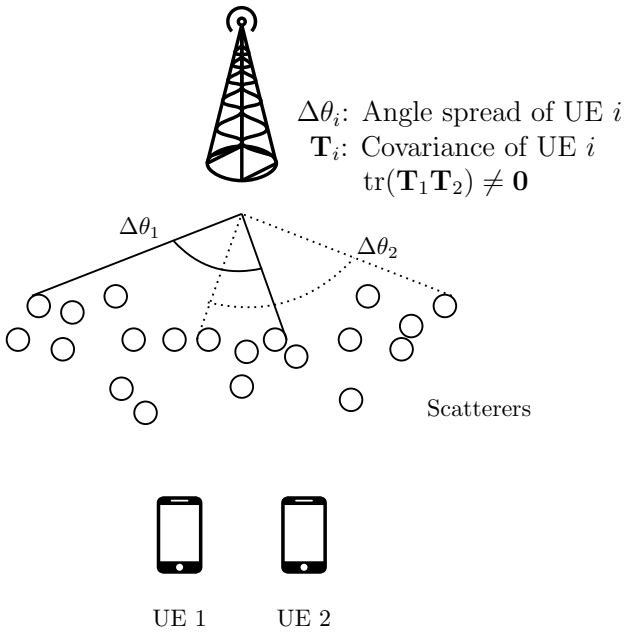

Figure 9.1 – La matrice de covariance de canal est essentiellement dictée par l'étalement de l'angle parcouru par les AoAs de la propagation par trajets multiples des signaux. Dans de nombreux scénarios réalistes, les écarts d'angle des UEs interférents se chevauchent.

9.2.1 Communications multicast: quand la fiabilité du service devient un facteur limitant

Dans cette thèse, nous considérons l'application des communications D2D dans le contexte des communications multicast dans lesquelles un émetteur souhaite transmettre un message commun à plusieurs récepteurs. Un tel scénario se présente naturellement dans de nombreux réseaux sans fil [31–36]. Plus précisément, les services de multicast sont pertinents pour de nombreuses applications complexes allant de la mise en cache périphérique sans fil, où les contenus populaires sont mis en cache pendant les heures creuses et ensuite distribués via la multicast [37, 38], à la diffusion de messages critiques dans les réseaux de véhicules [39]. Cependant, il est bien connu que la multicast sur des canaux sans fil est entravée par l'effet *worst-user-kills-all*, par lequel la capacité de multicast disparaît lorsque le nombre des UEs K augmente pour un nombre fixe des antennes à la BS [31, 32]. En fait, comme le message transmis par la BS doit être décodé par tous les UEs, la capacité de multicast est limitée par les UEs avec le plus petit gain d'évanouissement et ce dernier a tendance à diminuer avec la dimension du système. En particulier, pour le cas de évanouissant du canal i.i.d. Rayleigh, la capacité de multicast disparaît rapidement car elle évolue inversement proportionnellement à K [31]. Notez que ce problème ne peut pas être résolu fondamentalement en ajoutant simplement plus d'antennes aux émetteurs/récepteurs.

Pour surmonter ce problème, différentes approches ont été considérées dans la littérature (par

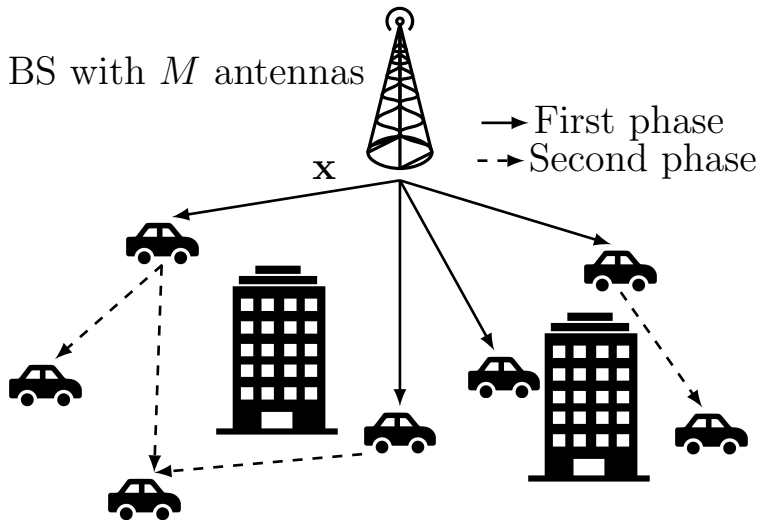

Figure 9.2 – Multicast coopérative à deux phases assistée par D2D. Au cours de la première phase, la BS envoie le message commun x via la multicast conventionnelle à un ensemble de relais, qui à leur tour retransmettent le message dans la deuxième phase via les liens D2D au reste du réseau.

exemple, [15, 31, 33–36, 40–44, 46]), qui peuvent être grossièrement classées en trois groupes. Dans le premier groupe, un sous-ensemble des UEs dans de bonnes conditions de canal est sélectionné pour être servi, tandis que les UEs dans de mauvaises conditions de canal sont négligés [40, 41]. Cependant, non seulement une telle approche aboutit à une couverture réseau limitée, mais elle implique également la résolution d'un problème combinatoire pour trouver le meilleur sous-ensemble des UEs. Le second groupe exploite plusieurs antennes au niveau de l'émetteur et le durcissement de canal résultant pour atténuer la variance de la puissance du signal reçu individuel lorsque le nombre des UEs augmente [31, 42]. Cependant, une telle approche est basée sur l'hypothèse d'évanouit du canal i.i.d. Rayleigh et exige que le nombre d'antennes à la BS croisse au moins comme $\log(K)$. Enfin, le troisième groupe s'appuie sur la coopération entre les UEs activée par les liens D2D.

9.2.2 D2D-assistée multicast

Dans le scénario de multicast susmentionné, les communications D2D entre les UEs peuvent être exploitées pour surmonter le comportement de disparition de la capacité de multicast en divisant le temps de transmission total en deux phases. Ici, la multicast conventionnelle se produit uniquement dans la première phase, où la BS transmet à un débit tel que le message commun est reçu par un sous-ensemble des UEs dans des conditions de canal favorables. Ensuite, ces UEs agissent comme des relais opportunistes et retransmettent en coopération le message dans la deuxième phase. Cette approche, qui est représentée sur la Fig. 9.2, a

été largement étudiée dans la littérature sous des hypothèses de CSIT spécifiques et en se concentrant sur le cas simple de l'émetteur à une seule antenne [15, 33–36, 43, 44, 46], comme détaillé ci-après.

L'analyse théorique de la multicast coopérative à deux phases peut être trouvée dans [33–35, 43, 46]. Plus spécifiquement, [33] a établi la capacité de multicast en utilisant un schéma coopératif à deux phases pour un réseau simple avec des canaux à évanouissement i.i.d. Rayleigh. La mise à l'échelle de la multicast a été analysée dans [34] pour deux modèles de réseau différents, où la capacité de multicast s'est avérée augmenter de $\log(\log(K))$ dans le cas d'un réseau dense (c'est-à-dire, un scénario dans lequel le nombre de récepteurs augmente sur une zone de réseau fixe) avec des canaux spatialement i.i.d. Récemment, [46] a caractérisé la mise à l'échelle de la multicast pour une topologie de réseau plus générale (capturant la perte de chemin) et a montré qu'avec des statistiques de CSIT, le débit de multicast moyen augmente de $\log(\log(K))$. Une analyse similaire peut être trouvée dans [35] pour les réseaux métropolitains sans fil IEEE 802.16. De plus, [43] a caractérisé le débit de multicast réalisable d'un schéma interactif basé sur des liaisons de coopération en duplex intégral et non orthogonales. Un autre schéma en deux phases a été présenté dans [36], qui visait à minimiser la consommation électrique totale tout en garantissant une certaine couverture sous le CSIT parfait. D'autre part, [44] a considéré une structure de message multicast à deux couches avec une partie à haute priorité, à faible débit et une partie à faible priorité à haut débit, de sorte que les UEs qui sont capables de décoder l'ensemble du message aident les autres en agissant comme des relais opportunistes. L'allocation des temps entre les deux phases a été étudiée dans [15], qui a montré que plus de temps devrait être consacré à la deuxième phase à mesure que les UEs s'éloigne de la BS. Enfin, un schéma coopératif biphasé similaire avec plusieurs antennes au niveau de la BS a été proposé dans [47] dans le contexte de la diffusion sous le CSIT parfait. En exploitant la division de débit, ce schéma forme un message virtuel commun à multidiffuser dans la première phase et retransmis via un relais opportuniste dans la deuxième phase.

En résumé, les travaux existants ont démontré les avantages des schémas coopératifs à deux phases soit pour des configurations de CSIT spécifiques, soit pour le cas simple de la BS à une seule antenne. Cela nous motive à étudier la multicast coopérative à deux phases en exploitant plusieurs antennes à la BS, *qui change radicalement la nature du problème*, et à considérer diverses configurations de CSIT allant de CSIT parfaites à le CSIT topologique (où seule la carte de la zone du réseau et la distribution des UEs sont disponibles à la BS). Cette discussion est détaillée dans la Partie III de cette thèse.

9.3 Communications MmWave

Ces dernières années, la nécessité de faire face à des scénarios d'accès massifs a également conduit à l'étude de bandes de fréquences plus élevées comme moyen de garantir la connectivité à un grand nombre d'appareils de l'internet des objets (IoT). À cet égard, les onde millimétrique (mmWave) joue un rôle clé dans la réalisation des promesses de la 5G et continuera de le faire dans les réseaux aprés-5G [9, 48]. En effet, l'avènement des applications IoT massives générant un énorme volume d'appareils pose mmWave comme une solution candidate pour de nombreuses applications telles que les réseaux intelligents, les villes intelligentes et les industries intelligentes [49]. Cependant, mmWave contraste avec la nature de faible puissance des périphériques IoT qui ne sont pas capables par eux-mêmes de contrecarrer les environnements de propagation difficiles dans ces bandes de fréquences élevées. Le principal défi dans ce cas est que les émetteurs/récepteurs mmWave utilisent généralement plusieurs chaînes de fréquence radio (RF) et un grand nombre d'antennes pour lutter contre l'atténuation de perte de chemin élevée susmentionnée. Cette stratégie contraste avec les dispositifs IoT à énergie contrainte, car l'intégration de plusieurs composants actifs drainant de l'énergie devient irréalisable [50].

9.3.1 Réseaux assistés par RIS

Dans le contexte des communications mmWave, les surfaces intelligentes reconfigurables (RISs) attirent beaucoup d'attention en raison des progrès récents des métamatériaux, ce qui rend leur construction et leur installation en milieu urbain [51]. [1] Une RIS est une surface réfléchissante qui peut être commodément modélisée comme un réseau discret d'antennes passives, dont chacune peut introduire un déphasage plus une atténuation d'amplitude dans le signal. Une optimisation appropriée de tous ces éléments d'antenne équivalents conduit à une combinaison cohérente de tous les trajets déphasés et atténués du signal entrant. Il en résulte un faisceau très étroit et directif, qui peut améliorer la qualité du signal reçu à l'UE destinataire [52]. Une telle optimisation est généralement effectuée par une entité centrale du réseau qui informe ensuite la RIS [53]. Cette dernière est donc une structure entièrement passive dont le seul composant actif est le contrôleur de la RIS, qui produit de petites variations de la tension d'entrée sur chaque élément de la RIS qui se traduisent par un déphasage ajouté au signal entrant. Par conséquent, les RISs peuvent finalement transformer la nature incontrôlable de l'environnement de propagation en un support programmable en neutralisant efficacement l'atténuation de la perte de chemin et les effets d'évanouissement.

[1] Notez que le terme *surface intelligent reflétant* (IRS) est également utilisé dans d'autres travaux connexes. Les acronymes IRS et RIS peuvent être utilisés de manière interchangeable car ils désignent le même dispositif physique, c'est-à-dire une surface réfléchissante qui peut être contrôlée par une entité du réseau. Pour éviter toute ambiguïté, nous avons choisi d'utiliser dans cette thèse le terme RIS.

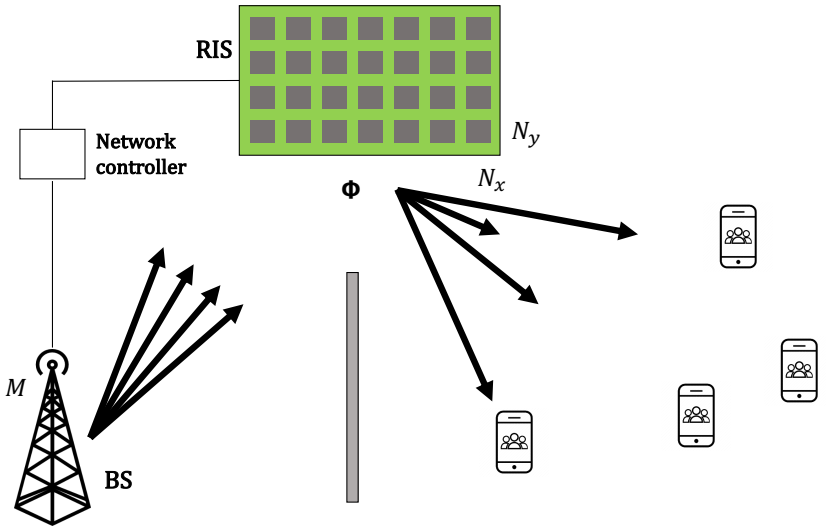

Figure 9.3 – Exemple de réseau assisté par une RIS avec le chemin ligne de mire (LoS) obstrué, où $\mathbf{\Phi}$, N_X et N_y sont la matrice contenant les déphasages induits, et le nombre des éléments de la RIS sur les axes x et y, respectivement.

Grâce à l'utilisation des RISs, il est alors possible d'exploiter la grande quantité de spectre disponible aux fréquences mmWave et d'augmenter considérablement les débits de données de pointe. Conceptuellement, la RIS peut rappeler certains des défis derrière les méthodes de relais *amplifier et avancer (AF)* conventionnelles [54] et les méthodes de formation de faisceaux utilisées dans le (massive) MIMO [55]. Cependant, il existe une différence marquée entre les relais AF conventionnels et les RISs [56, 57]. En effet, les premiers reposent sur des amplificateurs de puissance actifs (consommateurs d'énergie) à faible bruit et d'autres composants électroniques actifs, tels que les convertisseurs, mélangeurs et filtres numérique-analogique (DAC) ou analogique-numérique (ADC). En revanche, les RISs ont une empreinte matérielle très faible, consistant en une ou quelques couches de structures planes qui peuvent être construites en utilisant des méthodes de lithographie ou de nano-impression. Par conséquent, les RISs sont particulièrement intéressants pour une intégration transparente dans les murs, les plafonds, les boîtiers d'objets, les verres de construction ou même les vêtements [58]. D'un autre côté, la technologie massive MIMO et les RISs peuvent produire des gains de rapport signal sur bruit (SNR) similaires. [2] Cependant, une RIS réalise de tels gains de formation de faisceaux de manière quasi passive puisque seule une entrée de puissance (négligeable) est nécessaire pour le contrôleur de la RIS , présentant ainsi une efficacité énergétique élevée.

[2] Bien qu'il ait été montré que l'SNR évolue linéairement avec le nombre de antennes en utilisant le massive MIMO et proportionnelles au carré du nombre d'éléments d'antenne équivalents avec les RISs, le manque d'amplification de puissance dans cette dernière technologie détermine une perte de performance telle que, globalement, les deux technologies produisent des gains d'SNR similaires dans les mêmes conditions [55].

En raison des avantages décrits précédemment, les RISs gagnent en fait beaucoup d'élan dans les scénarios d'accès massifs [52, 59–73] en raison de leur capacité susmentionnée à transformer la nature stochastique de l'environnement sans fil en un canal programmable. Les RISs ont été récemment proposés pour une variété d'applications, y compris les communications sécurisées [67, 68], l'accès multiple non orthogonal [69], le calcul en direct [70], ou des réseaux cellulaires écoénergétiques [71, 72].

Si la modélisation théorique des réseaux sans fil assistés par les RISs est bien étudiée, de nombreux défis restent à relever, comme la construction de bancs d'essai pour la validation expérimentale [74–77], la tâche d'estimer le canal combiné à partir de la BS à la RIS et à l'UE [78, 79], et l'optimisation conjointe de la BS multi-antenne et des paramètres de la RIS [79–85]. Cette dernière catégorie est particulièrement pertinente pour cette thèse, concernant l'optimisation conjointe de la formation de faisceau active à la BS et de la formation de faisceau passive à la RIS. Dans [80], les auteurs ont analysé le cas d'un seul UE et proposent de maximiser le débit. Le problème d'optimisation non convexe qui en résulte est résolu à la fois via une itération en virgule fixe et une optimisation multiple. Un paramètre similaire est analysé dans [79], où les auteurs proposent une solution heuristique à la maximisation non convexe de la puissance du signal reçu avec des performances similaires à la relaxation semi-définie (SDR) classiques. Le paramètre d'un UE seul est également étudié dans [84], où les auteurs proposent d'encoder des informations à la fois dans le signal transmis et dans la configuration de la RIS. Un paramètre multi-utilisateur est analysé dans [81] où les auteurs proposent de maximiser le minimum des SNR réçu parmi tous les UEs dans le régime du grand système. Bien que cette approche garantisse l'équité entre les UEs, elle pourrait ne pas maximiser le débit de somme du système. Dans [82], les auteurs conçoivent conjointement la formation de faisceaux à la BS et les paramètres de la RIS en minimisant la puissance d'émission totale au niveau de la BS, étant donné une exigence de réception minimale du rapport du signal sur interférences plus bruit (SINR). Ce cadre a ensuite été étendu pour prendre en compte les RISs à basse résolution dans le cas d'un seul UE [83].

Dans cette thèse, nous considérons un réseau assisté par une RIS comme celui représenté sur la Fig. 9.3 et nous affirmons que la formation de faisceau active via un réseau d'antennes côté émetteur et la formation de faisceau passive dans le canal via une RIS *peuvent se compléter* et fournir des gains encore plus importants lorsqu'ils sont optimisés conjointement. En particulier, nous introduisons un nouveau cadre mathématique pour minimiser le erreur quadratique moyenne somme (SMSE) des systèmes de communication à formation de faisceaux assistés par une RIS, qui convient à un accès sans fil massif IoT. Cette approche, qui à notre connaissance n'a pas été explorée auparavant, nous permet de construire des algorithmes efficaces qui maximisent les performances du débit de somme. En effet, notre fonction objectif est volontairement choisie de telle sorte que nous puissions en déduire un mécanisme qui apporte des solutions performantes tout en garantissant efficacité et évolutiv-

ité. Ce concept est détaillé dans la Partie IV de cette thèse.

9.4 Aperçu de la Thèse et Principales Contributions

Dans cette section, nous donnons un bref aperçu de cette thèse en mettant en évidence les concepts clés et les contributions détaillées dans chacune de ses sections. Plus précisément, cette thèse est divisée en cinq parties, qui sont brièvement décrites ci-dessous.

Part I: Motivation and System Model. Cette partie est divisée en deux chapitres. Le Chapitre 1 décrit la motivation derrière notre travail en mettant en lumière les défis et les limites de l'état de l'art sur les technologies multi-antennes dans les réseaux sans fil au-delà de la 5G. Le Chapitre 2 décrit le modèle de système du scénario d'accès massif considéré. En particulier, nous décrivons un tel scénario dans son cas le plus général en fournissant des définitions clés, des hypothèses et des mesures de performance qui seront utilisées tout au long de cette thèse. Dans les parties suivantes, nous détaillerons le réglage ci-dessus afin de mieux se concentrer sur différents aspects de conception spécifiques.

Part II: Covariance Shaping. Dans le Chapitre 3, nous introduisons le concept de *covariance shaping*, qui consiste à modifier convenablement les statistiques de canal perçues par la BS au moyen de la formation de faisceaux statistique du côté de l'UE pour imposer une orthogonalité partielle ou totale entre les transmissions interférentes dans l'espace. Cette méthode est basée uniquement sur les propriétés statistiques du canal et peut être utilisée à la fois pour la réduction de la surcharge et de la complexité des opérations matricielles dans l'acquisition de le CSI, respectivement, et pour l'atténuation des interférences. Par rapport aux travaux existants qui supposent de manière irréaliste l'orthogonalité statistique comme une propriété donnée par l'environnement de diffusion physique, covariance shaping exploite les propriétés de sélectivité spatiale des UEs lorsque ces derniers sont équipés d'au moins deux antennes pour appliquer une telle propriété dans n'importe quel scénario physique donné. De plus, covariance shaping suppose un modèle de canal général qui va au-delà de la structure de Kronecker communément admise. En effet, alors que le modèle de canal de Kronecker est largement répandu en raison de sa formulation analytique simple et de sa traitabilité, il ne permet pas aux UEs de modifier la statique du canal perçue par la BS. À cet égard, nous transformons un modèle de canal généralement peu pratique mais plus réaliste en un avantage. Dans le Chapitre 4, cette méthode est d'abord étudiée dans le cas simple de deux UEs afin de mettre en évidence ses caractéristiques clés et elle est ensuite étendue à un nombre général des UEs. De plus, nous dérivons le débit de somme réalisable sous covariance shaping, ce qui expose davantage les effets de la méthode proposée sur les performances du réseau. Ces résultats ont été publiés dans les articles suivants.

[21] P. Mursia, I. Atzeni, D. Gesbert, and L. Cottatellucci, "On the Performance of Covariance

Shaping in Massive MIMO Systems," in *Proc. IEEE Int. Workshop Computer-Aided Modeling and Design of Commun. Links and Netw. (CAMAD)*, Barcelona, Spain, 2018

[20] P. Mursia, I. Atzeni, D. Gesbert, and L. Cottatellucci, "Covariance Shaping for Massive MIMO Systems," in *Proc. IEEE Global Commun. Conf. (GLOBECOM)*, Abu Dhabi, UAE, 2018

[86] P. Mursia, I. Atzeni, D. Gesbert, and L. Cottatellucci, "Enforcing Statistical Orthogonality in Massive MIMO Systems via Covariance Shaping," 2021, submitted to *IEEE Trans. Wireless Commun. (TWC)* [Online]. Available: https://arxiv.org/abs/2106.07952

Part III: D2D-Aided Multi-Antenna Multicasting. Dans cette partie, nous considérons un schéma de multicast en deux phases coopératif en présence de plusieurs antennes à la BS. En dotant la BS de capacités de précodage, le problème de la conception d'un schéma multicast coopératif capitalisant sur les communications D2D change radicalement de nature. En effet, il nécessite d'optimiser conjointement la stratégie de précodage et le débit multicast afin de maximiser les performances du système. A notre connaissance, ce scénario n'a pas été envisagé jusqu'à présent dans les ouvrages existants. Dans le Chapitre 5, nous décrivons le modèle de système considéré et les métriques d'optimisation. Plus précisément, nous utilisons la notion de *débit de multicast moyen* et de *débit de multicast de panne* comme métriques de performances, qui correspondent au débit de multicast maximal sous des contraintes de panne moyenne et conjointe sur les débits réalisables de les UEs, respectivement. De telles contraintes sont spécifiées par une *panne cible*, qui permet d'éviter de gaspiller des ressources de communication utiles pour servir un petit pourcentage des UEs qui pourrait être dans des conditions de canal particulièrement défavorables. De plus, différemment des travaux précédents, nous considérons diverses configurations de CSIT et proposons trois algorithmes notés: (i) D2D-MAM, qui est applicable dans le cas de CSIT parfaits; (ii) D2D-SMAM, qui est conçu pour rendre compte de la disponibilité des statistiques de CSIT à long terme, et (iii) D2D-TMAM, qui suppose seulement des CSIT grossiers tels que la carte du réseau et le pdf des UEs dans l'espace. Les méthodes proposées, qui sont détaillées dans le Chapitre 6, exploitent les capacités de précodage au niveau de la BS pour cibler des UEs spécifiques qui peuvent effectivement servir de D2D relaie vers les UEs restant, et maximise le débit de multicast sous la contrainte de panne spécifiée et la configuration de CSIT. Dans tous les cas considérés, les algorithmes proposés surmontent le comportement de goulot d'étranglement dû au pire UE de la multicast multi-antenne monophasée conventionnelle et transforment une grande population d'UEs en un avantage pour le débit de multicast réalisable. Ces résultats ont conduit aux publications suivantes.

[87] P. Mursia, I. Atzeni, D. Gesbert, and M. Kobayashi, "D2D-Aided Multi-Antenna Multicasting," in *Proc. IEEE Int. Conf. Commun. (ICC)*, Shanghai, China, 2019, **best paper award.**

[88] P. Mursia, I. Atzeni, M. Kobayashi, and D. Gesbert, "D2D-Aided Multi-Antenna Multicasting

in a Dense Network," in *Proc. Asilomar Conf. Signals, Syst., and Comput. (ASILOMAR)*, Pacific Grove, USA, 2019

[89] P. Mursia, I. Atzeni, M. Kobayashi, and D. Gesbert, "D2D-Aided Multi-Antenna Multicasting under Generalized CSIT," 2021, submitted to *IEEE Trans. Wireless Commun. (TWC)* [Online]. Available: https://arxiv.org/abs/2102.01624

Part IV: Reconfigurable Intelligent Surfaces. Dans le Chapitre 7, nous discutons de l'intégration de la technologie RIS récemment introduite dans les systèmes MIMO existants comme moyen d'améliorer les performances du réseau dans des scénarios d'accès massif. Plus précisément, nous proposons un algorithme d'optimisation alternée multi-UE assistée par RIS, noté RISMA, qui optimise conjointement la stratégie de formation de faisceaux (active) à la BS et au déphasages (passif) à la RIS. Par rapport aux travaux existants, RISMA a l'avantage unique d'un cadre d'optimisation simple et efficace, qui résulte du choix de l'SMSE comme métrique d'optimisation. Ce choix joue un rôle clé dans la détermination de la complexité associée de la procédure d'optimisation et des performances du réseau qui en résultent. En effet, comme décrit dans le Chapitre 8, l'SMSE nous permet d'obtenir un problème convexe dans les deux variables d'optimisation séparément. Plus précisément, lors de l'utilisation d'une optimisation alternée entre le vecteur de formation de faisceaux à la BS et les déphasages à la RIS, les sous-problèmes résultants sont résolus sous forme fermée, ce qui entraîne une évolutivité et une efficacité de la conception sans la nécessité de définir tout paramètre système. De plus, nous adaptons RISMA, qui fournit une solution d'un point de vue théorique, pour tenir compte des contraintes pratiques lors de l'utilisation des RISs à basse résolution comprenant des éléments d'antenne qui peuvent être activés de manière binaire. En particulier, un tel RIS ne supporte que les valeurs de déphasage d'un ensemble discret, plutôt que toute valeur réelle d'une plage, et aggrave encore notre problème. Pour adresser ce scénario, nous proposons Lo-RISMA, qui découple l'optimisation des coefficients d'activation binaires et des déphasages quantifiés. Les premiers sont optimisés via SDR tandis que les seconds sont projetés sur l'espace quantifié. Contrairement à d'autres travaux antérieurs considérant les RISs à basse résolution, Lo-RISMA bénéficie des propriétés clés de la métrique choisie (c'est à dire, l'SMSE). Plus précisément, pour chaque itération de l'algorithme proposé pour une configuration de la RIS fixe, la stratégie de précodage est trouvée via une solution simple de forme fermée, et une fois la stratégie de précodage fixée, le problème de trouver les paramètres de la RIS est résolu efficacement via SDR. Les travaux susmentionnés ont abouti à la publication suivante.

[90] P. Mursia, V. Sciancalepore, A. Garcia-Saavedra, L. Cottatellucci, X. Costa-Perez, and D. Gesbert, "RISMA: Reconfigurable Intelligent Surfaces Enabling Beamforming for IoT Massive Access," *IEEE J. Sel. Areas Commun. (JSAC)*, vol. 8716, no. c, pp. 1–1, 2020

Part V: Concluding Remarks. Cette dernière partie conclut cette thèse en résumant les principales contributions et en tirant des remarques finales sur les parties précédemment décrites.

Enfin, nous donnons quelques aperçus sur d'éventuels futurs travaux et orientations de recherche. Le manuscrit se termine par les annexes, la liste des publications, le résumé de la thèse en français et la liste des références.

Bibliography

[1] F. Boccardi, R. Heath, A. Lozano, T. L. Marzetta, and P. Popovski, "Five Disruptive Technology Directions For 5G," *IEEE Commun. Mag.*, vol. 52, no. 2, pp. 74–80, 2014.

[2] A. Gupta and R. K. Jha, "A Survey of 5G Network: Architecture and Emerging Technologies," *IEEE Access*, vol. 3, pp. 1206–1232, 2015.

[3] M. Agiwal, A. Roy, and N. Saxena, "Next Generation 5G Wireless Networks: A Comprehensive Survey," *IEEE Commun. Surveys Tuts.*, vol. 18, no. 3, pp. 1617–1655, 2016.

[4] E. Larsson, O. Edfors, F. Tufvesson, and T. Marzetta, "Massive MIMO For Next Generation Wireless Systems," *IEEE Commun. Mag.*, vol. 52, no. 2, pp. 186–195, 2014.

[5] J. J. G. Andrews, S. Buzzi, W. Choi, S. V. S. Hanly, A. Lozano, A. A. C. K. Soong, and J. J. C. Zhang, "What Will 5G Be?" *IEEE J. Sel. Areas Commun. (JSAC)*, vol. 32, no. 6, pp. 1065–1082, 2014.

[6] J. Zhang, E. Björnson, M. Matthaiou, D. Wing, K. Ng, H. Yang, and D. J. Love, "Prospective Multiple Antenna Technologies for Beyond 5G," *IEEE J. Sel. Areas Commun. (JSAC)*, vol. 38, no. 8, pp. 1637–1660, 2020.

[7] X. Chen, D. W. K. Ng, W. Yu, E. G. Larsson, N. Al-Dhahir, and R. Schober, "Massive Access for 5G and Beyond," pp. 1–22, 2020, [Online]. Available: http://arxiv.org/abs/2002.03491.

[8] H. Q. Ngo, A. Ashikhmin, H. Yang, E. G. Larsson, and T. L. Marzetta, "Cell-Free Massive MIMO Versus Small Cells," *IEEE Trans. Wireless Commun.*, vol. 19, no. 5, pp. 3623–3624, 2020.

[9] N. Rajatheva, I. Atzeni, E. Björnson, A. Bourdoux, S. Buzzi, J. B. Doré, S. Erkucuk, M. Fuentes, K. Guan, Y. Hu, X. Huang, J. Hulkkonen, J. M. Jornet, M. Katz, R. Nilsson, E. Panayirci, K. Rabie, N. Rajapaksha, M. J. Salehi, H. Sarieddeen, T. Svensson, O. Tervo, A. Tölli, Q. Wu, and W. Xu, "White Paper On Broadband Connectivity In 6G," pp. 1–48, 2020, [Online]. Available: https://arxiv.org/abs/2004.14247.

[10] O. Elijah, C. Y. Leow, T. A. Rahman, S. Nunoo, and S. Z. Iliya, "A Comprehensive Survey of Pilot Contamination in Massive MIMO-5G System," *IEEE Trans. Control Syst. Technol.*, vol. 18, no. 2, pp. 905–923, 2016.

[11] J. Jose, A. Ashikhmin, T. L. Marzetta, and S. Vishwanath, "Pilot Contamination and Precoding in Multi-Cell TDD Systems," *IEEE Trans. Wireless Commun.*, vol. 10, no. 8, pp. 2640 – 2651, 2011.

[12] T. L. Marzetta, E. G. Larsson, and H. Yang, *Fundamentals of Massive MIMO.* Cambridge University Press, 2016.

[13] E. Bjornson, J. Hoydis, and L. Sanguinetti, "Massive MIMO Has Unlimited Capacity," *IEEE Trans. Wireless Commun.*, vol. 17, no. 1, pp. 574–590, 2018.

[14] L. You, X. Gao, X. Xia, N. Ma, and Y. Peng, "Pilot Reuse for Massive MIMO Transmission over Spatially Correlated Rayleigh Fading Channels," *IEEE Trans. Wireless Commun.*, vol. 14, no. 6, pp. 3352–3366, 2015.

[15] H. Yin, D. Gesbert, and L. Cottatellucci, "Dealing With Interference in Distributed Large-Scale MIMO Systems: A Statistical Approach," *IEEE J. Sel. Topics Signal Process.*, vol. 8, no. 5, pp. 942–953, 2014.

[16] J. Nam, J. Y. Ahn, A. Adhikary, and G. Caire, "Joint Spatial Division and Multiplexing: Realizing Massive MIMO Gains With Limited Channel State Information," in *Conf. on Inf. Sci. and Sys. (CISS)*, vol. 1, no. 1, 2012.

[17] J. Nam, A. Adhikary, J. Y. Ahn, and G. Caire, "Joint Spatial Division and Multiplexing: Opportunistic Beamforming, User Grouping and Simplified Downlink Scheduling," *IEEE J. Sel. Topics Signal Process.*, vol. 8, no. 5, pp. 876–890, 2014.

[18] A. Adhikary, J. Nam, J. Y. Ahn, and G. Caire, "Joint Spatial Division and Multiplexing-The Large-Scale Array Regime," *IEEE Trans. Inf. Theory*, vol. 59, no. 10, pp. 6441–6463, 2013.

[19] H. Yin, D. Gesbert, M. Filippou, and Y. Liu, "A Coordinated Approach to Channel Estimation in Large-Scale Multiple-Antenna Systems," *IEEE J. Sel. Areas Commun. (JSAC)*, vol. 31, no. 2, pp. 264–273, 2013.

[20] P. Mursia, I. Atzeni, D. Gesbert, and L. Cottatellucci, "Covariance Shaping for Massive MIMO Systems," in *Proc. IEEE Global Commun. Conf. (GLOBECOM)*, Abu Dhabi, UAE, 2018.

[21] P. Mursia, I. Atzeni, D. Gesbert, and L. Cottatellucci, "On the Performance of Covariance Shaping in Massive MIMO Systems," in *Proc. IEEE Int. Workshop Computer-Aided Modeling and Design of Commun. Links and Netw. (CAMAD)*, Barcelona, Spain, 2018.

[22] N. N. Moghadam, H. Shokri-Ghadikolaei, G. Fodor, M. Bengtsson, and C. Fischione, "Pilot Precoding and Combining in Multiuser MIMO Networks," *IEEE J. Sel. Areas Commun. (JSAC)*, vol. 35, no. 7, pp. 1632–1648, 2017.

[23] A. Liu and V. Lau, "Hierarchical Interference Mitigation for Large MIMO Cellular Networks," *IEEE Trans. Signal Process.*, vol. 62, no. 18, pp. 4786–4797, 2014.

[24] M. Dai and B. Clerckx, "Transmit Beamforming For MISO Broadcast Channels With Statistical and Delayed CSIT," *IEEE Trans. Commun.*, vol. 63, no. 4, pp. 1202–1215, 2015.

[25] X. Zhang, D. P. Palomar, and B. Ottersten, "Statistically Robust Design of Linear MIMO Transceivers," *IEEE Trans. Signal Process.*, vol. 56, no. 8 I, pp. 3678–3689, 2008.

[26] H. Tin, L. Cottatellucci, D. Gesbert, R. R. Müller, and G. He, "Robust Pilot Decontamination: A Joint Angle and Power Domain Approach," *IEEE Trans. Signal Process.*, vol. 64, no. 11, pp. 3371–3375, 2016.

[27] V. Raghavan, J. H. Kotecha, and A. M. Sayeed, "Why Does The Kronecker Model Result In Misleading Capacity Estimates?" *IEEE Trans. Inf. Theory*, vol. 56, no. 10, pp. 4843–4864, 2010.

[28] A. Asadi, Q. Wang, and V. Mancuso, "A Survey on Device-to-Device Communication in Cellular Networks," *IEEE Commun. Surveys Tutorials*, vol. 16, no. 4, pp. 1801–1819, 2014.

[29] M. N. Tehrani, M. Uysal, and H. Yanikomeroglu, "Device-to-Device Communication in 5G Cellular Networks: Challenges, Solutions, and Future Directions," *IEEE Commun. Mag.*, vol. 52, no. 5, pp. 86–92, 2014.

[30] E. Baştug, M. Bennis, and M. Debbah, "Living On The Edge: The Role of Proactive Caching In 5G Wireless Networks," *IEEE Commun. Mag.*, vol. 52, no. 8, pp. 82–89, 2014.

[31] N. Jindal and Z.-Q. Luo, "Capacity Limits of Multiple Antenna Multicast," in *Proc. IEEE Int. Symp. Inf. Theory. (ISIT)*, Barcelona, Spain, 2006.

[32] N. D. Sidiropoulos, T. N. Davidson, and Z.-Q. Luo, "Transmit Beamforming for Physical-Layer Multicasting," *IEEE Trans. Signal Process.*, vol. 54, no. 6, pp. 2239–2251, 2006.

[33] A. Khisti, U. Erez, and G. Wornell, "Fundamental Limits and Scaling Behavior of Cooperative Multicasting in Wireless Networks," *IEEE Trans. Inf. Theory*, vol. 52, no. 6, pp. 2762–2770, 2006.

[34] B. Sirkeci-Mergen and M. C. Gastpar, "On the Broadcast Capacity of Wireless Networks With Cooperative Relays," *IEEE Trans. Inf. Theory*, vol. 56, no. 8, pp. 3847–3861, 2010.

[35] F. Hou, S. Member, L. X. Cai, S. Member, and P.-h. Ho, "A Cooperative Multicast Scheduling Scheme for Multimedia Services in IEEE 802.16 Networks," *IEEE Trans. Wireless Commun.*, vol. 8, no. 3, pp. 1508–1519, 2009.

[36] Y. Zhou, H. Liu, Z. Pan, L. Tian, J. Shi, and G. Yang, "Two-Stage Cooperative Multicast Transmission With Optimized Power Consumption and Guaranteed Coverage," *IEEE J. Sel. Areas Commun. (JSAC)*, vol. 32, no. 2, pp. 274–284, 2014.

[37] M. A. Maddah-Ali and U. Niesen, "Fundamental Limits of Caching," *IEEE Trans. Inf. Theory*, vol. 60, no. 5, pp. 2856–2867, 2014.

[38] G. Paschos, E. Bastug, I. Land, G. Caire, and M. Debbah, "Wireless Caching: Technical Misconceptions and Business Barriers," *IEEE Commun. Mag.*, vol. 54, no. 8, pp. 16–22, 2016.

[39] G. Araniti, C. Campolo, M. Condoluci, A. Iera, and A. Molinaro, "LTE for Vehicular Networking: A Survey," *IEEE Commun. Mag.*, vol. 51, no. 5, pp. 148–157, 2013.

[40] V. Ntranos, N. D. Sidiropoulos, and L. Tassiulas, "On Multicast Beamforming for Minimum Outage," *IEEE Trans. Wireless Commun.*, vol. 8, no. 6, pp. 3172–3181, 2009.

[41] O. Mehanna, N. D. Sidiropoulos, and G. B. Giannakis, "Joint Multicast Beamforming and Antenna Selection," *IEEE Trans. Signal Process.*, vol. 61, no. 10, pp. 2660–2674, 2013.

[42] K.-H. Ngo, S. Yang, and M. Kobayashi, "Scalable Content Delivery With Coded Caching in Multi-Antenna Fading Channels," *IEEE Trans. Wireless Commun.*, vol. 17, no. 1, pp. 548–562, 2018.

[43] V. Exposito, S. Yang, and N. Gresset, "An Information-Theoretic Analysis of the Gaussian Multicast Channel With Interactive User Cooperation," *IEEE Trans. Wireless Commun.*, vol. 17, no. 2, pp. 899–913, 2018.

[44] L. Yang, Q. Ni, L. Lv, J. Chen, X. Xue, H. Zhang, and H. Jiang, "Cooperative Non-Orthogonal Layered Multicast Multiple Access for Heterogeneous Networks," *IEEE Trans. Commun.*, vol. 67, no. 2, pp. 1148–1165, 2019.

[45] C. Yin, Y. Wang, W. Lin, and J. Xu, "Device-to-Device Assisted Two-Stage Cooperative Multicast with Optimal Resource Utilization," in *Proc. IEEE Global Commun. Conf. (GLOBECOM)*, Austin, TX, USA, 2014.

[46] T. V. Santana, R. Combes, and M. Kobayashi, "Performance Analysis of Device-to-Device Aided Multicasting in General Network Topologies," *IEEE Trans. Commun.*, vol. 68, no. 1, pp. 137–149, 2020.

[47] Y. Mao, B. Clerckx, J. Zhang, V. O. Li, and M. Arafah, "Max-Min Fairness Of K-User Cooperative Rate-Splitting In MISO Broadcast Channel With User Relaying," *IEEE Trans. Wireless Commun.*, vol. 19, no. 10, pp. 6362–6376, 2020.

[48] W. Roh, J. Y. Seol, J. H. Park, B. Lee, J. Lee, Y. Kim, J. Cho, K. Cheun, and F. Aryanfar, "Millimeter-Wave Beamforming As An Enabling Technology For 5G Cellular Communications: Theoretical Feasibility and Prototype Results," *IEEE Commun. Mag.*, vol. 52, no. 2, pp. 106–113, 2014.

[49] B. P. S. Sahoo, C. Chou, C. Weng, and H. Wei, "Enabling Millimeter-Wave 5G Networks for Massive IoT Applications: A Closer Look at the Issues Impacting Millimeter-Waves in Consumer Devices Under the 5G Framework," *IEEE Consumer Electronics Magazine*, vol. 8, no. 1, pp. 49–54, 2019.

[50] O. Y. Kolawole, S. Biswas, K. Singh, and T. Ratnarajah, "Transceiver Design for Energy-Efficiency Maximization in mmWave MIMO IoT Networks," *IEEE Transactions on Green Communications and Networking*, vol. 4, no. 1, pp. 109–123, 2020.

[51] M. di Renzo et al., "Smart Radio Environments Empowered by Reconfigurable Intelligent Surfaces : How it Works, State of Research, and Road Ahead," 2020, [Online]. Available: https://arxiv.org/abs/2004.09352.

[52] E. Basar, M. Di Renzo, J. De Rosny, M. Debbah, M. Alouini, and R. Zhang, "Wireless Communications Through Reconfigurable Intelligent Surfaces," *IEEE Access*, vol. 7, pp. 116 753–116 773, 2019.

[53] M. di Renzo et al., "Smart Radio Environments Empowered by Reconfigurable AI meta-surfaces: An Idea Whose Time Has Come," *Eurasip Journal on Wireless Communications and Networking*, vol. 1, no. 1, 2019.

[54] K. Ntontin et al., "Reconfigurable Intelligent Surfaces vs. Relaying: Differences, Similarities, and Performance Comparison," 2019, [Online]. Available: http://arxiv.org/abs/1908.08747.

[55] E. Björnson and L. Sanguinetti, "Demystifying the Power Scaling Law of Intelligent Reflecting Surfaces and Metasurfaces," in *IEEE 8th International Workshop on Computational Advances in Multi-Sensor Adaptive Processing (CAMSAP)*, 2019.

[56] K. Ntontin, J. Song, M. D. Renzo, and S. Member, "Multi-Antenna Relaying and Reconfigurable Intelligent Surfaces : End-to-End SNR and Achievable Rate," 2019, [Online]. Available: http://arxiv.org/abs/1908.07967.

[57] E. Björnson, Ö. Özdogan, and E. G. Larsson, "Intelligent Reflecting Surface vs. Decode-and-Forward: How Large Surfaces Are Needed to Beat Relaying?" 2019, [Online]. Available: http://arxiv.org/abs/1906.03949.

[58] O. P. Falade et al., "Design and Characterisation of a Screen-Printed Millimetre-Wave Flexible Metasurface Using Copper Ink for Communication Applications," *Flexible and Printed Electronics*, vol. 3, no. 4, p. 045005, 2018.

[59] L. Subrt and P. Pechac, "Controlling Propagation Environments Using Intelligent Walls," in *Proceedings of IEEE European Conference on Antennas and Propagation, (EuCAP)*, Prague, Czech Republic, 2012.

[60] X. Tan, Z. Sun, J. M. Jornet, and D. Pados, "Increasing Indoor Spectrum Sharing Capacity Using Smart Reflect-Array," in *Proc. IEEE Int. Conf. Commun. (ICC)*, Kuala Lumpur, Malaysia, 2016.

[61] J. Zhang, E. Björnson, M. Matthaiou, D. W. K. Ng, H. Yang, and D. J. Love, "Multiple Antenna Technologies for Beyond 5G," 2019, [Online]. Available: http://arxiv.org/abs/1910.00092.

[62] E. Basar, "Transmission Through Large Intelligent Surfaces: A New Frontier in Wireless Communications," in *"Proc. IEEE European Conference on Networks and Communications (EuCNC)"*, Valencia, Spain, 2019.

[63] Ö. Özdogan, E. Björnson, and E. G. Larsson, "Intelligent Reflecting Surfaces: Physics, Propagation, and Pathloss Modeling," *IEEE Wireless Communications Letters*, vol. 9, no. 5, pp. 581–585, 2020.

[64] W. Tang, M. Z. Chen, X. Chen, J. Y. Dai, Y. Han, M. Di Renzo, Y. Zeng, S. Jin, Q. Cheng, and T. J. Cui, "Wireless Communications with Reconfigurable Intelligent Surface: Path Loss Modeling and Experimental Measurement," 2019, [Online]. Available: http://arxiv.org/abs/1911.05326.

[65] S. Hu, F. Rusek, and O. Edfors, "Beyond Massive MIMO: The Potential of Positioning with Large Intelligent Surfaces," *IEEE Trans. Signal Process.*, vol. 66, no. 7, pp. 1761–1774, 2018.

[66] S. Zhang and R. Zhang, "Capacity Characterization for Intelligent Reflecting Surface Aided MIMO Communication," 2019, [Online]. Available: http://arxiv.org/abs/1910.01573.

[67] M. Cui, G. Zhang, and R. Zhang, "Secure Wireless Communication Via Intelligent Reflecting Surface," in *Proc. IEEE Global Commun. Conf. (GLOBECOM)*, Waikoloa, HI, USA, 2019.

[68] X. Yu, D. Xu, Y. Sun, D. W. K. Ng, and R. Schober, "Robust and Secure Wireless Communications via Intelligent Reflecting Surfaces," 2019, [Online]. Available: http://arxiv.org/abs/1912.01497.

[69] M. Fu, Y. Zhou, and Y. Shi, "Intelligent Reflecting Surface for Downlink Non-Orthogonal Multiple Access Networks," in *IEEE Globecom Workshops (GC Wkshps)*, 2019, pp. 1–6.

[70] T. Jiang and Y. Shi, "Over-the-Air Computation via Intelligent Reflecting Surfaces," in *IEEE Global Communications Conference (GLOBECOM)*, 2019, pp. 1–6.

[71] C. Huang et al., "Energy Efficient Multi-User MISO Communication Using Low Resolution Large Intelligent Surfaces," in *Proc. IEEE Globecom Workshops, (GC WKSHPS)*, Abu Dhabi, United Arab Emirates, 2018.

[72] C. Huang, A. Zappone, G. C. Alexandropoulos, M. Debbah, and C. Yuen, "Reconfigurable Intelligent Surfaces for Energy Efficiency in Wireless Communication," *IEEE Transactions on Wireless Communications*, vol. 18, pp. 4157–4170, 2019.

[73] C. Huang et al., "Holographic MIMO Surfaces for 6G Wireless Networks: Opportunities, Challenges, and Trends," 2019, [Online]. Available: http://arxiv.org/abs/1911.12296.

[74] W. Tang, J. Y. Dai, M. Chen, X. Li, Q. Cheng, S. Jin, K. K. Wong, and T. J. Cui, "Programmable Metasurface-Based RF Chain-Free 8PSK Wireless Transmitter," *Electronics Letters*, vol. 55, no. 7, pp. 417–420, 2019.

[75] V. Arun and H. Balakrishnan, "RFocus: Practical Beamforming for Small Devices," in *17th USENIX Symposium on Networked Systems Design and Implementation (NSDI 20)*, 2020.

[76] F. Liu et al., "Intelligent Metasurfaces with Continuously Tunable Local Surface Impedance for Multiple Reconfigurable Functions," *Physical Review Applied*, vol. 11, no. 4, pp. 1–10, 2019.

[77] L. Dai et al., "Reconfigurable Intelligent Surface-Based Wireless Communications: Antenna Design, Prototyping, and Experimental Results," *IEEE Access*, vol. 8, pp. 45 913–45 923, 2020.

[78] Z.-Q. He and X. Yuan, "Cascaded Channel Estimation for Large Intelligent Metasurface Assisted Massive MIMO," *IEEE Wireless Commun. Lett.*, 2019.

[79] D. Mishra and H. Johansson, "Channel Estimation and Low-complexity Beamforming Design for Passive Intelligent Surface Assisted MISO Wireless Energy Transfer," in *Proc. IEEE Int. Conf. Acoust., Speech, and Signal Process. (ICASSP)*, Brighton, UK, 2019.

[80] X. Yu, D. Xu, and R. Schober, "MISO Wireless Communication Systems Via Intelligent Reflecting Surfaces: (Invited Paper)," in *Proc. IEEE Int. Conf. Commun. (ICC)*, Shanghai, China, 2019.

[81] Q.-U.-A. Nadeem, A. Kammoun, A. Chaaban, M. Debbah, and M.-S. Alouini, "Asymptotic Max-Min SINR Analysis of Reconfigurable Intelligent Surface Assisted MISO Systems," 2019, [Online]. Available: http://arxiv.org/abs/1903.08127.

[82] Q. Wu and R. Zhang, "Intelligent Reflecting Surface Enhanced Wireless Network: Joint Active and Passive Beamforming Design," *IEEE Transactions on Wireless Communications*, vol. 18, no. 11, pp. 5394–5409, 2019.

[83] Q. Wu and R. Zhang, "Beamforming Optimization for Intelligent Reflecting Surface with Discrete Phase Shifts," in *Proc. IEEE Int. Conf. Acoust., Speech, and Signal Process. (ICASSP)*, Brighton, UK, 2019.

[84] R. Karasik, O. Simeone, M. Di Renzo, and S. Shamai, "Beyond Max-SNR: Joint Encoding for Reconfigurable Intelligent Surfaces," 2019, [Online]. Available: http://arxiv.org/abs/1911.09443.

[85] C. Huang, R. Mo, and C. Yuen, "Reconfigurable Intelligent Surface Assisted Multiuser MISO Systems Exploiting Deep Reinforcement Learning," 2020, [Online]. Available: http://arxiv.org/abs/2002.10072.

[86] P. Mursia, I. Atzeni, D. Gesbert, and L. Cottatellucci, "Enforcing Statistical Orthogonality in Massive MIMO Systems via Covariance Shaping," 2021, submitted to *IEEE Trans. Wireless Commun. (TWC)* [Online]. Available: https://arxiv.org/abs/2106.07952.

[87] P. Mursia, I. Atzeni, D. Gesbert, and M. Kobayashi, "D2D-Aided Multi-Antenna Multicasting," in *Proc. IEEE Int. Conf. Commun. (ICC)*, Shanghai, China, 2019, **best paper award.**

[88] P. Mursia, I. Atzeni, M. Kobayashi, and D. Gesbert, "D2D-Aided Multi-Antenna Multicasting in a Dense Network," in *Proc. Asilomar Conf. Signals, Syst., and Comput. (ASILOMAR)*, Pacific Grove, USA, 2019.

[89] P. Mursia, I. Atzeni, M. Kobayashi, and D. Gesbert, "D2D-Aided Multi-Antenna Multicasting under Generalized CSIT," 2021, submitted to *IEEE Trans. Wireless Commun. (TWC)* [Online]. Available: https://arxiv.org/abs/2102.01624.

[90] P. Mursia, V. Sciancalepore, A. Garcia-Saavedra, L. Cottatellucci, X. Costa-Perez, and D. Gesbert, "RISMA: Reconfigurable Intelligent Surfaces Enabling Beamforming for IoT Massive Access," *IEEE J. Sel. Areas Commun. (JSAC)*, vol. 8716, no. c, pp. 1–1, 2020.

[91] C. Huang, A. Zappone, M. Debbah, and C. Yuen, "Achievable Rate Maximization by Passive Intelligent Mirrors," in *Proc. IEEE Int. Conf. Acoust., Speech, and Signal Process. (ICASSP)*, Calgary, Canada, 2018.

[92] A. M. Sayeed, "Deconstructing Multiantenna Fading Channels," *IEEE Trans. Signal Process.*, vol. 50, no. 10, pp. 2563–2579, 2002.

[93] A. Paulraj, R. Nabar, and D. Gore, *Introduction to Space-Time Wireless Communications*. Cambridge University Press, 2006.

[94] A. K. Hassan, M. Moinuddin, U. M. Al-Saggaf, O. Aldayel, T. N. Davidson, and T. Y. Al-Naffouri, "Performance Analysis and Joint Statistical Beamformer Design for Multi-User MIMO Systems," *IEEE Commun. Lett.*, vol. 7798, no. c, pp. 1–1, 2020.

[95] J. Hoydis, S. Ten Brink, and M. Debbah, "Massive MIMO In The UL/DL of Cellular Networks: How Many Antennas Do We Need?" *IEEE J. Sel. Areas Commun. (JSAC)*, vol. 31, no. 2, pp. 160–171, 2013.

[96] E. Björnson, J. Hoydis, and L. Sanguinetti, "Massive MIMO Networks: Spectral, Energy, and Hardware Efficiency," *Found. Trends Signal Process.*, vol. 11, no. 3–4, pp. 154–655, 2017.

[97] L. Grippo and M. Sciandrone, "On The Convergence of The Block Nonlinear Gauss-Seidel Method Under Convex Constraints," *Operations Research Letters*, vol. 26, no. 3, pp. 127–136, 2000.

[98] W. Weichselberger, M. Herdin, H. Özcelik, and E. Bonek, "A Stochastic MIMO Channel Model With Joint Correlation of Both Link Ends," *IEEE Trans. Wireless Commun.*, vol. 5, no. 1, pp. 90–99, 2006.

[99] I. Atzeni, B. Gouda, and A. Tolli, "Distributed Precoding Design via Over-the-Air Signaling for Cell-Free Massive MIMO," *IEEE Trans. Wireless Commun.*, vol. 20, no. 2, pp. 1201–1216, Feb. 2021.

[100] G. Scutari, F. Facchinei, P. Song, D. P. Palomar, and J. S. Pang, "Decomposition by partial linearization: Parallel optimization of multi-agent systems," *IEEE Trans. Signal Process.*, vol. 62, no. 3, pp. 641–655, Feb. 2014.

[101] C. B. Peel, B. M. Hochwald, and A. L. Swindelhurst, "A Vector-Perturbation Technique for Near-Capacity Multiantenna Multiuser Communication - Part I: Channel Inversion and Regularization," *IEEE Trans. Commun.*, vol. 53, no.1, no. 1, pp. 195–202, 2005.

[102] S. Christensen, R. Agarwal, E. Carvalho, and J. Cioffi, "Weighted Sum-Rate Maximization Using Weighted MMSE for MIMO-BC Beamforming Design," *IEEE Trans. Wireless Commun.*, vol. 7, no. 12, pp. 4792–4799, 2008.

[103] Q. H. Spencer, A. L. Swindlehurst, and M. Haardt, "Zero-Forcing Methods For Downlink Spatial Multiplexing In Multiuser MIMO Channels," *IEEE Trans. Signal Process.*, vol. 52, no. 2, pp. 461–471, 2004.

[104] J. Harri, F. Filali, and C. Bonnet, "Mobility Models for Vehicular Ad Hoc Networks: A Survey and Taxonomy," *IEEE Trans. Control Syst. Technol.*, vol. 11, no. 4, pp. 19–41, 2009.

[105] A. Destounis, G. S. Paschos, and D. Gesbert, "Selective Fair Scheduling over Fading Channels," in *Proc. Int. Symp. Model. and Optim. in Mobile, Ad Hoc and Wireless Netw. (WiOpt)*, 2018.

[106] A. N. Uwaechia and N. M. Mahyuddin, "A Comprehensive Survey on Millimeter Wave Communications for Fifth-Generation Wireless Networks: Feasibility and Challenges," *IEEE Access*, vol. 8, pp. 62 367–62 414, 2020.

[107] S. V. Hum and J. Perruisseau-Carrier, "Reconfigurable Reflectarrays And Array Lenses For Dynamic Antenna Beam Control: A Review," *IEEE Trans. Antennas Propag.*, vol. 62, no. 1, pp. 183–198, 2014.

[108] R. Mendez-Rial, C. Rusu, N. Gonzalez-Prelcic, A. Alkhateeb, and R. W. Heath, "Hybrid MIMO Architectures for Millimeter Wave Communications: Phase Shifters or Switches?" *IEEE Access*, vol. 4, pp. 247–267, 2016.

[109] B. Di, H. Zhang, L. Li, L. Song, Y. Li, and Z. Han, "Practical Hybrid Beamforming With Finite-Resolution Phase Shifters for Reconfigurable Intelligent Surface Based Multi-User Communications," *IEEE Trans. Veh. Technol.*, vol. 69, no. 4, pp. 4565–4570, 2020.

[110] R. Hunger, M. Joham, and W. Utschick, "On The MSE-Duality of The Broadcast Channel And The Multiple Access Channel," *IEEE Trans. Signal Process.*, vol. 57, no. 2, pp. 698–713, 2009.

[111] D. Xu, X. Yu, and R. Schober, "Resource Allocation for Intelligent Reflecting Surface-Assisted Cognitive Radio Networks," 2020, [Online]. Available: http://arxiv.org/abs/2001.11729.

[112] X. Shen, S. Diamond, Y. Gu, and S. Boyd, "Disciplined Convex-Concave Programming," in *IEEE 55th Conference on Decision and Control, (CDC)*, Las Vegas, NV, USA, 2016.

[113] Z. Luo, W. Ma, A. M. So, Y. Ye, and S. Zhang, "Semidefinite Relaxation of Quadratic Optimization Problems," *IEEE Signal Processing Magazine*, vol. 27, no. 3, pp. 20–34, 2010.

[114] A. M. C. So, J. Zhang, and Y. Ye, "On Approximating Complex Quadratic Optimization Problems via Semidefinite Programming Relaxations," *Math. Program.*, vol. 110, pp. 93–110, 2007.

[115] Y. Han, W. Tang, S. Jin, C.-K. Wen, and X. Ma, "Large Intelligent Surface-Assisted Wireless Communication Exploiting Statistical CSI," *IEEE Trans. Veh. Technol.*, vol. 68, no. 8, pp. 8238–8242, 2019.

[116] W. K. Ma, P. C. Ching, and Z. Ding, "Semidefinite Relaxation Based Multiuser Detection for M-Ary PSK Multiuser Systems," *IEEE Trans. Signal Process.*, vol. 52, no. 10, pp. 2862–2872, 2004.

[117] N. D. Sidiropoulos and Z. Q. Luo, "A Semidefinite Relaxation Approach To MIMO Detection For High-Order QAM Constellations," *IEEE Signal Process. Lett.*, vol. 13, no. 9, pp. 525–528, 2006.

[118] A. Abrardo, D. Dardari, and M. Di Renzo, "Intelligent Reflecting Surfaces: Sum-Rate Optimization Based on Statistical CSI," 2020, [Online]. Available: http://arxiv.org/abs/2012.10679.